STRESS RELAXATION OF AZ31 ALLOY USING HIGH ENERGY DIFFRACTION MICROSCOPY

BY

WENLI TANG

THESIS

Submitted in partial fulfillment of the requirements
for the degree of Master of Science in Mechanical Engineering
in the Graduate College of the
University of Illinois at Urbana-Champaign, 2014

Urbana, Illinois

Adviser:

Professor Armand Beaudoin

ABSTRACT

AZ31 is a commercial Mg-3wt.%Al-1wt.%Zn ternary alloy with good specific strength, but relatively limited room temperature formability – a consequence of marked difference in strength of slip systems in this hcp alloy. Tensile test is the traditional method to study the kinetics of individual slip/twin events and, in the present work, High Energy Diffraction Microscopy (HEDM) is used to explore the kinetics at the scale of individual grains by following diffraction spots during a loading increment and subsequent relaxation. The study was conducted at the Advanced Photon Source (APS) sector 1-ID-C at Argonne National Laboratory and loading steps and relaxation were set at different points within elasto-plastic transitions (118MPa, 135MPa, 153MPa and 168MPa).

Two different aspects of diffraction pattern were studied in the thesis: individual peak dynamics and reflection-wise ellipse-fitting strain time series. Peaks of crystallographic planes having a normal roughly parallel to the tensile axis are tracked and the relative plane distances calculated from radial displacements. Generally speaking, grains not favorably oriented for basal slip showed a loading response followed by small (or no) relaxation. In contrast, grains with a pyramidal plane sharing a normal with the tensile axis demonstrate quite diverse response. As for ellipse fitting result, net peak strains relating to loading step for distinct plane families decreased linearly with dot product of loading-direction vector and corresponding basal plane normal vector.

The thesis concludes the algorithm for analysis: image rotation, image combination, Gaussian filtering, peak isolation, trajectory generation, reciprocal space–detector space transformation, ellipse fitting and peak strain–orientation correlation.

To my parents, for their love and support.

ACKNOWLEDGMENTS

It is my great honor to thank all the people who helped, encouraged, taught and assisted me throughout my two-year master education. This thesis could not be accomplished without the help of those nice and helpful individuals.

First, I sincerely thank my academic adviser, Professor Armand Beaudoin, for his patient instruction and spirit of cooperation. Treating me as peer rather than junior, he thought about my idea carefully, exchanged viewpoints with me and gave me freedom and encouragement to handle my own project. I am very grateful to him for inviting me to assist experiment at Argonne National Laboratory, which offered me opportunity to touch the academic frontier of material science. But mostly, Professor Beaudoin always respected my own life choice and gave me time to think things through.

I am very appreciative to Kamalika Chattergee, my best lab partner. She always spent her own time assisting me with time-consuming tensile test. Happy and energetic all the time, she was the one who sent me the right paper when I was stuck in some difficulty. Also, I am indebted to Timothy Garbaciak for conducting DIC experiment in my busiest period.

I am grateful to thank Dr. Peter Kenesei, beam scientist of Argonne National Laboratory, for his help in HEDM experiment setup and constructive interpretation of data trend. He patiently introduced me details of instrument setup, usage of Fit2D, HEXRD and basic of X-ray diffraction when I was a green hand. Cautious of data trend, he raised the baseline comparison to state the beam stability. I learned rigorousness and preciseness of researcher from Dr. Kenesei and I believe it will be my lifelong gift.

I am very obligated to Professor Dallas Trinkle, professor of department of material science of University of Illinois at Urbana and Champaign. He contributed his amazing memory to my literature review and introduced me the work of Caillard about 'prismatic glide in divalent h.c.p metals', the work of Corby and Caceres about 'serrated flow in magnesium alloy AZ91' and so on. It is his discussion about deformation mechanism of magnesium that broaden my academic scope of peer works all over the world.

I would like to acknowledge Greg Milner, the research laboratory machine shop supervisor of aerospace engineering, for manufacturing magnesium alloy for my research. Since Mg is flammable, it is challenging to electrical discharge machine the cold-rolled AZ31 plate; however, Greg solved all the manufacturability problem and gave me qualified strip and dog bone specimens.

I also want to express my deepest appreciation for Caterpillar Inc.'s generous gift for my research. In terms of research, the grant allowed the purchase of necessary lab equipments and the manufacture of material. As for my personal interest, the grant waived my two-year graduate school tuition. The help from Caterpillar really boosted my research career.

Finally, I would like to give my sincere gratitude towards my family for their eternal support and selfless love. From a young age, my father opened the door of the world of engineering for me by teaching me how to solve the problem, from fixing the washing machine to replacing the part of bicycle, by hands. Throughout my eighteen-year campus life, my mother always shared her life experience with me every time I made stupid mistake or lost myself in different dilemmas. I also thank my grandparents for what they taught me–spirit of chasing freedom and bravery of saying 'no' to what I dislike.

TABLE OF CONTENTS

LIST OF TABLES

LIST OF FIGURES

LIST OF ABBREVIATIONS

HEDM	High Energy Diffraction Microscopy
HCP	Hexagonal Close Packed
TEM	Transmission Electron Microscopy
APS	Advanced Photon Source
XRD	X-Ray Diffraction
DIC	Digital Image Correlation
WAXS	Wide Angle Scattering
SAXS	Small Angle Scattering
ND	Normal Direction
TD	Transverse Direction
RD	Rolling Direction
EDM	Electrical Discharge Machining

CHAPTER 1

INTRODUCTION

1.1 Magnesium Alloys

In the last few decades, energy efficiency has become an very important engineering issue and much research on energy-saving has been proposed and funded. In material aspects, lighter and more durable substitutes for traditional materials are highlighted.

Magnesium alloys are promising structural light materials with high specific strength and specific stiffness and are widely applied for different engineering purposes. It is the best substitute for aluminum and steel. However, the limited room-temperature formability restricts its wider application. Mg-3AL-1Zn (AZ31) is the most popular magnesium alloy for sheet application [1]. AZ31 is an alloy with not only good strength-ductility combination, but also corrosion and weldability. Nowadays, AZ31B is applied as biodegradable metallic implant [2]. In the aerospace industry, Aircraft fuselage lap joints are made using AZ31 alloy. At elevated temperature, AZ31B's super formability could be used to manufacture intricate components for automobiles [3]. Moreover, the AZ31B could also be used in cell phone and laptop cases [4], speaker cones and concrete tools [5].

1.2 Deformation Mechanism

The crystalline structure of Magnesium is hexagonal close packed (HCP).As shown in Figure 1.1, the lattice parameters **a** and **c** are 0.32nm and 0.52nm separately. The atomic number of Mg is 12, which makes Mg the lightest metal in the periodic table. In contrast to face-centered cubic crystal (FCC) structure and body-centered cubic (BCC) structure,

the HCP crystal structure has a reduced number of active slip systems because they are not energy-favorable. If the number of slip modes does not satisfy the compatibility condition in metallic materials, then mechanical twinning becomes important complementary deformation mechanism. Generally speaking, the HCP metals usually show strong temperature-dependent behaviors and different deformation modes are triggered with temperature elevation. As a result, the ductility of the metal is improved and recrystallization may occur [6, 7].

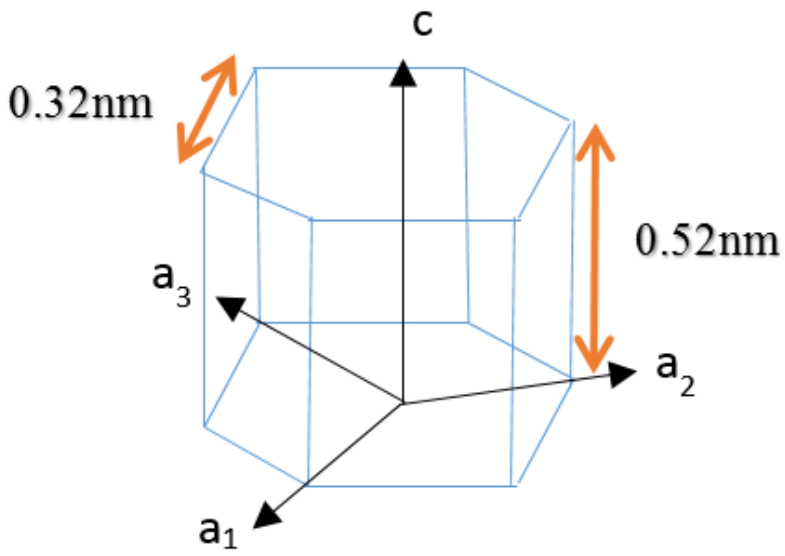

Figure 1.1: Magnesium Crystal Structure and Lattice Parameters

1.2.1 Glide Mechanisms in HCP

Figure 1.2 shows common glide planes and Yoo [8] listed the possible slip systems in Table 1.1. The number of potential deformation systems in HCP are large and the most energy-favorable slip systems in HCP metals are prismatic and basal glide on $\langle \mathbf{a} \rangle$ direction. Two families provide four independent slip systems but all resultant strain is $\langle \mathbf{a} \rangle$ direction. Therefore, the activation of slip on pyramidal planes with Burger vector of $\langle \mathbf{a+c} \rangle$ satisfies the Taylor criterion for homogeneous plastic deformation [9]. Generally speaking, the relative ease of slip on $\langle \mathbf{a} \rangle$ compared with that on $\langle \mathbf{a+c} \rangle$ is controlled by the crystal axial ratio

Table 1.1: Reported Independent Dislocation Systems in HCP [8]

Slip Direction	Glide Plane	Notation	Number of Independent Modes
$\langle a \rangle$	Basal	$\{0002\}\ \langle 11\bar{2}0 \rangle$	2
$\langle a \rangle$	Prismatic	$\{1\bar{1}00\}\ \langle 11\bar{2}0 \rangle$	2
$\langle a \rangle$	Pyramidal	$\{1\bar{1}01\}\ \langle 1120 \rangle$	4
$\langle a+c \rangle$	Pyramidal	$\{10\bar{1}1\}\ \langle 11\bar{2}\bar{3} \rangle$	4
$\langle a+c \rangle$	Pyramidal	$\{2\bar{1}\bar{1}1\}\ \langle 11\bar{2}\bar{3} \rangle$	4
$\langle a+c \rangle$	Pyramidal	$\{11\bar{2}2\}\ \langle 11\bar{2}\bar{3} \rangle$	4

c/a.

The primary slip systems in HCP metals are determined by the shortest Burger vectors and they may either located in basal plane, such as Mg and Cd, or in prism plane, such as Ti and Zr [10]. A. Couret and D. Caillard [11] employed TEM to observe the prismatic glide in divalent HCP metals and proposed an anchoring-unlocking cross-slip mechanism at low temperatures and a jog-pair mechanism at high temperature. Polycrystalline Mg and its alloy was studied and texture simulation analyses of texture evolution showed that $\langle \mathbf{c}+\mathbf{a} \rangle$ dislocations plays a critical rule in deformation [12] and the enhanced secondary slip was complemented by the source and mobility [13] of $\langle \mathbf{c}+\mathbf{a} \rangle$ dislocations for the pyramidal slip [14]. Koike [15] applied TEM to study the room temperature polycrystalline AZ31 deformation mechanism and found in some grains non-basal slip of $\langle \mathbf{c}+\mathbf{a} \rangle$ is dominant and when the yield anisotropy factor is increased over 1.1, 40 percent of the $\mathbf{a}$ dislocation segments show cross-slip from basal to non-basal planes.

1.2.2 Mechanical Twinning in HCP

There are two different kinds of mechanical twinning identified in HCP structure– tensile twinning and compression (contraction) twinning.

Tensile Twinning is activated on the plane $\{10\bar{1}2\}$ when its activation energy is less than that of pyramidal slip $\langle \mathbf{c}+\mathbf{a} \rangle$. As shown in Figure 1.3, the Schmid factor changes after the lattice rotates 86 degrees. Therefore, a reset of deformation systems follows tensile twinning

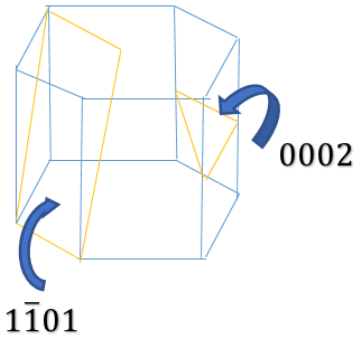

(a) Illustration of Basal and Pyramidal Planes

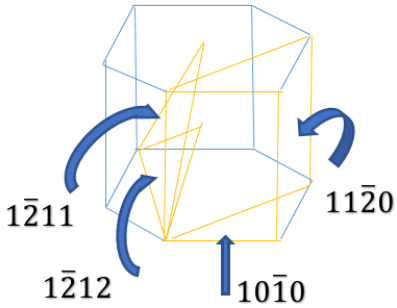

(b) Illustration of Prismatic and Pyramidal Planes

Figure 1.2: Geometrical Illustration of Crystallographic Slip Planes in a Single Mg

[16].

Compression Twinning occurs on the plane $\{10\bar{1}1\}$ at room temperature. As shown in Figure 1.4, the atomic layers tilt 56 degrees from the basal planes of initial crystal and the resolved shear stress on the tensile twinning system within the lenticular twin increases. Afterwards, tensile twinning is triggered inside the initial twin. Finally, the net rotation is 37 degrees with respect to the matrix basal plane. This mechanism is called double twinning [16].

Many theoretical calculations results of stacking faults and twin boundaies have been done. According to ab initio calculations, tension twins $\{10\bar{1}2\}$ in Zr and Mg are energy preferred [10]. For all HCP materials studied, the stacking fault is stable and has an energy comparable with twin boundaries, which is due to a local reconstruction of basal planes passing through the fault [17, 14].

1.2.3 Deformation Systems of Mg

The activity of deformation mechanism of AZ31B has been studied in the recent years. Yasumasa Chino [18] showed that in a coarse grain polycrystalline Mg, non-basal slip plays important role in satisfying five independent slip condition and twinning serves as relax-

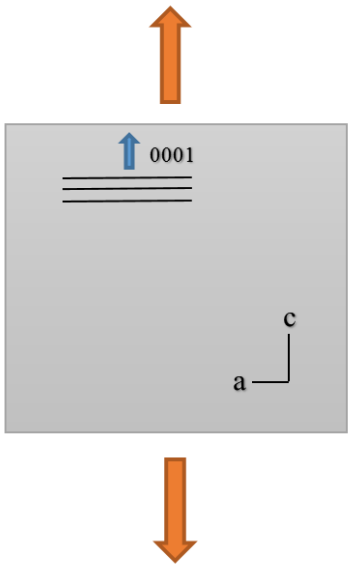

(a) Original Crystal Lattice and Orientation

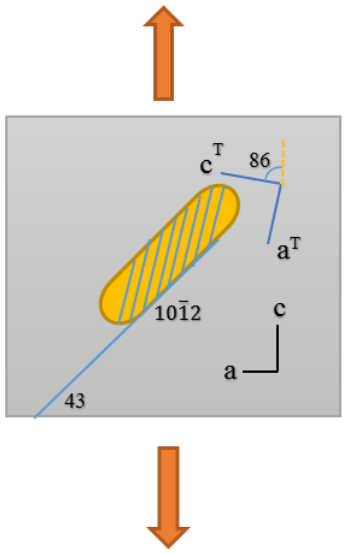

(b) Twinned Lenticular and Rotation Direction

Figure 1.3: Illustration of Basal Plane Rotation of Tensile Twinning

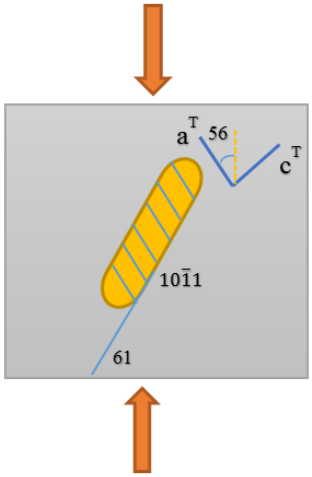

(a) Twinned Lenticular and Rotation Direction of Compressive Twinning

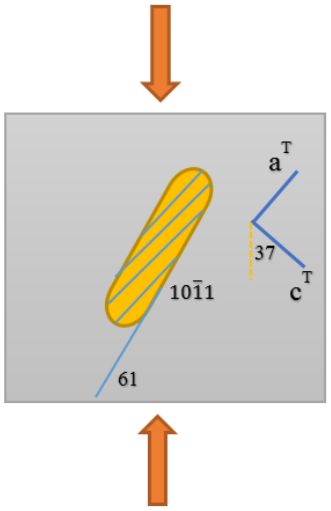

(b) Twinned Lenticular and Rotation Direction of Subsequent Twinning

Figure 1.4: Illustration of Basal Plane Rotation of Double Twinning

ation mechanism to release the stress concentration developed during the tensile test. In compression test, twinning serves as not only relaxation mechanism but also complementary deformation mode. In fine grain polycrystalline Mg, grain boundary sliding, instead of compression twinning, is the critical relaxation mechanism even in room temperature, which rationalizes the better ductility of fine grain Mg than that of coarse grain Mg. Yi [19] showed that the activity of the basal $\langle \mathbf{a} \rangle$ slip and the tensile twinning contribute to the mechanical anisotropy during tension, but $\langle \mathbf{a+c} \rangle$ becomes more important in compression, while the conclusion depends on texture of specimen–as specimen discussed in this thesis, $\langle \mathbf{a+c} \rangle$ becomes more important in tension because most basal poles are perpendicular to the tensile axis.

The easiest deformation mechanisms are basal $\{0001\}\ \langle 11\bar{2}0 \rangle$ slip and $\{10\bar{1}2\}\ \langle 10\bar{1}1 \rangle$ twinning [20]. Compared with aluminum having 12 $\{111\}\ \langle 1\bar{1}0 \rangle$ geometrical and 5 independent slip systems, two independent slip systems prevent the arbitrary deformation of magnesium [21]. Some analyses on slip systems are based on Schmid-Factor considerations [22] There are three different possible slip systems, which include (1) the basal slip $\{0001\}\ \langle 11\bar{2}0 \rangle$, (2) the prism slip $\{10\bar{1}0\}\ \langle 11\bar{2}0 \rangle$, $\{10\bar{1}0\}\ \langle 0001 \rangle$ and $\{11\bar{2}0\}\ \langle 0001 \rangle$, (3) the first pyramidal slip $\{10\bar{1}1\}\ \langle 11\bar{2}0 \rangle$, (4) the second pyramidal slip $\{11\bar{2}2\}\ \langle 11\bar{2}\bar{3} \rangle$. In consideration of Schmid factors, critical resolved shear stress (CRSS) and CRSS temperature dependence, the basal slip is always dominant and the slips in the same direction on the prism $\{1\bar{1}00\}$ and pyramidal $\{10\bar{1}1\}$ plane only occur under high stress concentration. When the temperature increases over 600K, the CRSS of prismatic and pyramidal slips decreases to the same order of basal slip [22].

1.3 Fundamentals of High Energy Diffraction Microscopy

X-ray Diffraction (XRD) provides one of the fundamental methods of experimental stress analysis. XRD measures the average spacing between layers of atoms, which offers insight into the grain and subgrain length-scale information of the micro-structure of materials.

1.3.1 Basics of Diffraction Physics

X-ray diffraction is a tool of analyzing the atomic and molecular structure of materials. The principle of the XRD is based on one basic phenomenon, i.e. when x-rays are projected upon layers of atoms, the x-rays would be diffracted by the lattice when the constructive interference condition was met. This diffraction could be formulated by the famous Bragg's Law:

$$n\lambda = 2d\sin(\theta) \tag{1.1}$$

n: Order of Diffraction

λ: Wavelength of Xrays

d: Spacing between Different Atomic Layers

θ: Diffraction Angle

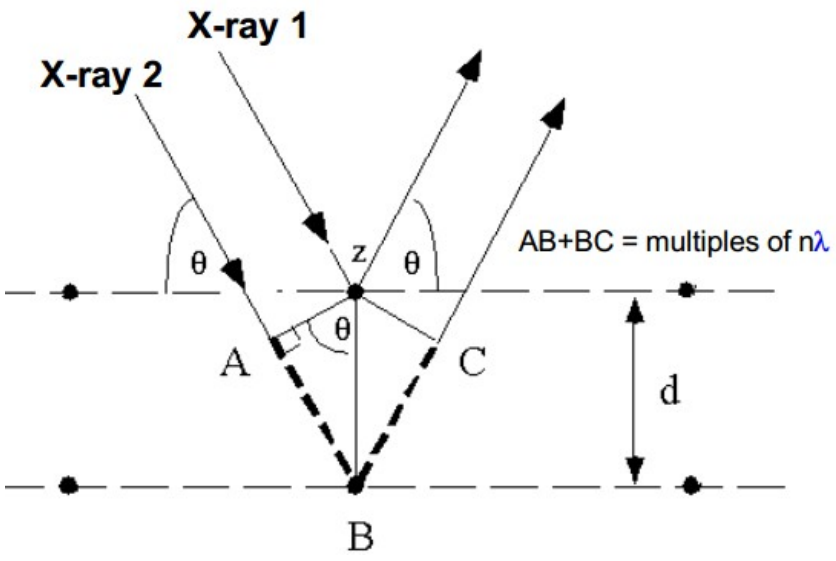

Figure 1.5: Geometry of Bragg's Law

Bragg's Law could also be applied to any other beam source with wavelength close to scale of atomic lattice, such as ions, neutrons and electrons.

1.3.2 Reciprocal Lattice and Xray Diffraction Geometry

The lattice is the basic unit of crystal and it is distinct property for specific material. Crystalline structure is composed of ordered and periodic lattices. Therefore, X-Ray diffraction could map intrinsic lattice geometry into a diffraction pattern.

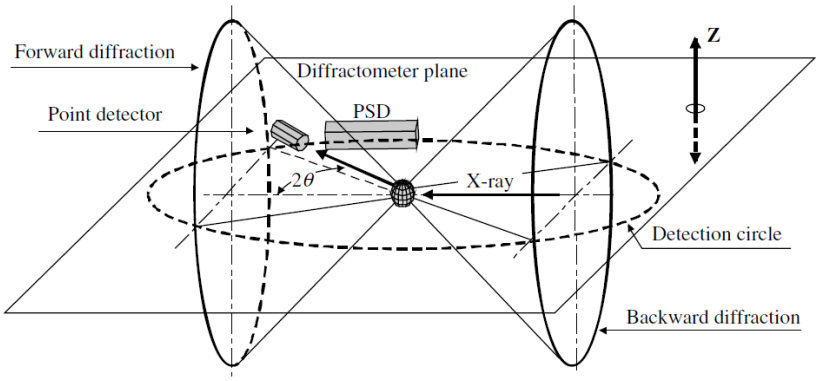

Figure 1.6: Diffraction Patterns in 3D Space from a Powder Sample and the Diffractometer [23].

The reciprocal lattice is a transformation of the crystal lattice in real space to reciprocal space. The shape and size in a unit cell in real space is symbolized by three vectors **a**,**b** and **c**. The unit cell of the corresponding reciprocal lattice is given by three vectors $\mathbf{a}^*$, $\mathbf{b}^*$ and $\mathbf{c}^*$. V is the triple product of **a**,**b** and **c**. The relationship of vectors in two different spaces is shown as follows:

$$\begin{aligned} \mathbf{a}^* &= \frac{1}{V}(\mathbf{b} \times \mathbf{c}) \\ \mathbf{b}^* &= \frac{1}{V}(\mathbf{c} \times \mathbf{a}) \\ \mathbf{c}^* &= \frac{1}{V}(\mathbf{a} \times \mathbf{b}) \end{aligned} \tag{1.2}$$

The volume of the crystal unit cell in real space is

$$V = \mathbf{a} \cdot \mathbf{b} \times \mathbf{c} \tag{1.3}$$

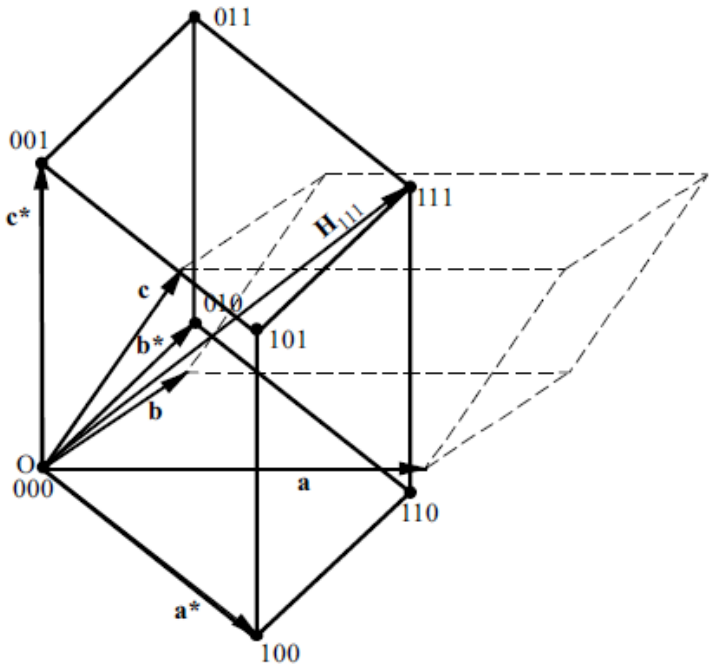

Figure 1.7: The relationship between the original lattice in real space and the reciprocal lattice [24]

Since the reciprocal lattice axis is the cross product of two real space lattice axes, it is perpendicular to the planes defined by the two axes vectors. Figure 1.7 shows the relationship between the reciprocal space and the real lattice space. Every vector in the reciprocal space represents the normal vector of plane of lattice and the norm of the vector indicates the distance between two sequential parallel planes. Except for the origin, each lattice point is denoted by a set of tuple (hkl). The relationship is as follows:

$$\mathbf{H}_{hkl} = h\mathbf{a}^* + k\mathbf{b}^* + l\mathbf{c}^* \tag{1.4}$$

$$|\mathbf{H}_{hkl}| = \frac{1}{d_{hkl}} \tag{1.5}$$

Bragg's Law gives simple relationship between lattice geometry and diffraction angle, which means diffraction peaks are detectable at only specific diffraction angles. Figure 1.8 shows typical diffraction pattern received by a line detector.

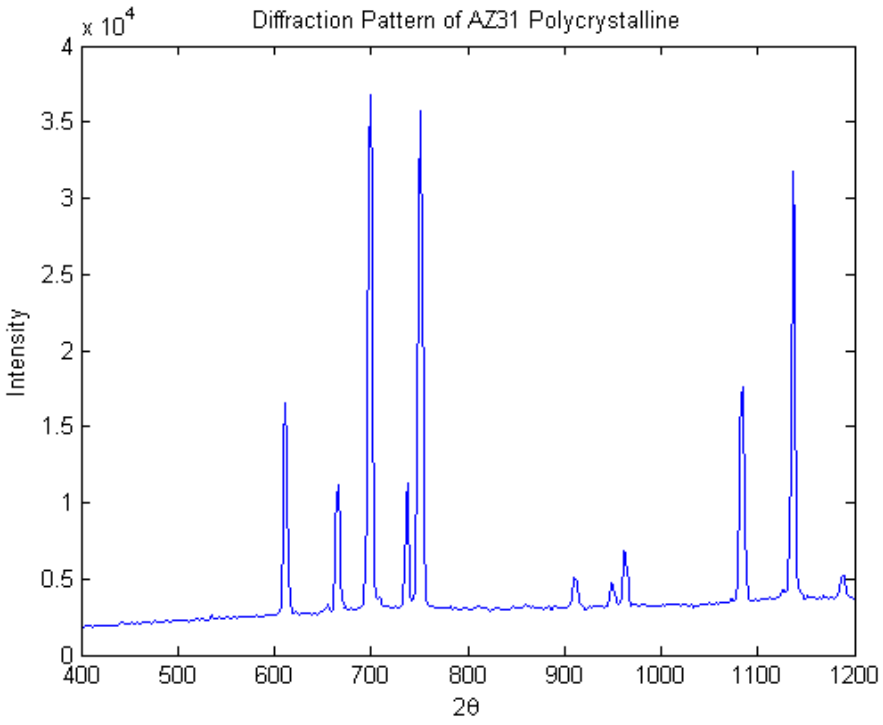

Figure 1.8: Diffraction Pattern of Polycrystalline AZ31

2D Xray diffraction is different from conventional XRD. With a two-dimensional detector, the detectable area is not limited to the diffractometer plane shown in Figure 1.7, but is extended to include part of the Debye diffraction ring.

Figure 1.9 compares different detectors: (1) Point detector only scan of one point at the 2D space (Left Diagram); (2) Line detector scan of a radial part of the 2D space (Right Diagram); (3) Area Detector show the whole ring detail (Background).

1.3.3 Coordinate Systems in 2D Xray Diffraction

In 2D Xray diffraction, transformation between different reference frames and the right coordinate choice is a prerequisite. From Figure 1.6, the right-handed Cartesian coordinate system is defined by $\mathbf{X}_L\mathbf{Y}_L\mathbf{Z}_L$. The direct X-ray beam travels along the $\mathbf{X}_L$ positive direction and $\mathbf{Z}_L$ is the upwards direction, which fixes $\mathbf{Y}_L$ direction by right hand law. In this thesis,

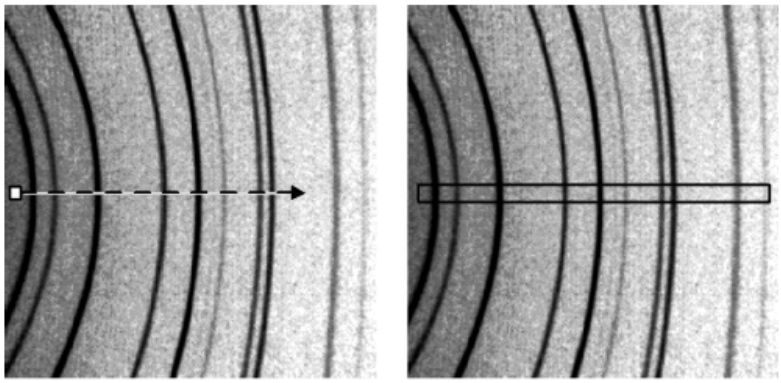

Figure 1.9: Comparison of Point Detector, Line Detector and Area Detector [24]

the Poulsen coordinate convention [25] is applied and the detail will be introduced in this subsection.

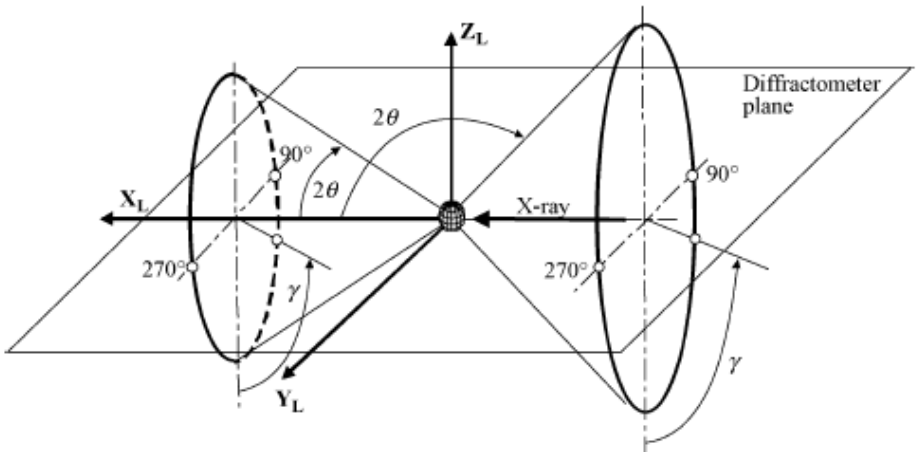

Figure 1.10: Illustration of the Geometry Defination of Diffraction Rings in Laboratory Axes [23]

1.3.3.1 General Geometry Conventions in 2D-XRD System in Bob's Convention

The diffraction space contains the information of crystal structure and wavelength of the beam. The apex angles of the cones are determined by the 2θ values derived from Bragg Law. Twice the value of 2θ gives the apex angles of forwards diffraction cones, and twice of $180 - 2\theta$ gives the values for 'backwards' one. The γ angle is defined as the azimuthal angle from the origin at the $-\mathbf{Z}_L$ direction of the incident beam. However, other different

conventions of γ were applied in different cases therefore it should be well defined before application. The diffraction space system is independent of the detector setup (or detector space) and sample orientation, which is only related to the laboratory coordinate systems. The transformation of diffraction space into the laboratory coordinate system is defined by the following equations

$$Y_L^2 + Z_L^2 = X_L^2 \tan^2 2\theta \tag{1.6}$$

$$s = \begin{bmatrix} s_x \\ s_y \\ s_z \end{bmatrix} = \begin{bmatrix} \cos 2\theta \\ -\sin 2\theta \sin \gamma \\ -\sin 2\theta \cos \gamma \end{bmatrix} \tag{1.7}$$

where

s is the unit diffraction vector,

2θ is the diffraction apex angle, and

γ is the azimuthal angle (as shown in Figure 1.10)

The detector position is defined by the sample-to-detector distance d and the detector swing angle α, provided the detector is assumed to be flat. Different positions of the detectors could generate circle, ellipse, hyperbola or parabola diffraction patterns. The following figure shows the relationship between detector position and diffraction pattern.

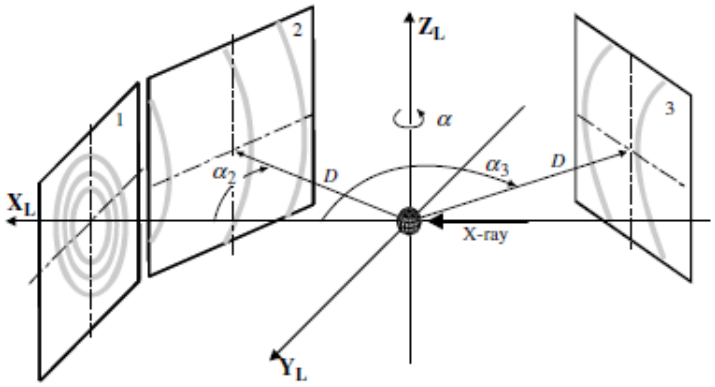

Figure 1.11: Different Detecor Positions in the Laboratory System [23]

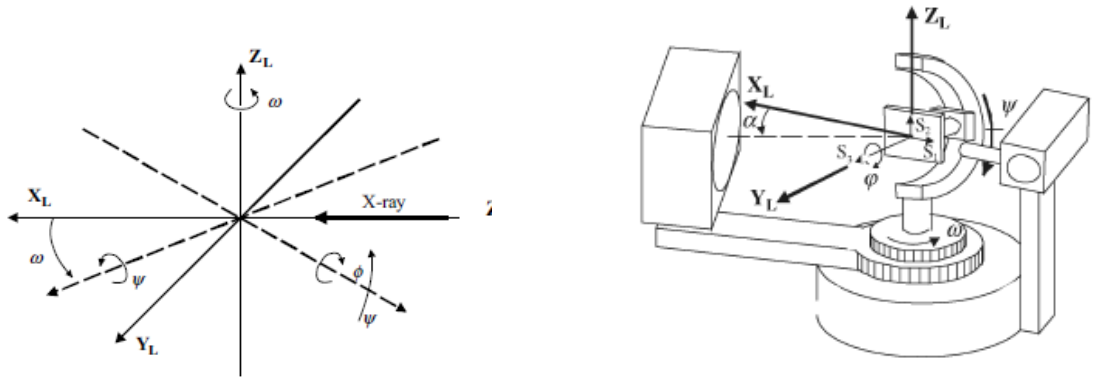

(a) Three Independent Rotations

(b) Goniometer Variation of Six Paramters in Sample Space

Figure 1.12: Scheme of Six Parameters [23]

There are six parameters in the sample space: three independent rotations (ω,ψ,ϕ) and three orthogonal translations ($\mathbf{X}$,$\mathbf{Y}$,$\mathbf{Z}$) (see Figure 1.12). Rotations orientations could be represented by Euler angles (classic Euler angles) or Tait-Bryan angles but there is no intrinsic difference between these conventions. In this thesis, classic Euler angles are applied. All these variations are realized by goniometer and the demonstration of the goniometer is shown in the figure.

The angular relationship between the laboratory coordinates $\mathbf{X}_L\mathbf{Y}_L\mathbf{Z}_L$ and the sample coordinates $\mathbf{S}_1\mathbf{S}_2\mathbf{S}_3$ are a 3×3 matrix. $\mathbf{A}$ designates the transformation from the laboratory coordinate to the sample coordinates.

$$\begin{aligned}\mathbf{A} &= \begin{bmatrix} a_{11} & a_{12} & a_{13} \\ a_{21} & a_{22} & a_{23} \\ a_{31} & a_{32} & a_{33} \end{bmatrix} \\ &= \begin{bmatrix} -\sin\omega\sin\psi\sin\phi - \cos\omega\cos\phi & \cos\omega\sin\psi\sin\phi - \sin\omega\cos\phi & -\cos\psi\sin\phi \\ \sin\omega\sin\psi\sin\phi - \cos\omega\cos\phi & -\cos\omega\sin\psi\sin\phi - \sin\omega\cos\phi & \cos\psi\sin\phi \\ -\sin\omega\cos\psi & \cos\omega\cos\psi & \sin\psi \end{bmatrix}\end{aligned} \tag{1.8}$$

The unit vector $\mathbf{h}_s$ is the diffraction vector expressed in the sample coordinates and $\mathbf{h}_L$ is the one in laboratory coordinates. The relationship in between is given by the equation:

$$\mathbf{h}_s = \mathbf{A}\mathbf{h}_L \tag{1.9}$$

Combined with the Bragg Law, the scattering vector corresponding to a pixel is given by:

$$\mathbf{H} = \frac{2\sin\theta}{\lambda}\mathbf{h}_s \tag{1.10}$$

In summary, the laboratory coordinate system is the foundation of all three spaces. The diffraction space are determined by sample crystal structure, the wavelength of beam and material microstructure. The detector space depends on the 2D detector shape, location and swing angle. The sample space is determined by the sample location and orientation. Change in detector space does not change the diffraction space, but alters the measured part of diffraction space and measurement resolution [23].

1.3.3.2 Poulsen Convention and Bunge Notation

In this thesis, the Poulsen convention is applied and the geometry definition differs from Bob He convention introduced in last subsection [24]. (**XYZ**) is the laboratory coordinate and (**X'Y'Z'**) is the crystal coordinate system. The Euler angle follows the following sequence (see Figure 1.13): (1) rotate about the Z'-axis through the angle φ_1, (2) rotate about the X-axis through the angle ϕ and (3) rotate about the Z'-axis through the angle φ_2.

Therefore the transformation from the laboratory coordinate to the sample coordinate should

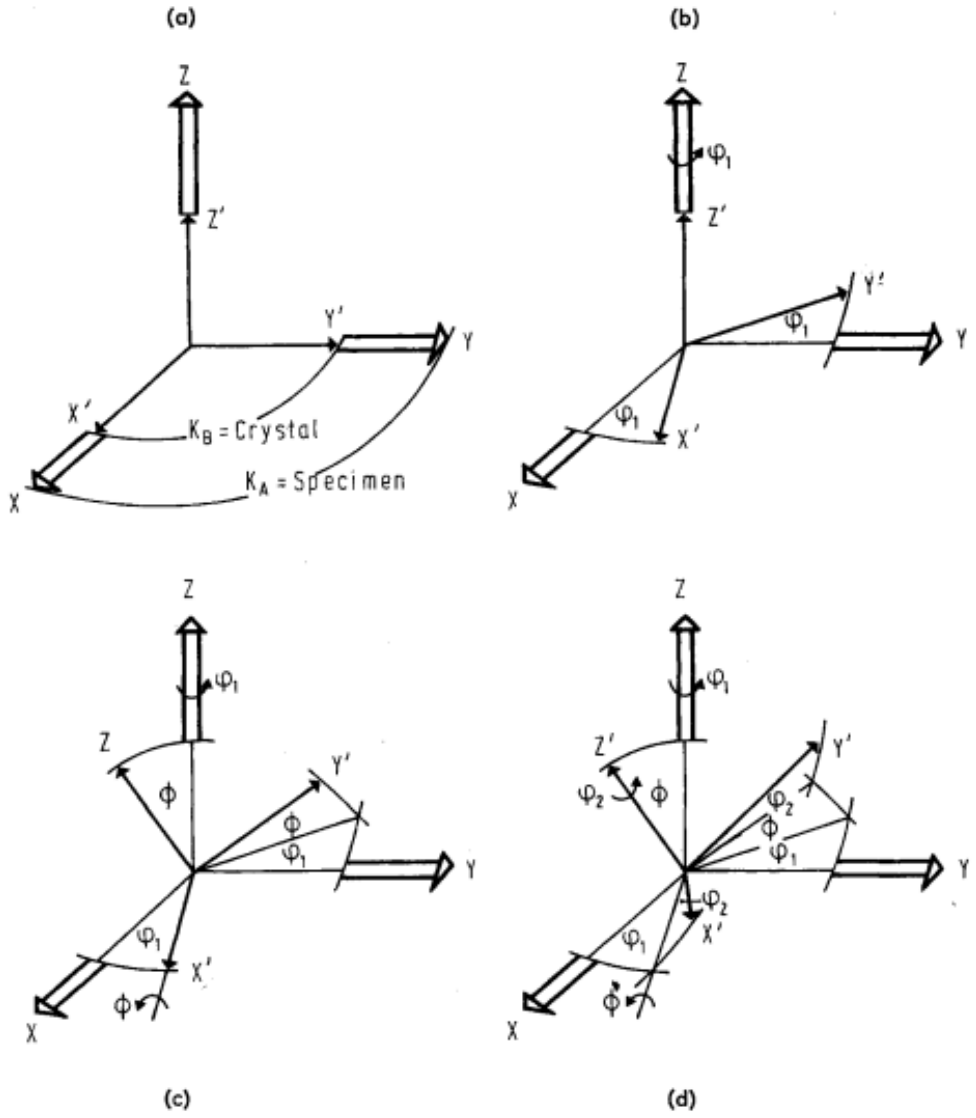

Figure 1.13: Definition of Bunge Euler Angles $\varphi_1\phi\varphi_2$ [27]

be rewritten as follows:

$$\mathbf{A} = \begin{bmatrix} \cos\varphi_1 \cos\varphi_2 - \sin\varphi_1 \sin\varphi_2 \cos\phi & \sin\varphi_1 \cos\varphi_2 + \cos\varphi_1 \sin\varphi_2 \cos\phi & \sin\varphi_2 \cos\phi \\ -\cos\varphi_1 \sin\varphi_2 - \sin\varphi_1 \cos\varphi_2 \cos\phi & -\sin\varphi_1 \sin\varphi_2 + \cos\varphi_1 \cos\varphi_2 \cos\phi & \cos\varphi_2 \cos\phi \\ \sin\varphi_1 \sin\phi & -\cos\varphi_1 \sin\phi & \cos\phi \end{bmatrix} \tag{1.11}$$

The diffraction tilt angle is still 2θ but the azimuthal angle is the mirror image symmetry to the Bob He's definition (see Figure 1.14). Therefore, the transformation between diffraction space and laboratory coordinate changes into

$$s = \begin{bmatrix} s_x \\ s_y \\ s_z \end{bmatrix} = \begin{bmatrix} \cos 2\theta \\ -\sin 2\theta \sin\eta \\ \sin 2\theta \cos\eta \end{bmatrix} \tag{1.12}$$

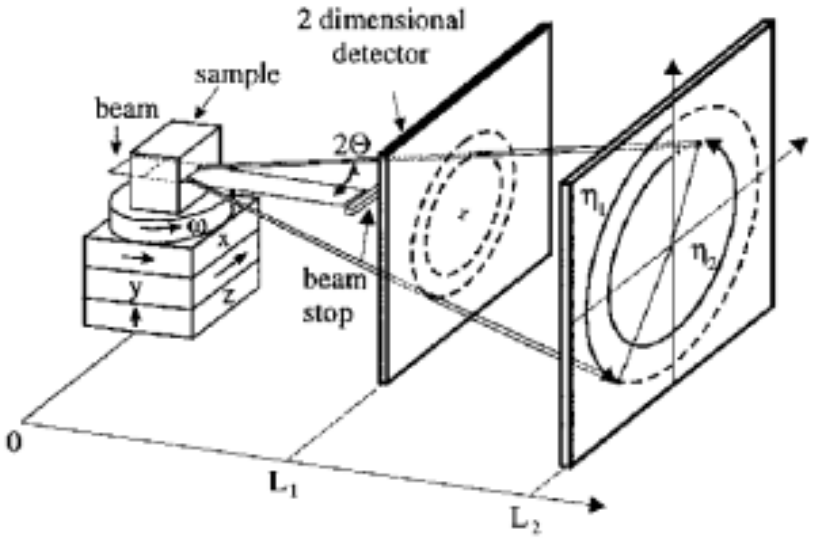

Figure 1.14: Poulsen Geometry Convention: (1) η is the azimuthal angle, (2) 2θ is the diffraction tilt angle and (3) ω is the sample rotation [25]

1.3.4 Synchrontron Radiation

In the last few years, synchrontron radiation is widely used in material science. Conventional beam sources could not penetrate much depth of the specimen, therefore it is not possible to study the whole cross-section of the specimen at one time. The reason lies in several factors:

1. energy absorption by specimen
2. wavelength matches lattice scale
3. energy of beam source

Therefore, the whole cross-section information requires the right size of specimen and highly-energized and dense beam source. The relationship between atomic number of element solids and X-ray Absorption is shown in the following figure and according to the diagram, the right energy for mm size specimen is about 50 keV to 100 keV [26].

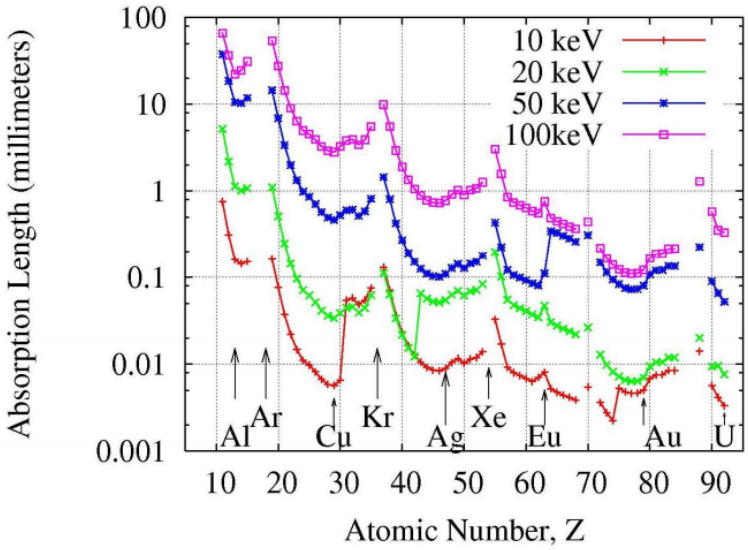

Figure 1.15: X-ray Absorption Lengths in Elemental Solids [26]

"In situ" typically refers to a method of data collection or sample manipulation without exposure to environment. Argonne National Laboratory is one of the several third generation

(a) Advance Phonton Source

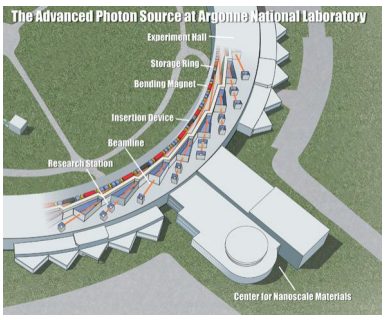

(b) Configuration of High Energy Beam Line

Figure 1.16: Argonne National Laboratory Synchrotron [26]

synchrotron radiation sources. Both near-field and far-field in situ 2D-XRD experiments are conducted at APS 1-ID High Energy Beamline.

1. Far-field Xray Diffraction: essentially a rotating-crystal method using high-energy synchrontron x-ray and an area detector at a relative large distance in unit of meter (Figure 1.11(b)).

2. Near-field Xray Diffraction: image diffracted beams from planar grain cross-sections during 180 degrees ω rotation and $\delta\omega$ integration intervals with a very close detector on the order of millimeter (Figure 1.11(a)).

Far-field high-energy diffraction microscopy is the method to investigate the embedded neighborhoods of grains. For each grain in an studied polycrystalline volume, far-field HEDM offers volume-averageed lattice orientations, lattice strain tensors and center of mass coordinates. Margulies et al. [28] and Martins et al. [29] developed the technique of obtaining fully 3D lattice strain tensors for individual grains when the specimen is loaded in situ. Mosciki et al. [30] and Oddershede et al. [31] managed to compute lattice strain tensors for large grains aggregates (about 1000 grains). The Miller group presented a method for sorting an embedded neighbourhood of grains by orientation indexing and then using the center of intensity to compute the lattice strain for individual grains [32].

The near-field HEDM technique was developed by Suter et al. [33, 34] and Ludwig et al.

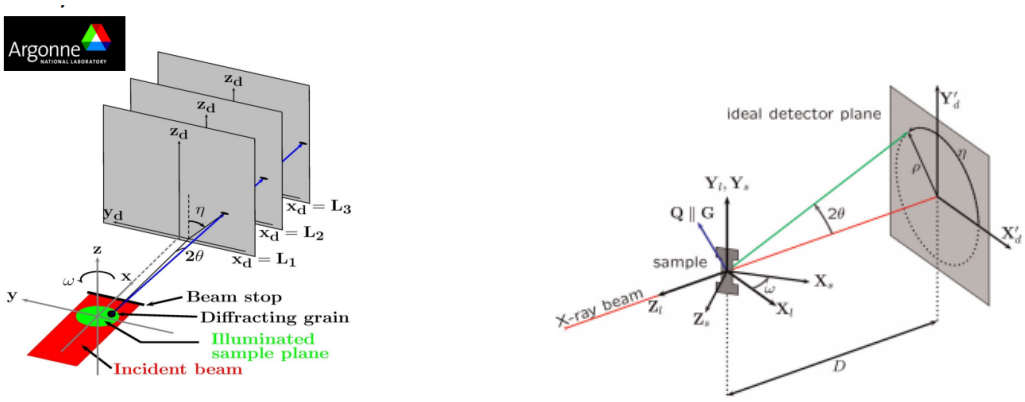

(a) Near-field HEDM Setup [36]

(b) Far-field HEDM Setup [32]

Figure 1.17: HEDM Experiment Configuration

[35]. Near-field microscopy focuses on the spatial resolution at the cost of strain resolution by introducting a detector working distance on the same order of 1-10mm. This technique offers a weapon to investigate the spatial orientation map rather than average grain orientation, which means subgrain detail is captured [35, 32]. A multi-detector instrument enables simultaneous data acquisition from both near-field and far-field methods.

1.4 Stress Relaxation of Metallic Material

Stress relaxation describes stress drop under constant strain when material undergoes plastic deformation. In elastic stress tests. when the crosshead stops, the total strain rate $\dot{\epsilon}_\Sigma$ is set to zero. The total strain rate is composed of two part, elastic strain rate and plastic strain rate, which means in the stress relaxation process $\dot{\epsilon}_p = -\dot{\epsilon}_e = -\frac{1}{E^*}\frac{d\sigma}{dt}$ [37]. (E^* is the combined elastic modulus from load frame and specimen, while E designates the specimen modulus.) Therefore, stress drop rate is reasonable to be assumed to be proportional to the plastic strain rate.

$$-\frac{d\sigma}{dt} = \dot{\epsilon}_p E^* \tag{1.13}$$

There are two possible mechanisms to explain dislocation stress relaxation: a) for high strain rate or low temperature – dynamic retardation of the system with dislocation atmospheres and b) for low strain rate or high temperature – dislocation anchoring and breaking [38].

Kamyshanchenko et al. [39] applied acoustic emission method to the indentation mechanical test to study the stress realaxation and concluded that a slip in the accommodation zones produces stress relaxation because of the formation and growth of twinned interlayers.

Pavel and Lukac [40] conducted stress relaxation tests to determine parameters of a possible thermally activated process in AZ31 in constant strain rate with temperature from room temperature to 300^{o}C. The whole process is probably that glissile dislocations in the non-compact planes (source) cancel out each other in the subsequent process (sink).

CHAPTER 2

EXPERIMENT

2.1 Experimental Setup

2.1.1 HEDM Apparatus and Implementation

The high energy diffraction microscopy (HEDM) was conduct at Argonne Nationally Laboratory Advanced Photon Source (APS) beamline 1-1D. The experiment setup is mainly composed of three parts (see Figure 2.1):

1. Beam Source – inlet electron, undulator and monochromator
2. Load Frame – adjustable rotation desk and load frame
3. Detector – Hydra Detector System

Several hutches were located in series and the beam ejected from undulator (see Figure 2.2). The function of undulator is to transform inlets electron into exit's electromagnetic pulse through a small slit. The device consists of a periodic structure of dipole magnets and therefore an alternating static magnetic field is generated, which is used to trigger electron collimation and oscillation for energy radiation. The high-energy monochromator was set in front of white beam slits to filter the undesirable wavelengths. The beam energy was tuned to 80.685eV.

The load frame (see Figure 2.3) of this experiment was designed by Cornell's group and the crosshead is driven by the motor at the top. The motor control for the loading is open loop therefore strain should not zero during the relaxation.

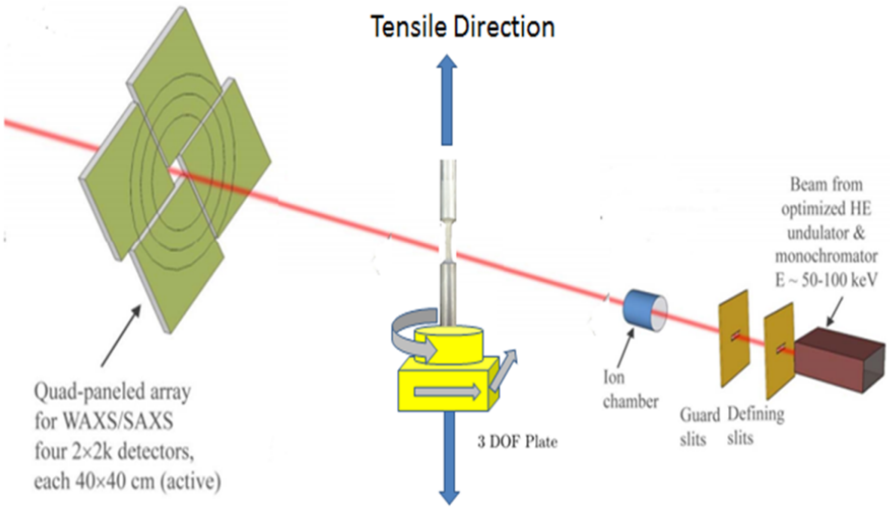

Figure 2.1: Scheme of Experimental Setup

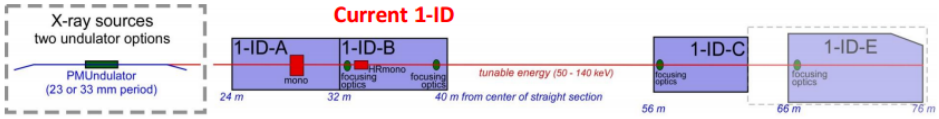

Figure 2.2: Scheme of hutches, beam and undulators [41]

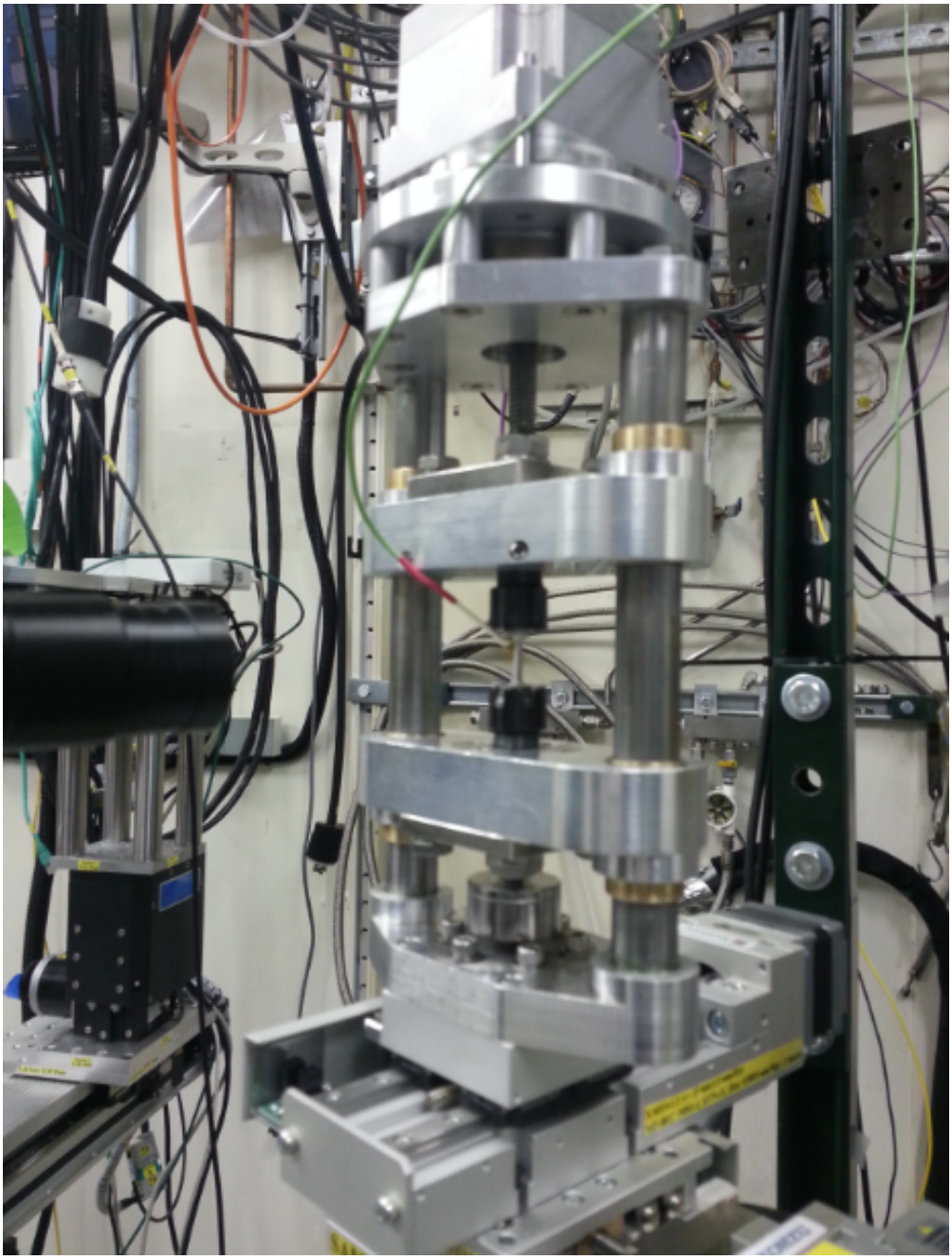

Figure 2.3: Load Frame

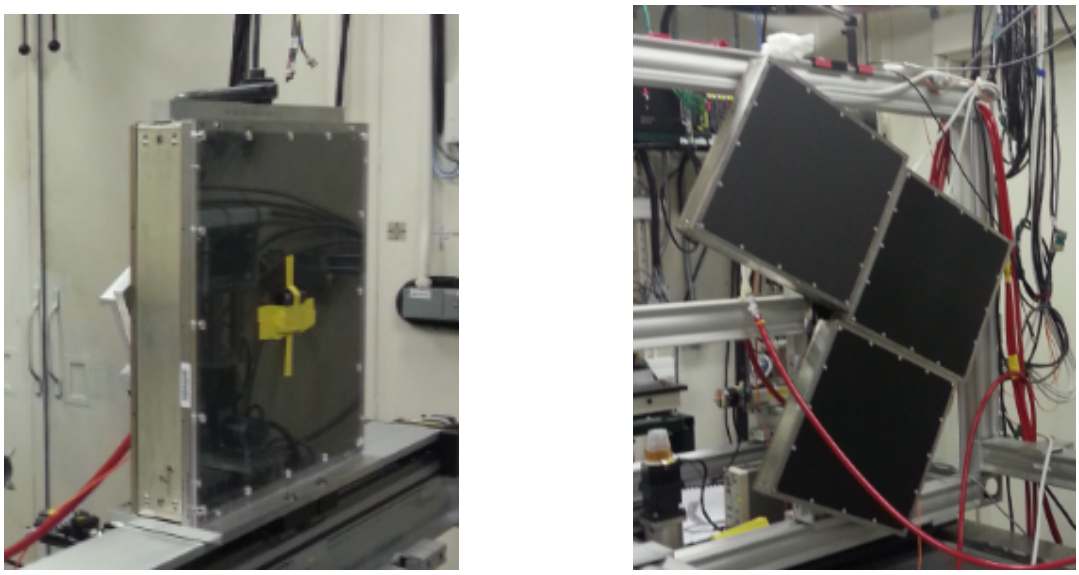

(a) GE Detector (b) Hydra Detector

Figure 2.4: GE Detector and Hydra Detector System

The GE detector (see Figure 2.4) uses a plate of amorphous silicon to detect high-energy diffraction and the Hydra detector consists of three (or four) GE detectors which gives larger spatial resolution for far field experiment. The dimension of the hydra is 410mm×410mm and the detector is composed of 2048×2048 pixels, the size of which is 200 microns [42].

2.1.2 Distance and Center Calibration

In order to collect data more precisely, calibration was very important because both the dimension of the grain or the displacement were in the same order of magnitude, which could result in loss of a target grain during experiment. On the other hand, calibration of Hydra detectors was more complicated than that of single detector since three individual calibration steps were needed to get separate distances of each detector. Therefore, two different calibrations were done during the experiment:

Detector Distance Calibration was achieved by powder diffraction of cerium (CeO_2). The powder specimen diffracted the incident beam into concentric ring on the detector. Since the crystal structure of the cerium was known in advance, then the distance from the sample to the detector could be fitted by algorithm (Ring Generation Algorithm in

the next chapter). For the Hydra system, the calibration should be done three times because each detector only swept only 90 degrees. The whole process could be realized by the software Fit2D.

Beam Center Calibration is the process to confirm the right diffraction region of interest. The beam ejected from the monochromator had limited size which could only hit a cross section of the specimen. However, in the experiment, the lower cross-head was fixed and the upper one ascended, which translated the cross-section of interest during the tensile test. Therefore, the adjustable desk descended the whole test frame to compensate the displacement. In order to get the right displacement, the surface texture following from EDM served as a random speckle pattern and monochromatic camera was set to capture real time condition of the pattern which could be used to correlate the displacement field of the whole gage length.

2.1.3 Specimen Detail

The specimen was manufactured by electric discharge machining and the dimension was 2mm×2mm. The gage length was 12.1mm and it was synchrotron-penetrable. The specimen was cut from the 13.6mm-thickness cold-rolled and annealed plate and the tensile axis is parallel to transverse direction. The plate should have a basal texture and the plate detail was shown in Figure 2.7.

The stress-strain curve (Figure 2.8) of the specified orientation showed the basic mechanical properties of material. The yield stress was about 150MPa and after that the material was in hardening domain. The gap in the plasticity indicated strain rate change (from 10^{-4} to 10^{-5}) and AZ31 was rate-sensitive.

2.2 Data Analysis

In order to get meaningful time series of the peak information, an effective algorithm should isolate individual peaks from the detector image, combine sub-images into the one big pic-

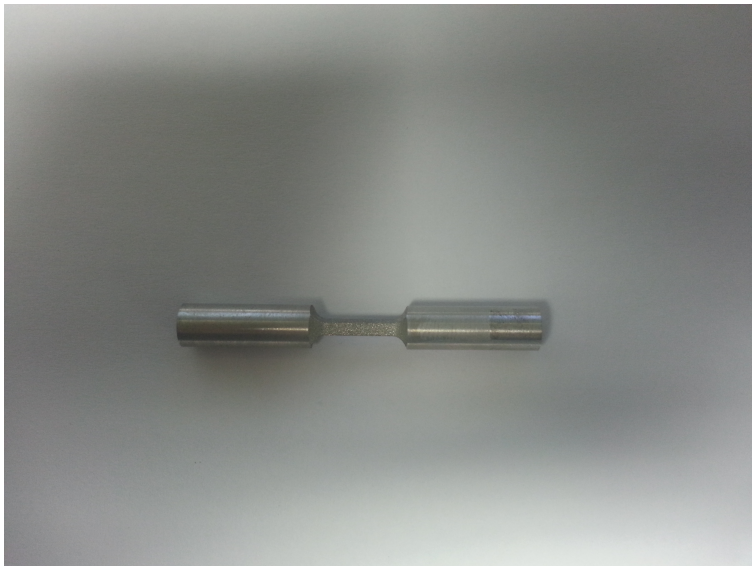

Figure 2.5: Picture of AZ31 Tensile Specimen

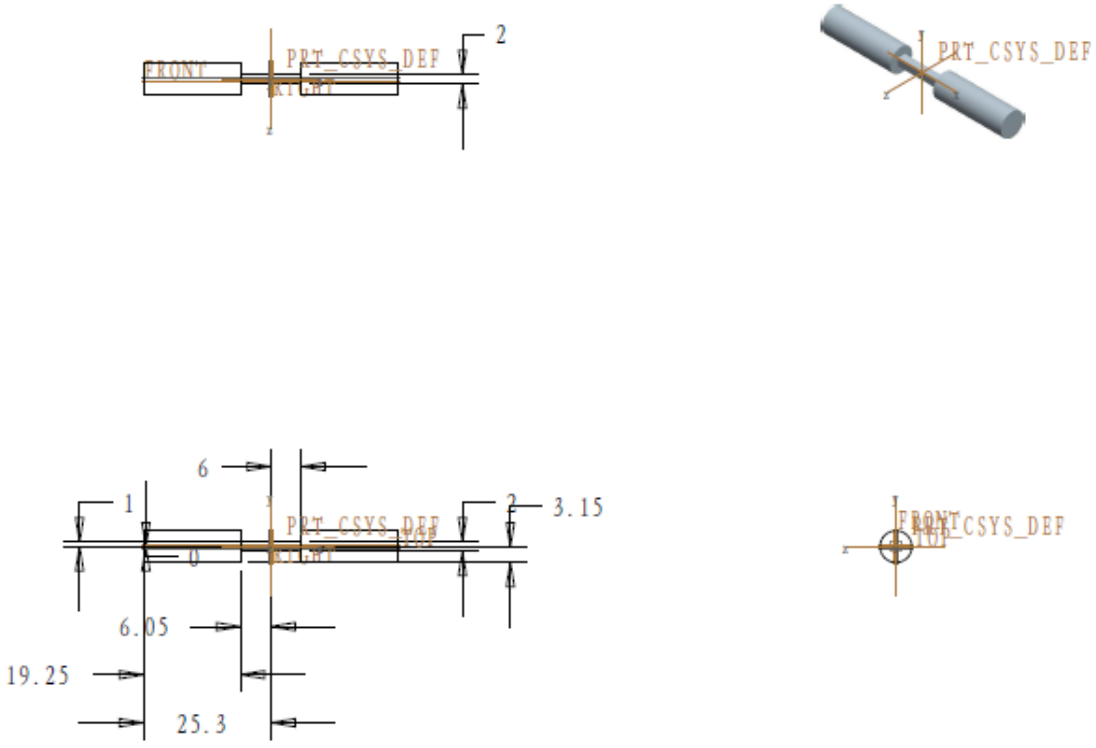

Figure 2.6: Dimension of Specimen

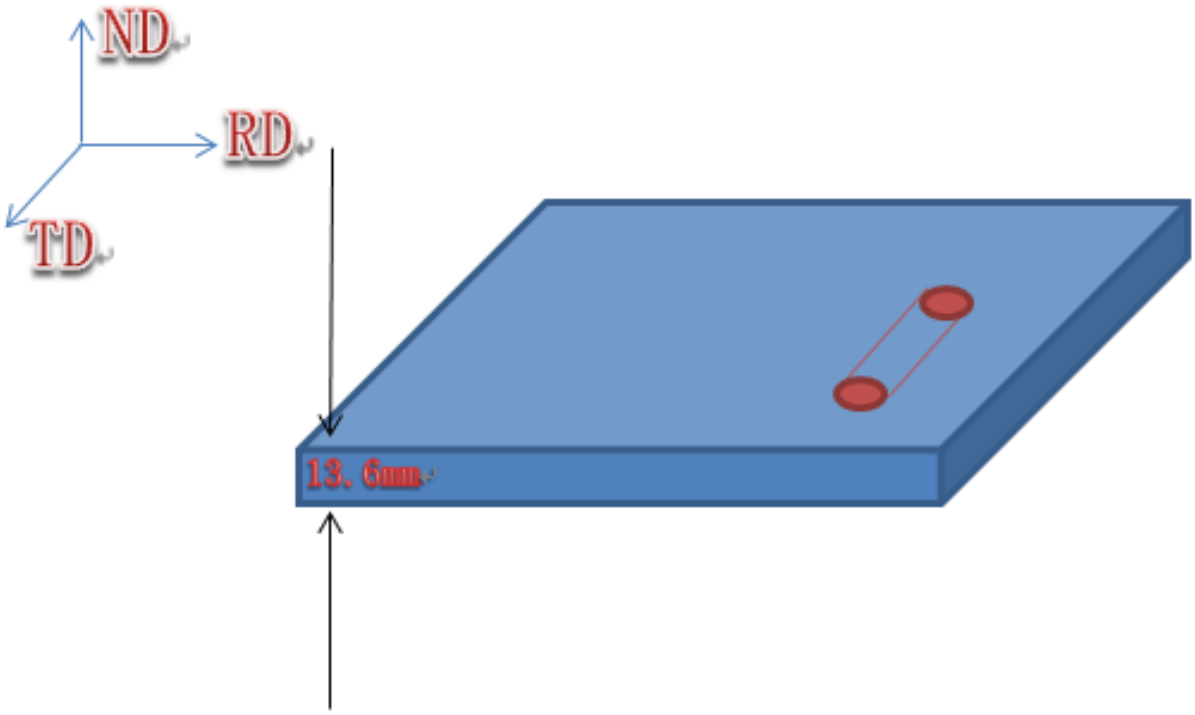

Figure 2.7: Cold Rolled Plate and Specimen Direction

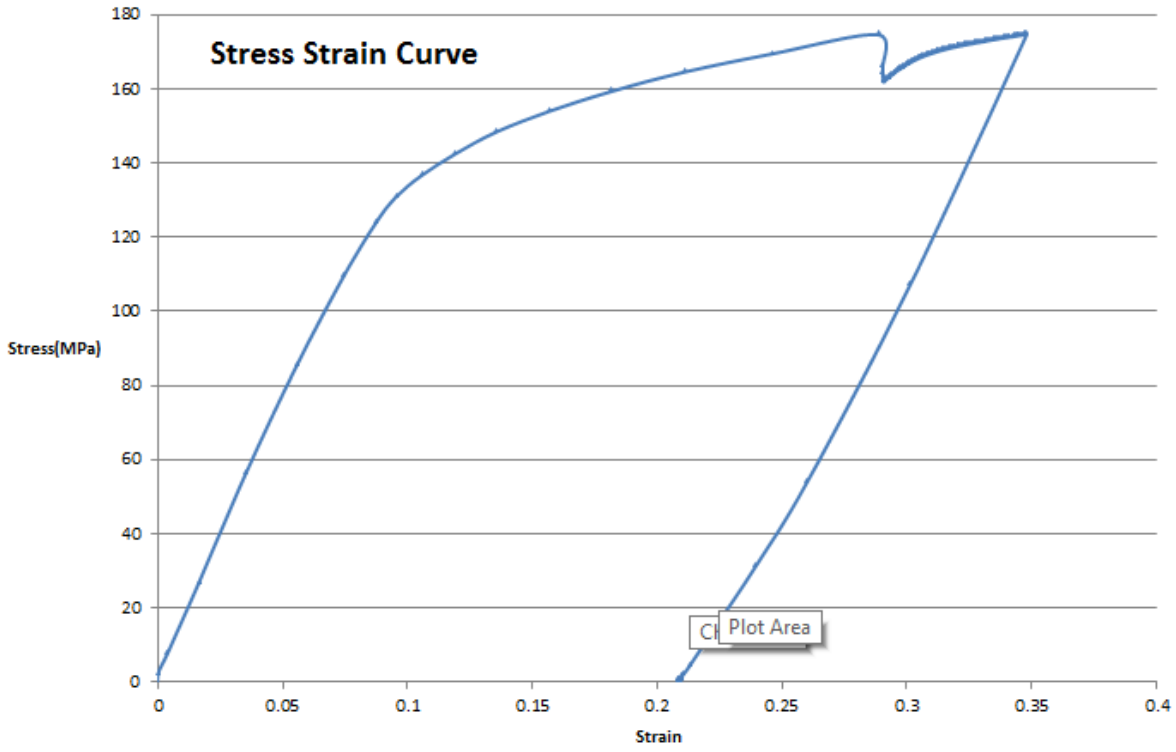

Figure 2.8: Stress Strain Curve of AZ31 Alloy

ture, repair the lost image resolution (detail in the subsection 'Pre-process of Images'), trace the trajectory of peak centroid, transform the detector space information into strain time series and complete fitting of reflection ring. Four different tensile loadings were analyzed and loading time series are shown as follows.

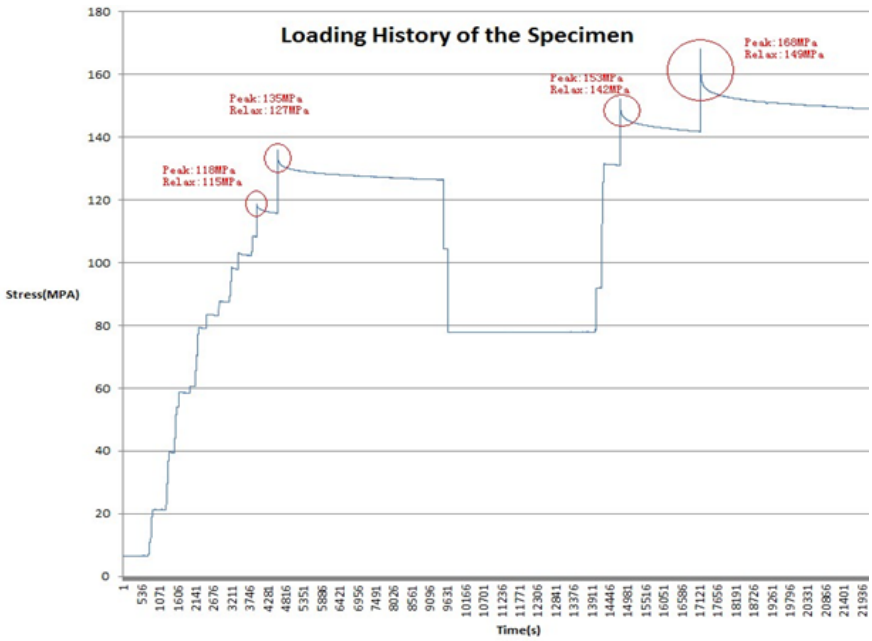

Figure 2.9: Loading Time Series (Four Circle Indicates Four Load Steps)

For every loading step, there are two important values – the maximum load and the load drop during relaxation. Four peak loads are 118MPa, 135MPa, 153MPa and 168MPa and their associated final loads are 115MPa, 127MPa, 142MPa and 149MPa. Therefore, the load drops are 3MPa, 8MPa, 11MPa and 19MPa. Two phenomenon are observed. The yield strength of the specimen is about 150MPa and the more plasticity, the greater relaxation.

2.2.1 Pre-processing of Images

The analyzed images are pre-processed by several techniques. The intensity saturation from previous frame in some detector pixel could be an obstacle of image analysis and in order to reduce this intensity lagging error, arithmetic averaging of the image is applied.

$$\bar{P}_n(x,y) = \frac{1}{3}\sum_{n-1}^{n+1} P_i(x,y) \tag{2.1}$$

$\bar{P}_n$ is the nth frame of after-processed image, and

P_i is the ith frame of before-processed image

The images from separate detectors are rotated and combined together. For each detector, the pattern looks identical and in order to get the combined images, rotation and translation for separate detectors are necessary. The rotational angles for three GEs are -62.6, 117.7 and 207.7 degrees respectively. X_G and Y_G represent the global coordinate and X_i and Y_i $(i = 1, 2, 3)$ are for individual detectors.

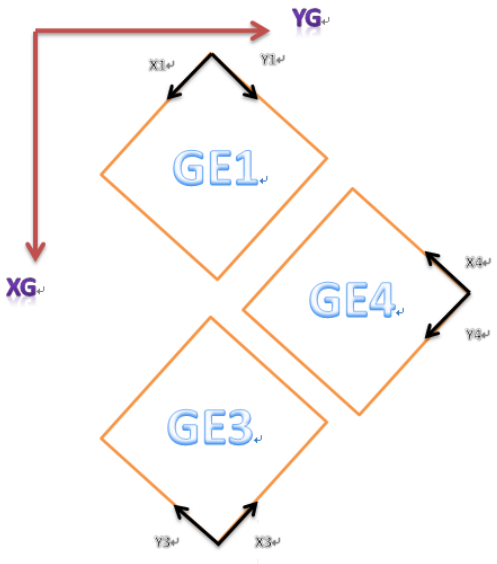

Figure 2.10: Global Coordinate for Combined Image and Local Coordinates for Separate Detectors

The size for individual detector pattern is 2048 × 2048 pixels and for the combined image, the final size is 2995 × 2995.

Moreover, the rotation of integer index image would lose some information because the index

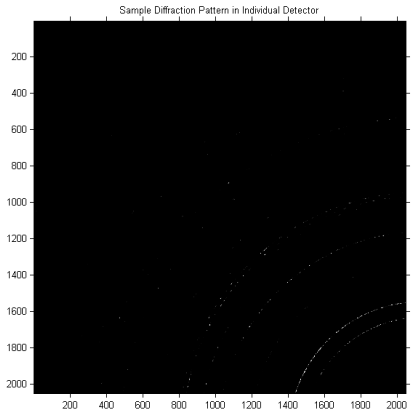

(a) Individual Detector Diffraction Pattern

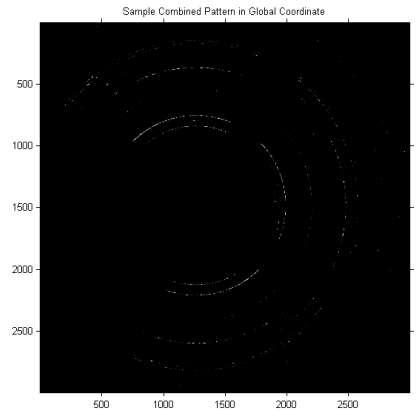

(b) Combined Diffraction Pattern After Gaussian Filtering

Figure 2.11: Comparison of Diffraction Patterns

after rotation is unlikely to be integer, which causes many non-value pixels. Therefore, a smoothing technique is applied to partially recover the image resolution. Gaussian filtering is applied in the algorithm. A Gaussian kernel coefficient are sampled from the 2D Gaussian function:

$$G(x,y) = \frac{1}{2\pi\sigma^2} e^{-\frac{x^2+y^2}{2\sigma^2}} \tag{2.2}$$

The numbers inside the kernal obey the normal distribution and this kernel is used to

```
>> H = fspecial('gaussian',5,0.8)

H =

    0.0005    0.0050    0.0109    0.0050    0.0005
    0.0050    0.0522    0.1141    0.0522    0.0050
    0.0109    0.1141    0.2491    0.1141    0.0109
    0.0050    0.0522    0.1141    0.0522    0.0050
    0.0005    0.0050    0.0109    0.0050    0.0005
```

Figure 2.12: Sample 5×5 Gaussian Kernel for Image Convolution

complete image convolution. After convolution, lost pixel intensity could be computed from

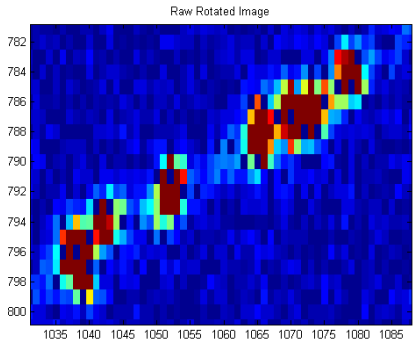

(a) Raw image:lost pixels found inside the peak

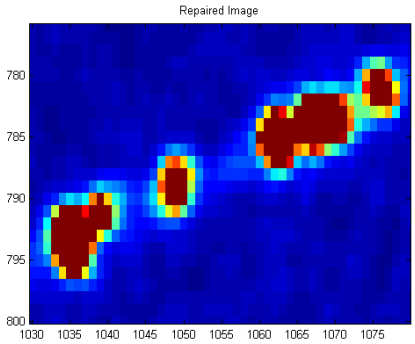

(b) Repaired image: no defect observed inside the peak

Figure 2.13: Effect of Gaussian Filtering

its neighboring pixels. However, since this technique is a blurring operation, the standard deviation of the image should be carefully selected. If the σ is overestimated, the image could be very blurry. On the contrary, if the σ is too small, the pixel repair will fail [43].

Figure 2.13 shows the effect of Gaussian filtering and the raw image is clearly full of zero-value pixels inside high-intensity region. On the contrary, the post-processed image contains all information and the transition between peak and background is smooth.

2.2.2 Peak Isolation Algorithm

Ideally, the constructive diffraction of two parallel atomic layers should be a point. However, real diffraction peaks span from a point into some area as shown in Figure 2.14. Like the weight centroid of a rigid body, the intensity centroid of a diffraction peak is defined in a similar way (see Formula 2.3). Intensity of peak is determined by the structure factor of crystal lattice and the broadening of the peak region is very complicated and out of thesis scope. This section highlights the methodology to calculate all of the intensity centroids in every frame.

For any given frame, the first job is to set a reasonable threshold to filter noise. However, if threshold is large, target peaks of higher order reflection would be ignored because of their

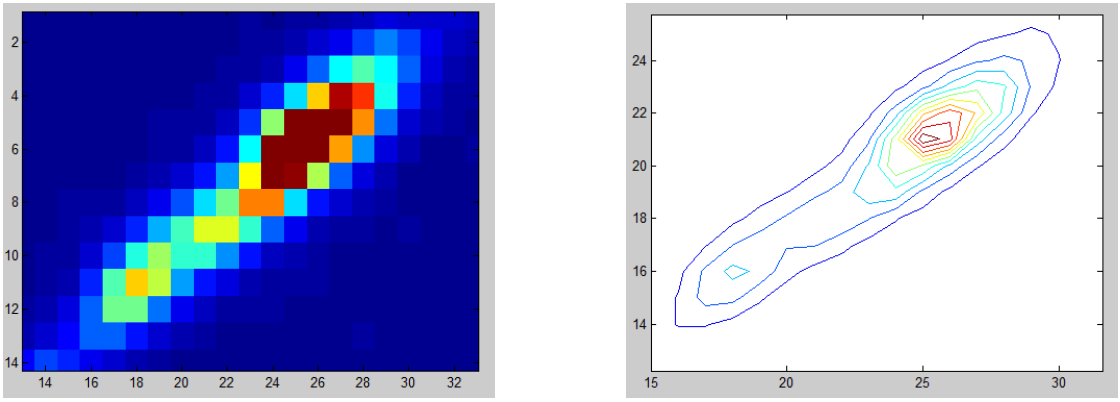

(a) Example of a diffraction peak

(b) Contour of a diffraction peak

Figure 2.14: Example of a diffraction peak

low intensity value. There are two different threshold-setting methods:

Global Threshold (for the whole image) In this experiment, 25 to 35 is a very reasonable value to observe the whole picture. As shown in Figure 2.15, the threshold of 50 eliminates almost all higher order reflection peaks but threshold of 25 keeps enough information. This global threshold is applied in peak positioning process and the speed is faster.

Local Threshold (for sub-image) After locating the rough peak position, the dynamic study of the peak can be processed locally. In a small subregion, the pixel intensity far away has no influence on local sub-image and high threshold is applied for lower order reflection peaks. In this case, one-fourth of the maximum intensity is set as the threshold. This criterion is used in quad-plots in appendix but it requires more time to loop over peaks. The pros and cons of threshold criteria are discussed in 'Algorithm Sensitivity' part.

A second step is to convert the grayscale image to a binary image, because this reduces the complexity of code to check the connectivity of pixels. The whole peak isolation process is analogous to the rice counting problem [44]. In the binary image, there are only two different regions: a connected white region and a black background. Then the connected region could

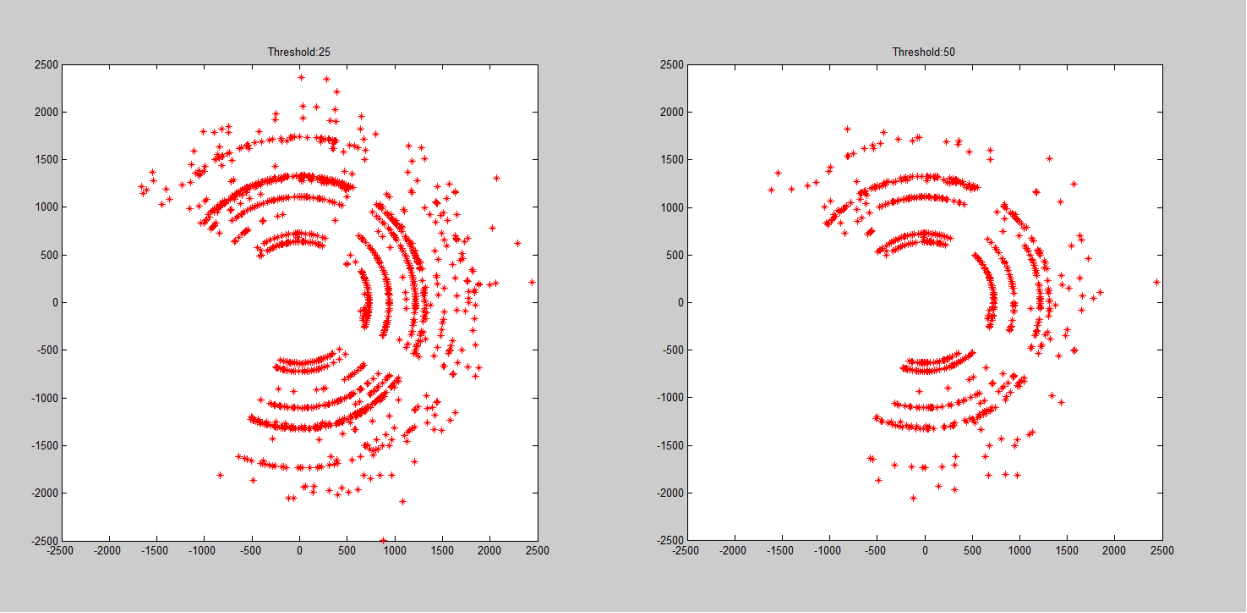

Figure 2.15: Effect of threshold on peak isolation result

be recorded inside a structure variable as individual objects after looping over non-zero pixels in the binary image by the function **bwconncomp**. In this algorithm, the two dimensional eight-connected neighborhood is applied as the second parameter as shown in Line 9 of the function **GetCentroidThresholdDim**. In Matlab, the function **regionprops** returns geometric information of the objects inside the geometry and the pixel-index-list offers us the map which enables us to get the pixel intensity in the original image.

```
1 level=graythresh(image);    % Automatically thresholding the image to ...
      filter the noise
2 bw = im2bw(image,level);     % Convert the image from grayscale to a ...
      binary image
```

Finally, the intensity centroid computation can be analogy to the mass centroid formula:

$$\mathbf{r}_c = \frac{\sum_{i=1}^{n} I_i \mathbf{r}_i}{\sum_{i=1}^{n} I_i} \tag{2.3}$$

where I_i is the intensity of the ith pixel inside the peak and

$\mathbf{r}_i$ is the position vector of the ith pixel.

The peak isolation algorithm is realized by the following code:

```
function [CentroidMatrix,GeoData] = GetCentroidThresholdDim(img,thre)
% img: the input grayscale image
% thre: the threshold used to filter the image
i1=img>thre;
i1=i1.*img;      % Thresholding according to manually set intensity
level = graythresh(i1);  % Thresholding according to image property
bw = im2bw(i1,level); % Convert the image from grayscale to a binary image
bw = bwareaopen(bw, 8);   % Erasing all connected region whose size is ...
    smaller than 8
AllInfo=bwconncomp(bw,8);
GeoData=regionprops(AllInfo,'PixelIdxList','PixelList');   % Get the ...
    geometric information of region
CentroidMatrix=[];
for i=1:AllInfo.NumObjects
    sub=GeoData(i).PixelList; %Intensity Centroid Computation
    [a,b]=size(sub);
    NumX=0;NumY=0;
    Den=0;
    for j=1:a
        tran=sub(j,:);
        index1=tran(1);
        index2=tran(2);
        Value=img(index2,index1);
        NumX=NumX+index1*Value;
        NumY=NumY+index2*Value;
        Den=Den+Value;
    end
    CentroidMatrix(i,:)=[NumX/Den,NumY/Den];
end
end
```

2.2.3 Peak Movement Trajectory Tracing Algorithm

Before introducing the algorithm of peak movement trajectory tracing, the data structure of the identified peaks is first clarified in the following. For each frame, a list of coordinates is developed through the peak isolation algorithm. The ith centroid in the nth frame is characterized by I_i^n $(i = 1, 2, 3.....m)$. An additional data structure is used to record all the information for each trajectory. Several parameters are recorded inside the structure (1) Index of the trajectory ; (2) Counter of peak recorded throughout all frames ; (3) Coordinate list of traced centroid ; (4) Latest position of the centroid. These data structures are given by the following scheme:

The logic of peak tracking centers upon pairing the frame centroid coordinate with history

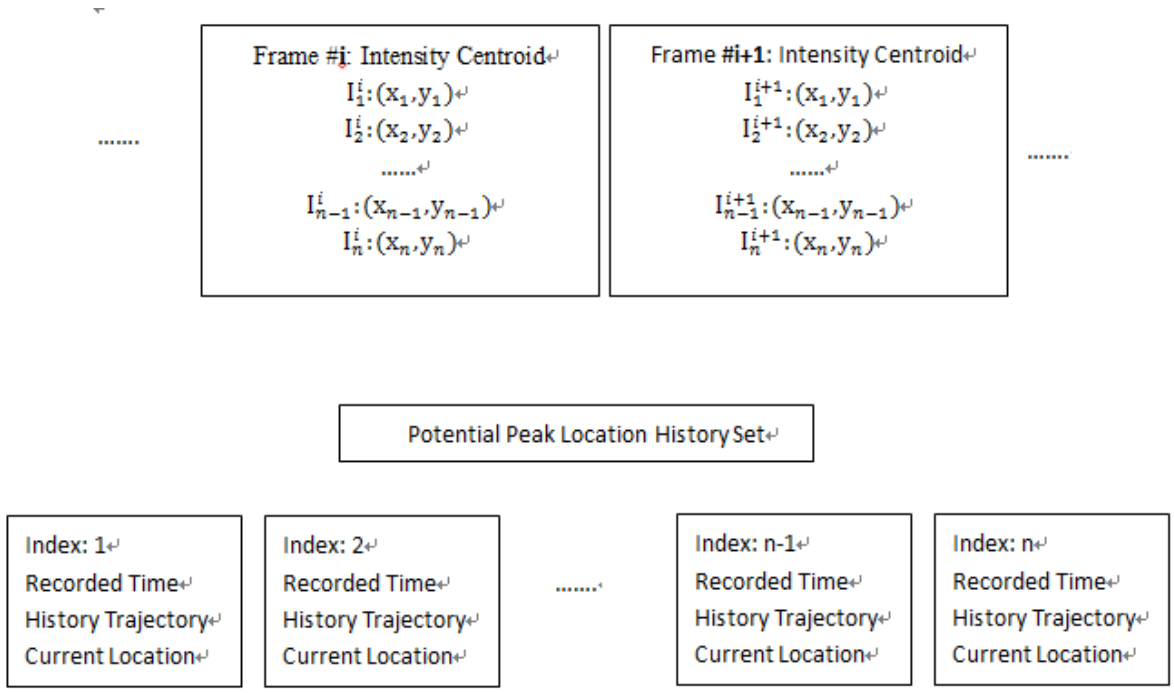

Figure 2.16: Data Structure of Trajectory Tracing Algorithm

trajectory coordinate. There are three loops inside this algorithm – looping throughout all frames, looping throughout all centroids inside one frame and looping over the trajectories recorded. Two points of comparison are applied in the third loop. One test is to investigate

whether the centroid matches the current position for the trajectory. The criteria applied is whether the distance in between is smaller than 4 pixels. If yes, three actions will be taken: (1) the record counter is incremented ; (2) Current position is updated; (3) The centroid is appended to the trajectory coordinate list. The other judgement is as to whether all of the trajectories have been examined. If yes, then a new trajectory object is created according to the current centroid coordinate and the counter is set to one.

2.2.4 Mg Ring Generation Algorithm

During the analysis, rings related to different plane families are the important reference of peak positions in the detector space. This information is applied in the strain change computation, the center of detector calibration and overall ellipse fitting. The basic algorithm could be generalized into several formulas. The realization of ring generation is described in this section.

For a hexagonal close-packed lattice, the distance between parallel $\langle hkl \rangle$ planes could be computed by the following formula [45]:

$$\mathbf{D}_{hkl} = \frac{1}{\sqrt{\frac{4(h^2+hk+k^2)}{3a^2+\left(\frac{l}{c}\right)^2}}} \tag{2.4}$$

h, k, l is the Miller Index and
a, c are the h.c.p Lattice Parameter
Transformation from plane distance to diffraction angle is the next step and Bragg's Law is the key to get the desired angle. Moreover, a trigonometrical relation is applied to calculate the diffraction ring radius.

$$n\lambda = 2d_{hkl}\sin(\theta_{hkl}) \tag{2.5}$$

$$R_{hkl} = KD\tan(2\theta_{hkl}) \tag{2.6}$$

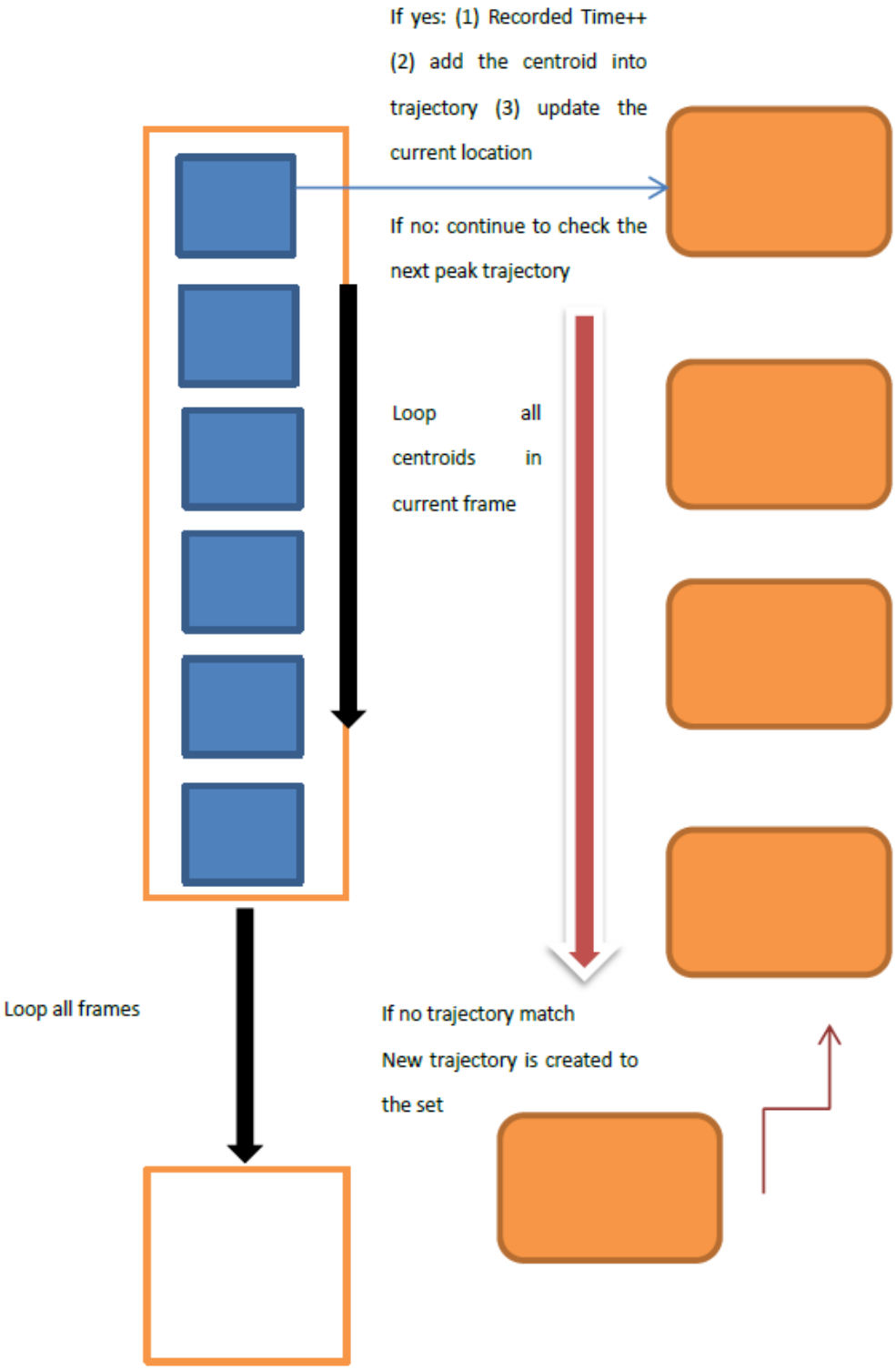

Figure 2.17: Scheme of Peak Trajectory Tracing Algorithm

where d_{hkl} is the distance between $\langle hkl \rangle$ planes

θ_{hkl} is the diffraction angle for $\langle hkl \rangle$ planes

R_{hkl} is the radius of $\langle hkl \rangle$ diffraction ring

D is the distance between detector and specimen and

K is the geometric constant related to unit transformation and detector resolution

The parameters used in the calculation are given in the appendix B. After transformation,

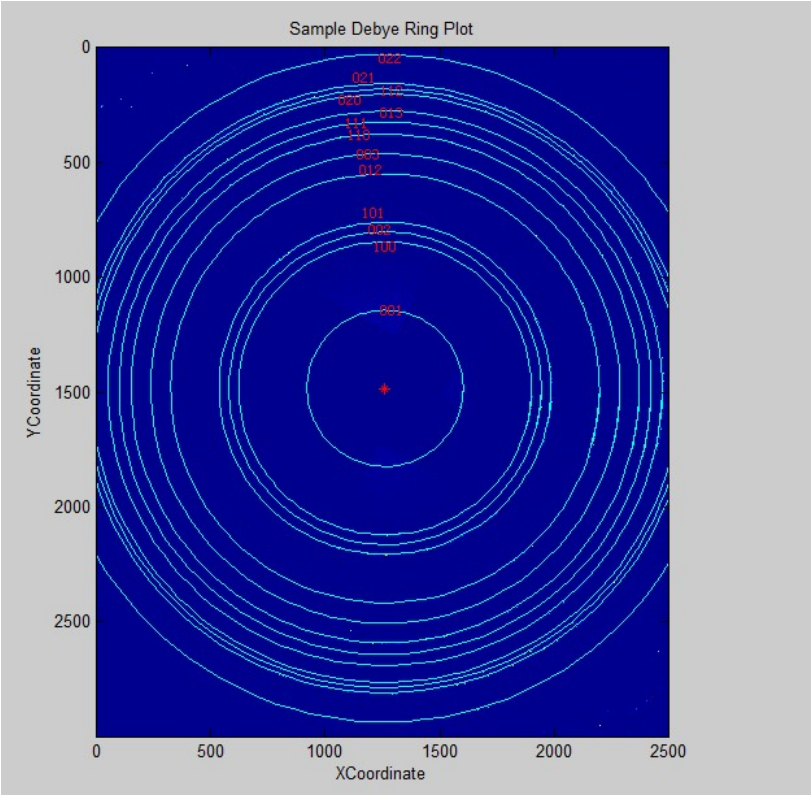

Figure 2.18: Debye Ring in Detector Space

the Debye ring could be fit into detector space and the inverse transformation will be also used in an average strain change computation.

2.2.5 Detector Center Calibration and Peak Grouping Algorithm

In order to analyze the concentric diffraction pattern, the center and radius of rings are fundamental for further statistics and analysis. Therefore, center calibration and peak grouping are rather important.

During the image rotation and combination algorithm, some initial guess of center is set in advance. However, due to the configuration of the three detectors, the real center is the triple intersection of detectors. Therefore, further calibration is necessary and the good initial guess of center position is selected as triple intersection point.

The logic of the radius calibration is pretty straightforward. Calculating the distances between center and all peak centroids is the first step, followed by comparison of these values with the standard diffraction ring radius generated by the Mg lattice parameters. The minimum difference between two diffraction rings is larger than 20 pixels and therefore the threshold of 10 pixels is quite reasonable in radius-distance comparison. Finally, an approximated structure parameter categorized by reflection orientation is produced.

These orientation-wise data are selected to be input into the circle center calibration. This problem could be stated in the following form: fitting the center of a circle by multiple points along the arc. It is an overdetermined least square fitting problem. There are many algorithms reviewed by Umbach [46]. The general idea of fitting will be introduced here.

A regular formulation of a circle is $(x-a)^2+(y-b)^2=r^2$ and the dataset is composed of points $(x_1,y_1),(x_2,y_2)\cdots,(x_n,y_n)$. The reasonable measure of fit process is given by the summation of distances between the circle and data points, which is formulated by:

$$SS(a,b,r)=\sum_{i=1}^{n}\left(r-\sqrt{(x-a)^2+(y-b)^2}\right)^2 \tag{2.7}$$

There is special notation used in the following derivation.

$$\begin{aligned} X_{ij} &= x_i - x_j \\ \bar{X}_{ijk} &= X_{ij}X_{jk}X_{ki} \\ X_{ij}^{(2)} &= x_i^2 - x_j^2 \end{aligned} \tag{2.8}$$

The method of modified least square methods is introduced in the ring fitting algorithm. This algorithm reduces the importance of pairs close to each other and the measure is SSM rather than SS.

$$SSM\left(a,b\right)=\sum_{i=1}^{n-1}\sum_{j=i+1}^{n}\left(aX_{ji}+bYji-0.5\left(X_{ij}^{(2)}+Y_{ij}^{(2)}\right)\right)^{2} \tag{2.9}$$

Then the differentiation with respect to a and b yields the system:

$$\begin{aligned}\frac{\partial SSM}{\partial a}=&2b\sum_{i=1}^{n-1}\sum_{j=i+1}^{n}X_{ji}Y_{ji}-\sum_{i=1}^{n-1}\sum_{j=i+1}^{n}X_{ji}Y_{ji}^{(2)}\\&+2a\sum_{i=1}^{n-1}\sum_{j=i+1}^{n}X_{ji}^{2}-\sum_{i=1}^{n-1}\sum_{j=i+1}^{n}X_{ji}X_{ji}^{(2)}\end{aligned} \tag{2.10}$$

$$\begin{aligned}\frac{\partial SSM}{\partial b}=&2a\sum_{i=1}^{n-1}\sum_{j=i+1}^{n}Y_{ji}X_{ji}-\sum_{i=1}^{n-1}\sum_{j=i+1}^{n}Y_{ji}X_{ji}^{(2)}\\&+2b\sum_{i=1}^{n-1}\sum_{j=i+1}^{n}Y_{ji}^{2}-\sum_{i=1}^{n-1}\sum_{j=i+1}^{n}Y_{ji}Y_{ji}^{(2)}\end{aligned} \tag{2.11}$$

Then the coordinate of center a and b can be calculated by the following formula:

$$\begin{aligned}a_{M}&=\frac{DC-BE}{AC-B^{2}}\\b_{M}&=\frac{AE-BD}{AC-B^{2}}\end{aligned} \tag{2.12}$$

The constants A,B,C,D,E value is given in the appendix A.

2.2.6 Overall Ellipse Fitting of Diffraction Ring

After addition of load on specimen, the concentric circles gradually distorts into ellipses due to the Poisson effect. According to the Bragg's law, the larger d between planes, the smaller the diffraction angle as well as the radius of the peak. However, this ring deformation only reflects the overall response rather than individual peak movements.

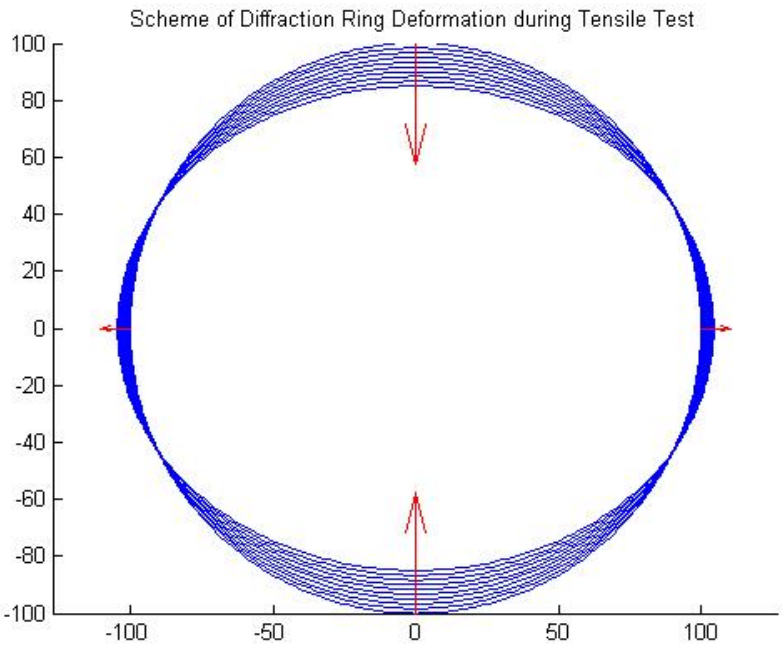

Figure 2.19: Deformation of Diffraction Ring during Tensile Test

Two different fitting algorithms are applied in the analysis for reference – Direct Ellipse Fitting and Least Square Ellipse Fitting. They will be presented in the following part.

2.2.6.1 Ellipse Fit Using Least Squares Criterion

The least square fitting follows the same principle as the circle fitting – the measure of fit is the sum of distance between data points to the target ellipse. The objective of the ellipse fit is to minimize the sum of the algebraic distances (cost) between the measurement and the fitted curve. The mathematical representation of conic equation of the ellipse is $ax^2 + bxy + cy^2 + dx + ey + f = 0$. The estimator is extracted from the following equations $g(x, y; \mathbf{A}) = ax^2 + bxy + cy^2 + dx + ey = f$, where (x_i, y_i) is a pair of collected data and $\mathbf{A}$ is the parameters (a, b, c, d, e) to be fit. Then the cost function is defined as:

$$\begin{aligned} C(\mathbf{A}) =& (\mathbf{g}(\mathbf{x}, \mathbf{y}; \mathbf{A}) - \mathbf{f})^T (\mathbf{g}(\mathbf{x}, \mathbf{y}; \mathbf{A}) - \mathbf{f}) \\ =& (\mathbf{XA} + \mathbf{f})^T (\mathbf{XA} + \mathbf{f}) \\ =& \mathbf{A}^T \mathbf{X}^T \mathbf{XA} + 2\mathbf{f}^T \mathbf{XA} + N\mathbf{f}^2 \end{aligned} \tag{2.13}$$

$\mathbf{g}(\mathbf{x}, \mathbf{y}; \mathbf{A})$: vector function of all the measurements and each element of $\mathbf{g}$ is $g(x, y; \mathbf{A})$
$\mathbf{X}$: a matrix whose element is composed of row vector (Design Matrix) $(x_i^2, x_i y_i, y_i^2, x_i, y_i)$
N : the number of total measurements $\mathbf{f}$: defined as constant column vector sharing one value f

The next step is to differentiate the cost function with respect to $\mathbf{X}$ and equate the result to zeros, which yields:

$$SS(\mathbf{X}) = -f \frac{\sum_{i=1}^{N} \mathbf{X}(x_i^2, x_i y_i, y_i^2, x_i, y_i)}{\mathbf{X}^T \mathbf{X}} \tag{2.14}$$

The non-tilt form of the ellipse is $\frac{(x-x_0)^2}{a_0^2} + \frac{(y-y_0)^2}{b_0^2} = 1$ or $Ax^2 + Cy^2 + Dx + Ey + F = 0$ and the transformation between two different forms could be completed by the following relationship:

$$\begin{aligned} F' &= -F + \frac{D^2}{4A} + \frac{D^2}{4A} \\ x_0 &= -\frac{D}{2A} \\ y_0 &= -\frac{E}{2C} \\ a_0 &= \sqrt{|\frac{F'}{A}|} \\ b_0 &= \sqrt{|\frac{F'}{C}|} \end{aligned} \tag{2.15}$$

The formula above is the main idea of the least square fitting of ellipse and the detailed formula is added in the appendix C.

2.2.6.2 Direct Ellipse-Specific Fitting

The formulation of the conic curve is the same as of the previous method but more constraint is imposed in this fit. If a conic formula represents ellipse, then the discriminant should

obey $b^2 - 4ac < 0$ and due to difficulty of imposing inequality as constraint, the formula was transformed into $4ac - b^2 = 1$ because all the parameters could be scaled at the same time. In the matrix form, rewrite the scalar equation into matrix form $\mathbf{A}^T\mathbf{C}\mathbf{A} = 1$:

$$\mathbf{A}^T \begin{bmatrix} 0 & 0 & 2 & 0 & 0 & 0 \\ 0 & -1 & 0 & 0 & 0 & 0 \\ 2 & 0 & 0 & 0 & 0 & 0 \\ 0 & 0 & 0 & 0 & 0 & 0 \\ 0 & 0 & 0 & 0 & 0 & 0 \\ 0 & 0 & 0 & 0 & 0 & 0 \end{bmatrix} \mathbf{A} = 1 \tag{2.16}$$

$\mathbf{C}$ is the matrix that expresses the constraint. Bookstein [47] showed that if a quadratic constraint is set on the parameters, the minimization becomes deficient generalized eigenvalue systems:

$$\mathbf{X}^T\mathbf{X}\mathbf{A} = \lambda\mathbf{C}\mathbf{A} \tag{2.17}$$

Then the simultaneous equations are got:

$$\begin{aligned} 2\mathbf{X}^T\mathbf{X}\mathbf{A} - 2\lambda\mathbf{C}\mathbf{A} &= 0 \\ \mathbf{A}^T\mathbf{C}\mathbf{A} &= 1 \end{aligned} \tag{2.18}$$

After rewriting the Scatter Matrix $\mathbf{S} = \mathbf{X}^T\mathbf{X}$, the system changes into:

$$\begin{aligned} \mathbf{S}\mathbf{A} &= \lambda\mathbf{C}\mathbf{A} \\ \mathbf{A}^T\mathbf{C}\mathbf{A} &= 1 \end{aligned} \tag{2.19}$$

The eigenvalue-eigenvector pair $(\lambda_i, \mathbf{u}_i)$ from matrix $\mathbf{S}$ could also be the solution of this system. So is $(\lambda_i, \mu_i\mathbf{u}_i)$. The value of μ_i is given by:

$$\mu_i = \sqrt{\frac{1}{\mathbf{u}_i^T\mathbf{S}\mathbf{u}_i}} \tag{2.20}$$

Finally, we set $\hat{A}_i = \mu_i \mathbf{u}_i$ to solve the problem (2.18). In order to satisfy the constraint, there should be an only negative eigenvalue $\lambda_i < 0$ which yields the only result, and all the other $\lambda_i > 0$ would be ignored. The pseudo code is given as here [48]:

```
function A = DirectFit(x,y)
%Build the Design Matrix: X
X=[x.*x, x.*y, y.*y, x, y, ones(size(x))];
%Build scatter matrix: S
S= X'*X;
% Build Constraint Matrix: C
C=zeros(6,6);
C(1,3)=-2;
C(3,1)=-2;
C(2,2)=1;
%Solve the eigen problem
[evec,eval] = eig(S,C);
%find the only negative eigenvalue
[NegR,NegC]=find(geval<0 & ¬isinf(geval));
%Get Fitted Parameters
A= gevec(:,NegC);
end
```

2.3 Results and Discussion

2.3.1 Baseline for Peak Movement Analysis

In order to show the stability of beam, a baseline of peak movement is provided as reference. As shown in Figure 2.20a, a horizontal peak is selected ($\eta = 90^o$). The reflection of the peak is $\langle 100 \rangle$. The radial displacement plot visualizes a smooth movement within 0.02 pixel without abrupt value change, which coincides with the trajectory plot.

Figure 2.21 compares the baseline peak ($\eta = 90^o$) with another $\langle 100 \rangle$ peak ($\eta = 0^o$).

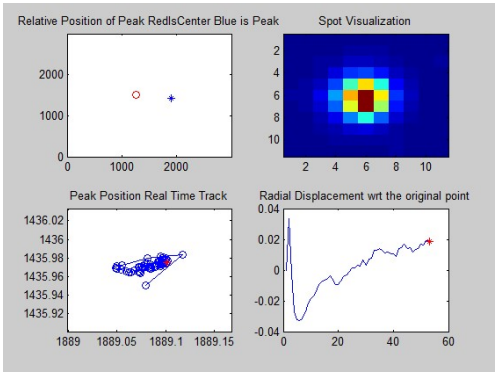

(a) Baseline Movement

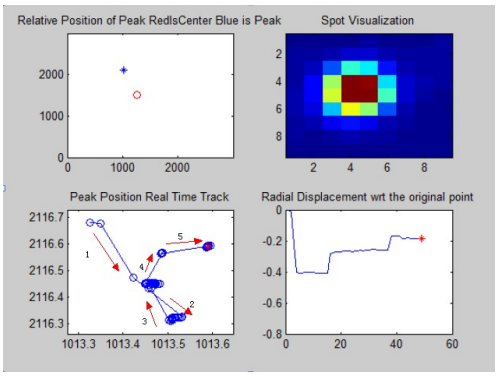

(b) A Sample Peak

Figure 2.20: Baseline of Peak Movement: Upper left corner shows the peak location; Upper right plot contours the intensity; Lower left corner visualizes the trajectory of peak intensity and Lower right diagram shows the radial displacement time series.

In contrast to relative small movement of the baseline, the blue time series looks full of dynamics. After five-frame loading, step-wise relaxation is clear, which indicates the rich kinetics of dislocation motion. Caceres et al. [49] mentioned that this phenomenon may results from the dynamic interaction of solute atom with dislocations temporarily arrested at forest dislocations. Alternatively, some non-diffusional theory [50] also rationalizes this phenomenon, which is that prismatic slip releases stress concentration lying in dislocation pile-up on basal slip system and new glissile dislocations on basal planes need to break a forest of dislocations on prismatic planes for further glide.

2.3.2 Peak Movement Dynamic Analysis

The peaks of interest are those with azimuthal angle within +/- 5 degrees of the vertical axis, because the diffraction vectors of these peaks were parallel to tensile axis and the radial displacement of these peaks contained tensile strain information. Four load steps were tested and four reflections of interest analyzed: $\langle 100 \rangle$, $\langle 101 \rangle$, $\langle 200 \rangle$ and $\langle 202 \rangle$. Actually, $\langle 200 \rangle$ peaks were the higher order $\langle 100 \rangle$ peaks and showed relatively larger displacements and the relaxation phenomenon was easier to be captured. The $\langle 100 \rangle$ and $\langle 200 \rangle$ were prismatic planes and $\langle 101 \rangle$ and $\langle 202 \rangle$ were pyramidal planes.

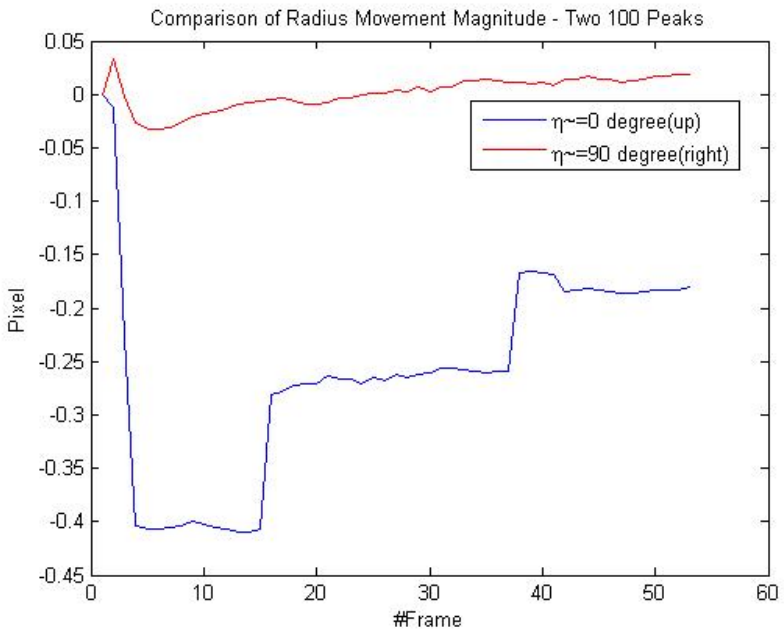

Figure 2.21: Comparison of Baseline Peak and a Typical Peak

Vertical peaks were expected to move inwards due to the increase of lattice strain and the horizontal peaks were likely to move outwards due to the Poisson Effect. The whole process should be divided into two parts – the loading part and the relaxation part. The peak radial movement directions in two processes were likely to be opposite to each other. However, after the examination of many points, the results looked diverse. In the following parts, typical peaks movement patterns will be presented and statistics of peak motion will be developed.

2.3.2.1 Typical Peak Trajectory Classification

Several factors are important in the peak dynamic study. The net radial displacement magnitude and direction are the best indicator of lattice strain. The movement pattern provides insight into the kinetics of deformation mechanisms. In the following analysis, the results are presented in separate four-block figures. The upper-left corner introduces peak relative position to the center of frame. The upper-right corner shows the peak intensity distribution. The lower-left subfigure gives the recorded peak trajectory in the detector space and the lower-right one contains two plots of the peak radial displacement with respect to

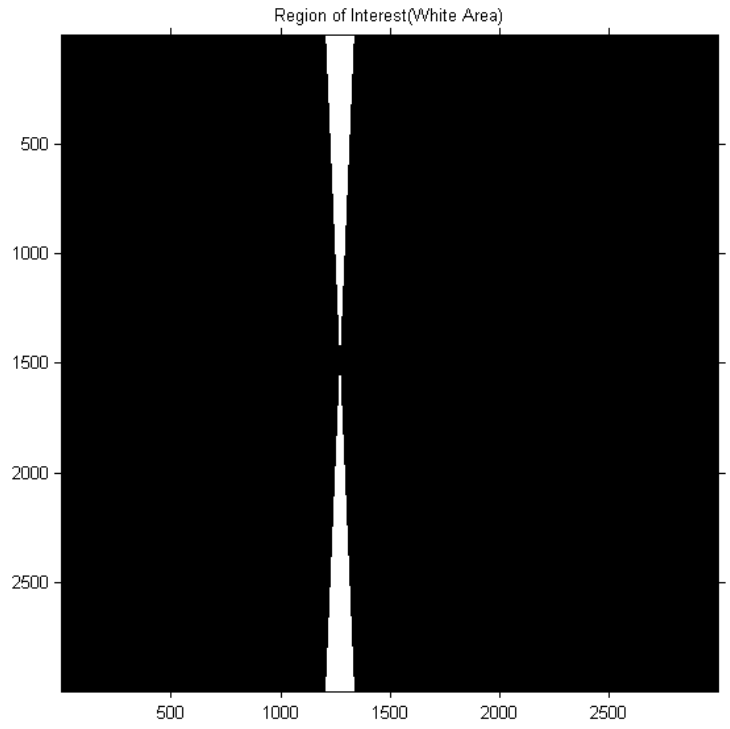

Figure 2.22: Scheme of Region of Interest (White Area)

time.

Obvious Loading without Relaxation Some peaks moved inwards after load addition but showed oscillations along azimuthal direction without net outwards displacement. The red arrows showed the direction of movement and this trajectory indicated that even in the relative plastic region, some peaks indicated little radial motion as bulk stress decreased.

Gradual Loading without Relaxation In Figure 2.24, this class of peaks reacted tardily to the load addition. For most of the trajectories, the loading duration took roughly five frames, but a gradual-loading peak might take 50 frames to develop. The peak kept moving inwards with decreasing speed and the final vibration magnitude was within 0.1 pixel.

Gradual Loading with Relaxation In Figure 2.25, this category was almost the same as the previous one except that obvious relaxation was observed at the last stage of trajectory. Clear radial inwards displacement was found at about frame 85, when the peak sharply

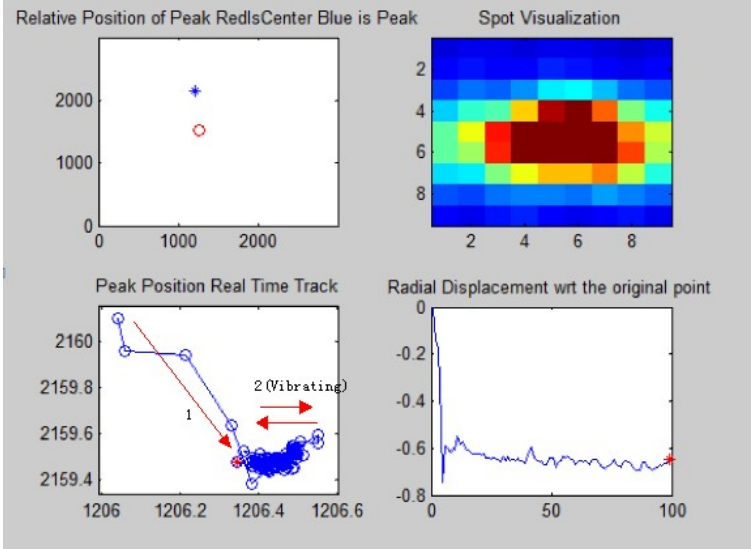

Figure 2.23: Lower order prismatic $\langle 100 \rangle$ peak trajectory I: at lower right corner, oscillations along azimuthal direction following straightforward outwards movement but no obvious relaxation ($142MPa \rightarrow 168MPa \rightarrow 149MPa$)

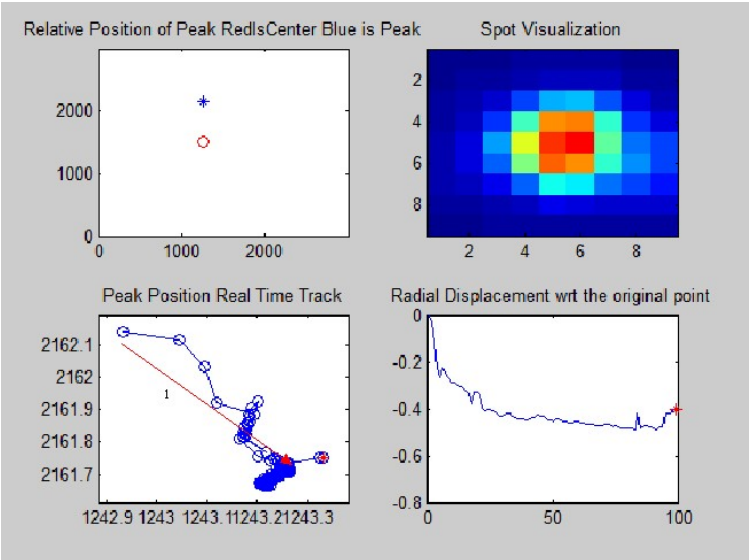

Figure 2.24: Lower order prismatic $\langle 100 \rangle$ peak trajectory II: in lower right plot, time series keep going inwards without relaxation; at lower left corner, the centroid deaccelerates unidirectionally ($120MPa \rightarrow 153MPa \rightarrow 142MPa$)

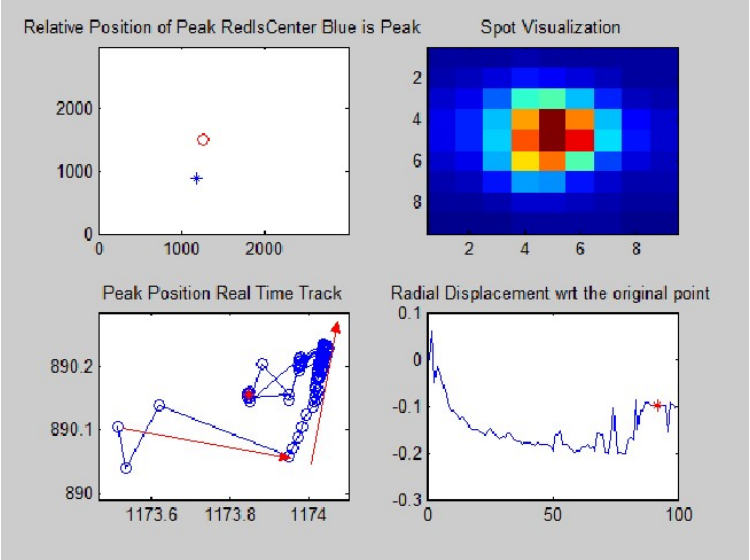

Figure 2.25: Lower order prismatic $\langle 100 \rangle$ peak trajectory III: at lower right corner, the time series looks a convex parabola and obvious division between loading and relaxation is observed; at lower left corner, relaxation is clear at the last stage of trajectory $(120MPa \rightarrow 153MPa \rightarrow 142MPa)$

turned along the trajectory.

Loading Followed by Stepwise Relaxation The peak moved inwards in smooth manner but moved outwards in jerky manner. If the whole process of movement was traced, then discrete bursts were captured. From Figure 2.26, the radial displacement relaxation appears as a terrace composed of three steps, which are associated with the point clusters between arrow 2 and 3, arrow 3 and 4 and near the end point of arrow 5.

Movement in Opposite Direction Peaks of this category were all pyramidal ones and the net displacement of the movement was positive under tensile loading, which inferred that the distances between planes decreased. In this category, three sub-categories could be further classified:

(a) **Uni-direction Movement:**

This sub-category described the pattern wherein the peak kept moving outwards and never turned back. The whole process is illustrated in Figure 2.27.

(b) **Fluctuating Movement:**

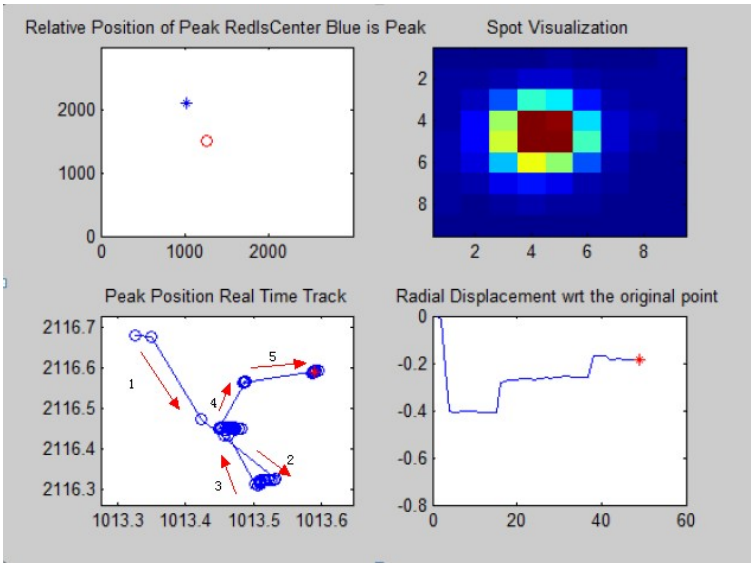

Figure 2.26: Lower order prismatic ⟨100⟩ peak trajectory IV: at lower right corner, the peak moved inwards in smooth manner but jerkily moved outwards; hopping trajectory and red arrows concord with sudden drops between terraces in time series $(110MPa \rightarrow 118MPa \rightarrow 115MPa)$

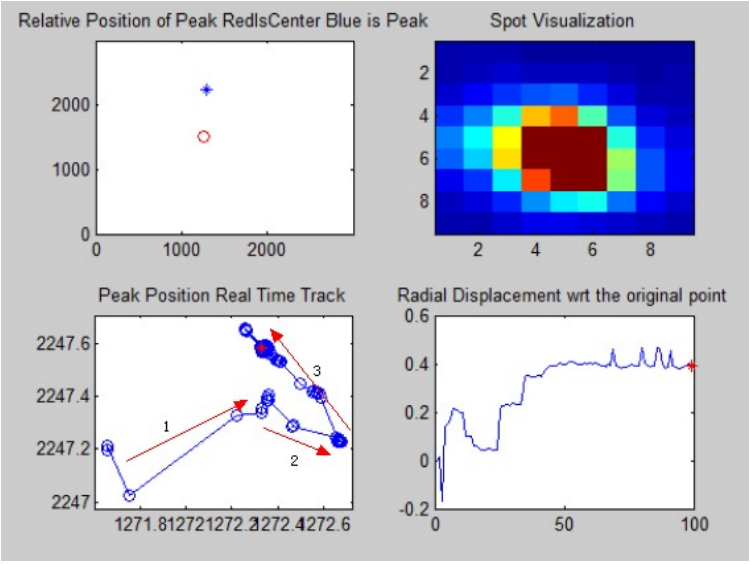

Figure 2.27: Lower order pyramidal ⟨101⟩ peak trajectory I: at lower left corner, trajectory shows initial grain rotation (goes sideways) and subsequent anti-strain-tendency outwards movement $(142MPa \rightarrow 168MPa \rightarrow 149MPa)$

Motion of peaks sometimes went drastically inwards and outwards in jerky manner and no simple pattern could be concluded. Turning to Figure 2.28, the peak moved

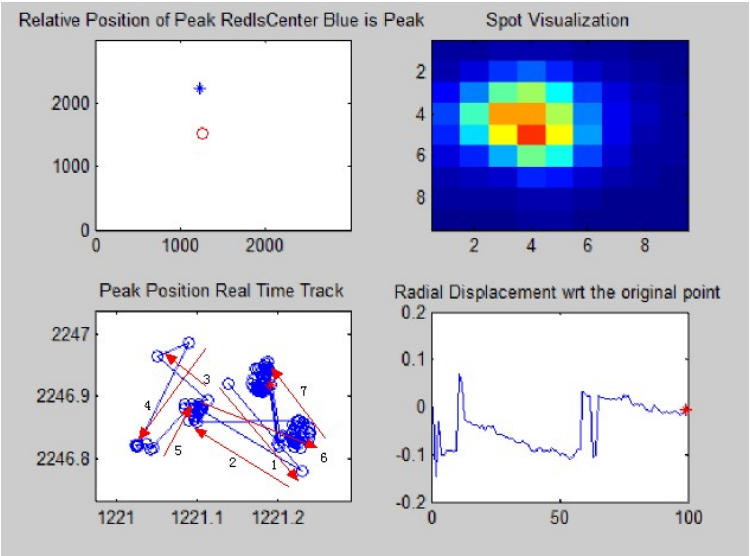

Figure 2.28: Lower order pyramidal $\langle 101 \rangle$ peak trajectory II: at lower left corner, centroid bounces without clear direction; at lower right corner, time series is composed of 0.2-pixel strain fluctuation ($120MPa \rightarrow 153MPa \rightarrow 142MPa$)

almost randomly about the initial location. Two negative-to-positive displacement jumps were observed at frame 10 and 60, which implied that sudden deformation and/or reorientation.

(c) **Reverse Relaxation:**

The name "reverse relaxation" means the totally opposite trajectory to the predicted one, which moved outwards first then relaxed inwards. Figure 2.29 showed the opposite moving direction of Figure 2.25.

Vibration Some peaks moved without clear direction and randomly wandered about the original point like Brownian movement. The trajectory is shown as follows: In this case, the net displacement was close to zero and no clear direction was apparent. However, the magnitude of vibration was about 0.2 pixel.

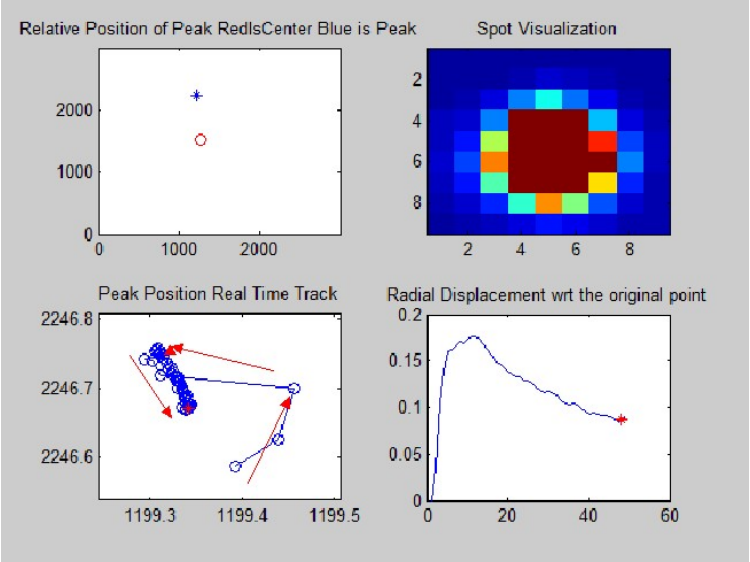

Figure 2.29: Lower order pyramidal $\langle 101 \rangle$ peak trajectory III: at lower left corner, trajectory indicates a two-stage movement composed of go-and-turn loading and gradual backwards movement, which is almost mirror to the one in Figure 2.25 $(110MPa \rightarrow 118MPa \rightarrow 115MPa)$

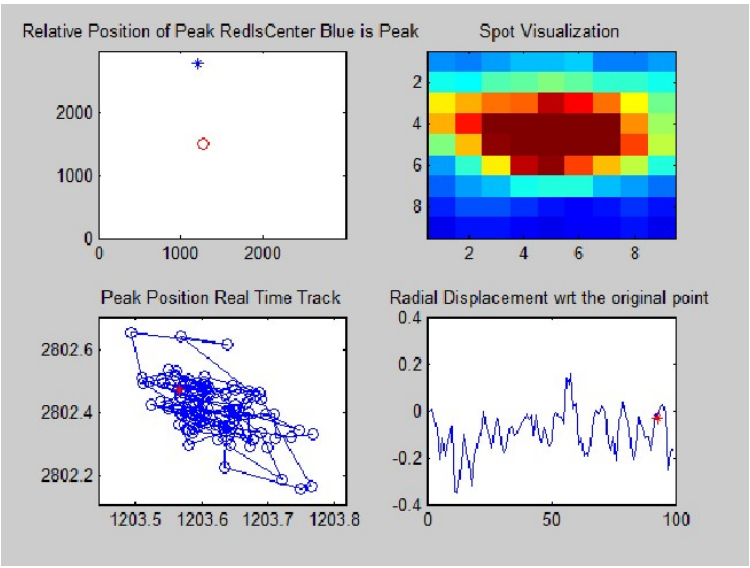

Figure 2.30: Higher order prismatic $\langle 200 \rangle$ peak trajectory I: at lower right corner, noisy time-series is shown and zero net displacement is observed, where centroid swings diagonally $(142MPa \rightarrow 168MPa \rightarrow 149MPa)$

2.3.2.2 Important Features of Observed Trajectories

The classification of peak trajectories in the previous section is still not conclusive and further complementary experiments are needed for validation. However, some features in the trajectories are illustrative for study of deformation mechanism.

Initial Tangential Displacement At the first few frames, the peaks moved tangentially besides radially and it was almost common for all trajectories. The tangential component indicated the azimuthal angle change, which inferred the effect of lattice rotation. This could be due to rotation of specimen or, more likely a different part of the grain meeting the Bragg condition.

Jerky Sudden Jumps in both the radial displacement plot and detector space trajectory indicated the swift transformation of lattice structure from one state into the other. The jerky manner differs case by case. For example Figure 2.26, the peak jumped step by step in the detector and between stable locations, the peak kept almost stationary between jumps. By contrast, Figure 2.24 demonstrates a totally different manner–the peak keeps jogging (moving along one direction slowly) or jumping (changed location suddenly swiftly) in the detector. The similarity of two patterns were sudden change of peak radial location. This discontinuous movement pattern hints at a jerky manner of the deformation, such as solute strengthening of dislocation.

Vibration The vibrancy of peaks was diverse and even on the same reflection ring, (see Figure 2.31) some peaks were stable (almost stationary in the detector) but the others were active (vibrating in large magnitude).

High degrees of dislocation movement inside the peak-related grain may explain the fluctuation of radial displacement. However, Figure 2.31b vibrated at a point different from the original point while Figure 2.30 showed vibrated at the very beginning. This difference may infer different deformation manners.

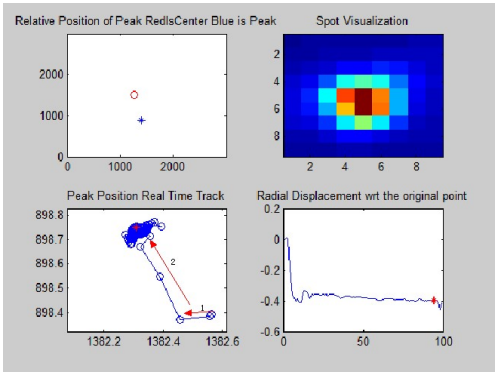

(a) Stable Trajectory ($\langle 100 \rangle$, $135MPa \rightarrow 127MPa$)

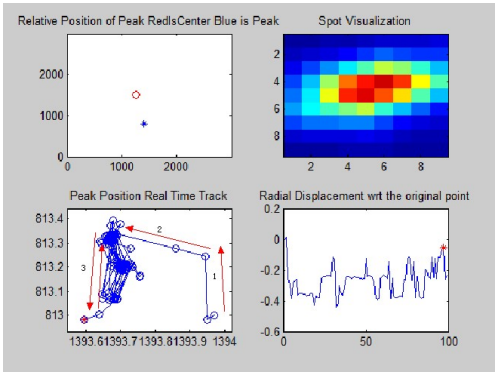

(b) Vibrating Trajectory ($\langle 101 \rangle$, $135MPa \rightarrow 127MPa$)

Figure 2.31: Comparison of Vibrancy of Two Peaks: subplot **a** shows stationary trajectory while subplot **b** shows movement with high vibrancy

Jogging Jogging means the peak keeps slow moving uni-directionally in the detector. This phenomenon was shown during loading and appeared together with other movement. In Figure 2.25, the right arrow indicated very typical jogging process – going towards one direction in decelerating manner which was reflected by the decreasing slope in the displacement curve. Here are many examples of jogging (see Figure 2.32 and 2.33)

In the Figure 2.32, pattern I jogged at stage 2 and then turned to jump-and-stop mode. Under the same loading, pattern II jogged at the whole process. The jogging also happened at higher and lower loading. Stage 2 of pattern III and stage 4 of pattern IV showed a period of jogging movement (See Figure 2.33).

Tardy Response to Loading In the pattern classification, gradual loading describes no quick response (about 5 frames) to external loading addition. Micro-structurally speaking, this might due to high resistance of deformation of some grains at the beginning of loading. This movement existed in both loading-relaxation peaks or reverse relaxation ones. In Figure 2.24 and 2.23, there was no obvious division point between loading and relaxation stage. Figure 2.34 demonstrated an obvious lag at the start of pyramidal plane distance shrinkage.

Delayed movement of peaks could be explained in statistics viewpoint, which meant due to

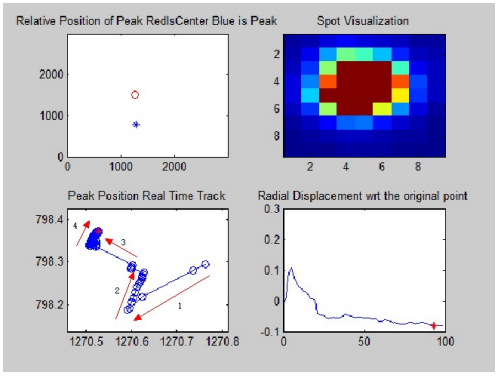

(a) Jogging I($\langle 101 \rangle$,$135MPa \rightarrow 127MPa$)

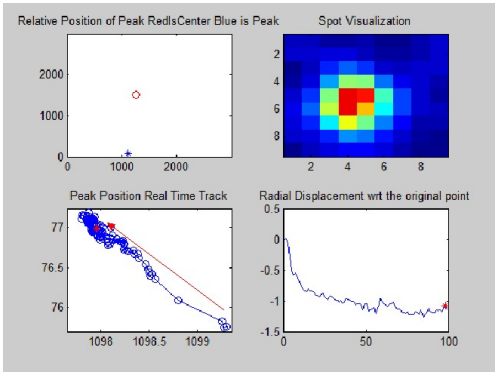

(b) Jogging II($\langle 202 \rangle$,$135MPa \rightarrow 127MPa$)

Figure 2.32: Jogging Movement Pattern Example I: subplot **a** (pattern I) shows jump-and-stop pattern while subplot **b** (pattern II) gives an example of uni-directional trajectory

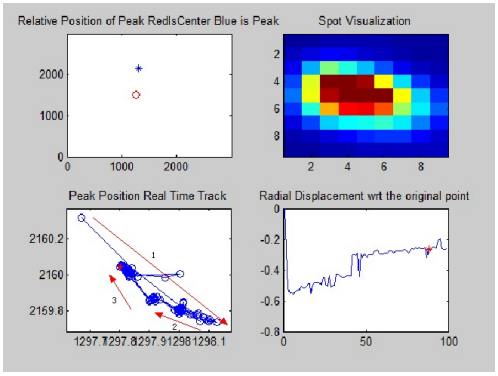

(a) Jogging III($\langle 100 \rangle$,$153MPa \rightarrow 142MPa$)

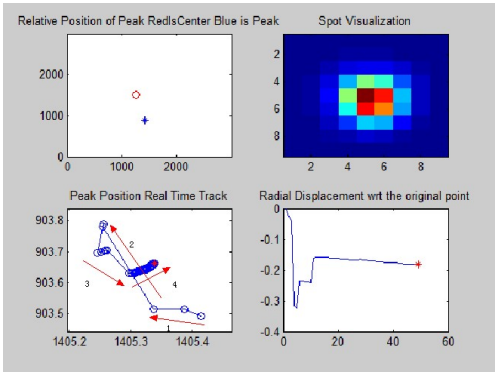

(b) Jogging IV($\langle 100 \rangle$,$118MPa \rightarrow 115MPa$)

Figure 2.33: Jogging Movement Pattern Example II: subplot **a** (pattern III) shows jogging in higher load and subplot **b** (pattern IV) show the one in lower load

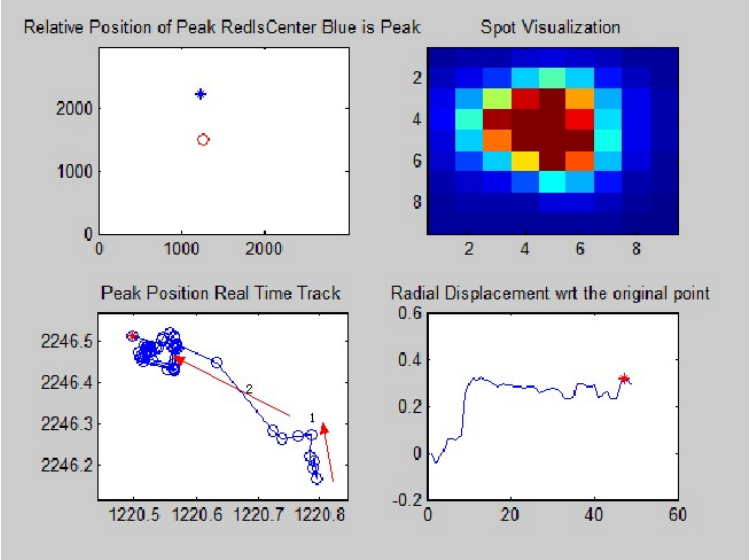

Figure 2.34: Reverse Relaxation with Tardy Response ($\langle 101 \rangle$, $153MPa \rightarrow 142MPa$)

anisotropy of grains, some grain deformed first at the cost of suppression of others. However, the average material response is well consistent with the stress-strain curve, which will be further discussed in the ellipse fitting analysis.

2.3.2.3 Statistics of Peak Movement Dynamics

Hundreds of stable peaks were traced and statistics of net displacements for separate reflections were achieved. The definition of column name will be clarified first. X Coor and Y Coor locate the position of centroid in the detector. Scan means one out of four scan numbers–606, 609, 616 and 622. Net Disp means the centroid radial position change for the entire history (between the 1st frame and the last frame). Direction means towards the center of the detector or not. Position clarifies the peak location qualitatively–in the upper or lower half of the detector. In the following part, the result will be presented reflection-wise:

Lower Order Prismatic Peaks $\langle 100 \rangle$

The average radial displacement was 0.3 pixel and the standard deviation was 0.14 pixel. The peaks of interest is listed:

Higher Order Prismatic Peaks $\langle 200 \rangle$

The average radial displacement was 0.5 pixel and the standard deviation was 0.27

Table 2.1: Displacement Statistics of ⟨100⟩ Peaks

X Coor	Y Coor	Scan	Net Disp	Direction	Index	Position
1184	2115	616	0.14	Inwards	100	Lower
1308	845	616	0.6	Inwards	100	Upper
1086	868	616	0.3	Inwards	100	Upper
1290	2119	616	0.3	Inwards	100	Lower
1300	843	606	0.4	Inwards	100	Upper
1024	889	606	0.225	Inwards	100	Upper
1415	2101	606	0.125	Inwards	100	Lower
1270	844	606	0.125	Inwards	100	Upper
1383	2109	606	0.17	Inwards	100	Lower
1171	850	622	0.3	Inwards	100	Upper
1216	845	622	0.5	Inwards	100	Upper
1392	2106	622	0.35	Inwards	100	Lower
1307	845	609	0.33	Inwards	100	Upper
1243	843	609	0.3	Inwards	100	Upper

pixel. The peaks of interest is listed in Table 2.2.

Lower Order Pyramidal Peaks ⟨101⟩

For pyramidal peaks, statistics of movements towards two different directions were done separately. For inwards movement, the average displacement was 0.15 pixel and the standard deviation was 0.079 pixel, which is listed in Table 2.3. For outwards movement, the average displacement was 0.3 pixel with standard deviation of 0.2 pixel, which is tabulated by Table 2.4.

Lower Order Pyramidal Peaks ⟨202⟩

For inwards movement, the average displacement was 0.84 pixel and the standard deviation was 0.53 pixel, which is listed in Table 2.5. For outwards movement, the average displacement was 0.5 pixel with standard deviation of 0.27 pixel, which is tabulated by Table 2.6.

More details about peak trajectories are included in the Appendix D.

Table 2.2: Displacement Statistics of $\langle 200 \rangle$ Peaks

X Coor	Y Coor	Scan	Net Disp	Direction	Index	Position
1383	2109	616	0.31	Inwards	200	Lower
1253	843	616	0.45	Inwards	200	Upper
955	312	606	0.2	Inwards	200	Upper
1575	2649	606	0.38	Inwards	200	Lower
1320	203	622	0.7	Inwards	200	Upper
1214	203	622	0.3	Inwards	200	Upper
1282	201	622	0.8	Inwards	200	Upper
1179	2762	622	0.4	Inwards	200	Lower
1137	2756	622	1	Inwards	200	Lower
1220	201	609	0.74	Inwards	200	Upper
1200	2761	609	0.001	Inwards	200	Lower
1184	2761	609	0.22	Inwards	200	Lower

Table 2.3: Inwards Displacement Statistics of $\langle 101 \rangle$ Peaks

X Coor	Y Coor	Scan	Net Disp	Direction	Index	Position
1215	2205	616	0.3	Inwards	101	Lower
1232	759	616	0.1	Inwards	101	Upper
1363	765	606	0.16	Inwards	101	Upper
1464	2178	606	0.15	Inwards	101	Lower
1404	2192	622	0.2	Inwards	101	Lower
1281	2207	609	0.05	Inwards	101	Lower
1215	2204	609	0.15	Inwards	101	Lower

Table 2.4: Outwards Displacement Statistics of $\langle 101 \rangle$ Peaks

X Coor	Y Coor	Scan	Net Disp	Direction	Index	Position
1281	2206	616	0.125	Outwards	101	Lower
1195	761	616	0.15	Outwards	101	Upper
1231	759	606	0.275	Outwards	101	Upper
1209	758	606	0.11	Outwards	101	Upper
1139	2159	606	0.1	Outwards	101	Lower
1340	2202	606	0.04	Outwards	101	Lower
1282	757	622	0.2	Outwards	101	Upper
1212	759	622	0.4	Outwards	101	Upper
1189	2202	622	0.25	Outwards	101	Lower
1195	761	609	0.5	Outwards	101	Upper
1231	758	609	0.686	Outwards	101	Upper
1241	757	609	0.5	Outwards	101	Upper

Table 2.5: Inwards Displacement Statistics of $\langle 202 \rangle$ Peaks

X Coor	Y Coor	Scan	Net Disp	Direction	Index	Position
1386	33	616	0.15	Inwards	202	Upper
1278	2936	616	0.5	Inwards	202	Lower
1387	32	606	0.55	Inwards	202	Upper
1203	2938	606	0.85	Inwards	202	Lower
1464	2922	622	0.75	Inwards	202	Lower
969	2908	622	2	Inwards	202	Lower
1713	2864	622	1	Inwards	202	Lower
1655	2883	622	0.5	Inwards	202	Lower
1487	45	609	1	Inwards	202	Upper
967	57	609	0.84	Inwards	202	Upper
1333	2934	609	1.5	Inwards	202	Lower
1108	2928	609	1	Inwards	202	Lower
1199	2937	609	1.1	Inwards	202	Lower
1460	2923	609	0.4	Inwards	202	Lower
1665	2881	609	0.5	Inwards	202	Lower
1675	2879	609	0.85	Inwards	202	Lower

Table 2.6: Outwards Displacement Statistics of $\langle 202 \rangle$ Peaks

X Coor	Y Coor	Scan	Net Disp	Direction	Index	Position
1052	42	616	0.35	Outwards	202	Upper
968	57	616	0.4	Outwards	202	Upper
1101	35	606	0.3	Outwards	202	Upper
1398	2931	606	0.35	Outwards	202	Lower
929	2901	622	0.9	Outwards	202	Lower
1004	49	622	0.3	Out then In	202	Upper
968	55	622	0.4	Outwards	202	Upper
776	109	609	0.9	Outwards	202	Upper
1612	2859	609	0.1	Outwards	202	Lower

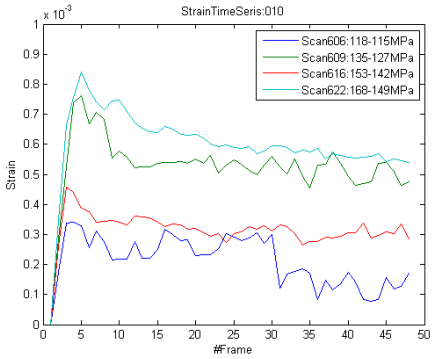

(a) ⟨010⟩ Strain Change Under Different Loading

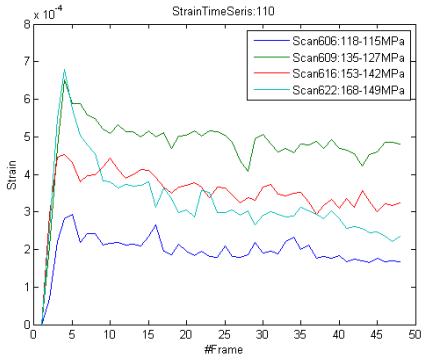

(b) ⟨110⟩ Strain Change Under Different Loading

Figure 2.35: Prismatic Strain Change w.r.t Tensile Load

2.3.3 Ellipse Fitting Analysis

Fitting techniques rendered smooth changes of strain values for all reflections and loadings, which indicated that despite jerky movements of individual peaks, the macroscopic average strains changed gradually if enough grains was taken into consideration. Details of strain computation will be discussed in this section. The quantity $d\epsilon$ (strain change) is studied to emphasize the transient strain-related events after loading. The reflection-wise and load-wise time series would be presented, as well as the effect of threshold and fitting techniques choice. All results in next subsection were computed by least square fitting mentioned in Section 2.2.6.1 (SS shown in Equation 2.14).

2.3.3.1 Reflection-wise Strain Change w.r.t Tensile Loading

Prismatic Planes There were two reflections – ⟨010⟩ and ⟨110⟩ – studied in the ellipse fitting. Due to lack of enough peaks, higher order reflection fitting failed in many cases while the lower order ones showed stable fitting results. In Scan 606, the loading was 118 MPa and the relaxation part was only 3 MPa, which meant the material was still in what would be considered as elastic domain. In Scan 622, the relaxation part was about 18 MPa and the peak load 168 MPa was beyond the yield stress of AZ31. As for $d\epsilon$ curve, Figure 2.35a illustrated that there were no $d\epsilon$ change after reaching the peak value in elastic region (blue line) while in plasticity, obvious decaying would be observed after overshoot (cyan line).

The results of two prismatic reflections were interesting and somehow anti-intuitive. In Figure 2.35a, the red line represented higher load but the green line presented bigger $d\epsilon$ and more relaxation, which might be caused by the unloading and reloading process in loading history (See Figure 2.9). Figure 2.35b the cyan line stabilized at the value lower than green and red lines and inferred that more plasticity was induced in higher loading.

In comparison, the red, green and blue lines had almost identical overshoot peak values and stable relaxed values which meant similarity of two prismatic plane families.

Pyramidal Planes There were three different pyramidal reflections studied in the XRD – $\langle 112 \rangle$, $\langle 011 \rangle$ and $\langle 021 \rangle$. Three planes showed distinct relaxation patterns as follows:

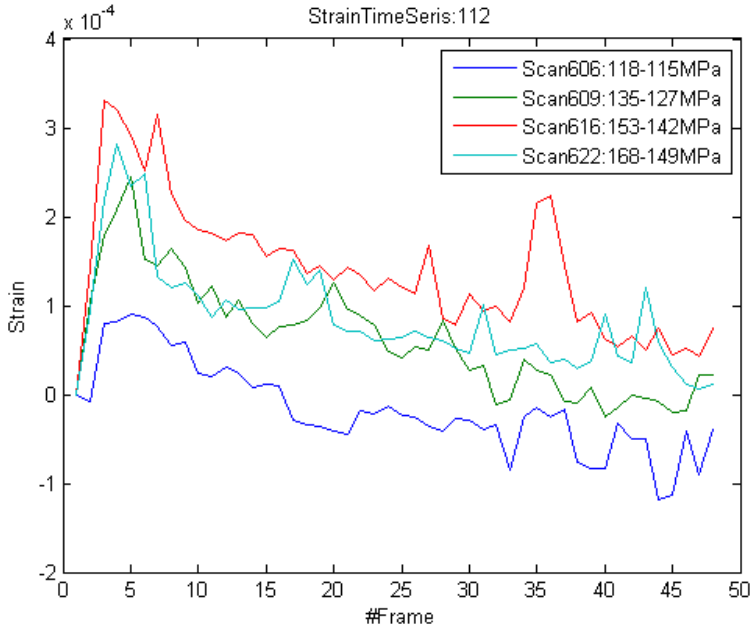

Figure 2.36: $\langle 112 \rangle$ Strain Change Under Different Loading

$\langle 112 \rangle$ planes relaxed in creeping manner in Figure 2.36. In the elastic region, it was loaded and even relaxed into negative $d\epsilon$ region. Compared with prismatic curves, the $d\epsilon$ values were obviously lower and the curves kept going down without stabilization. Moreover, the

relationship between load and $d\epsilon$ was ambiguous in the time series, where green, red and cyan tangled together in the plot.

$\langle 011 \rangle$ planes relaxed in a manner similar to prismatic loading. However, in the lowest

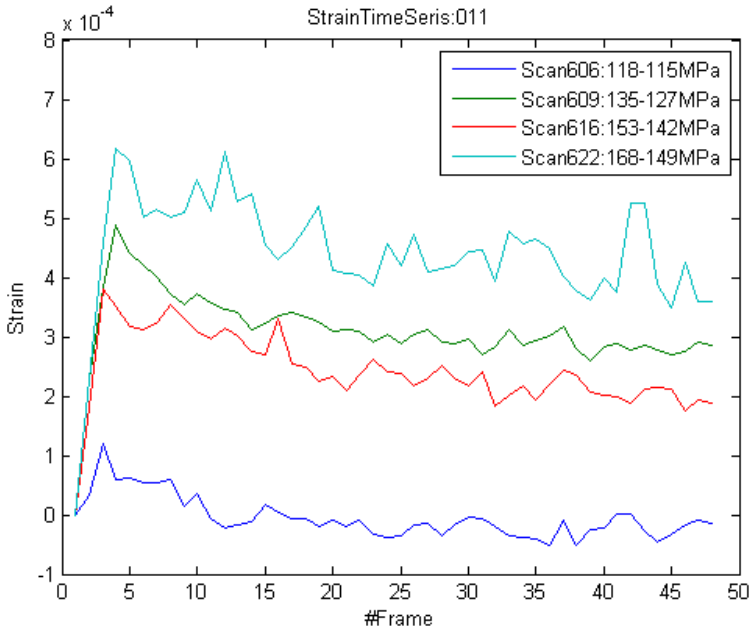

Figure 2.37: $\langle 011 \rangle$ Strain Change Under Different Loading

loading case (see Figure 2.37 blue line), the $d\epsilon$ stablized about 0. Four lines were separate and cyan, green and red lines were approximately parallel to each other.

$\langle 021 \rangle$ planes showed no relaxation in the lowest loading case (see Figure 2.38 blue line) and stabilized after loading. However, in the highest load, the cyan line $d\epsilon$ relaxed to the same value as green line did.

2.3.3.2 Comparison of Strain Changes of Different Reflections

There were two different sets of data discussed here – bi-detector fitting and tri-detector fitting. Two data sets fitted the ellipse with different number of peaks. The bi-detector fitting got rid of the side detector because side peaks correlated to strain component perpendicular to tensile axis and bias might be introduced in the fitting process. However, the bi-detector

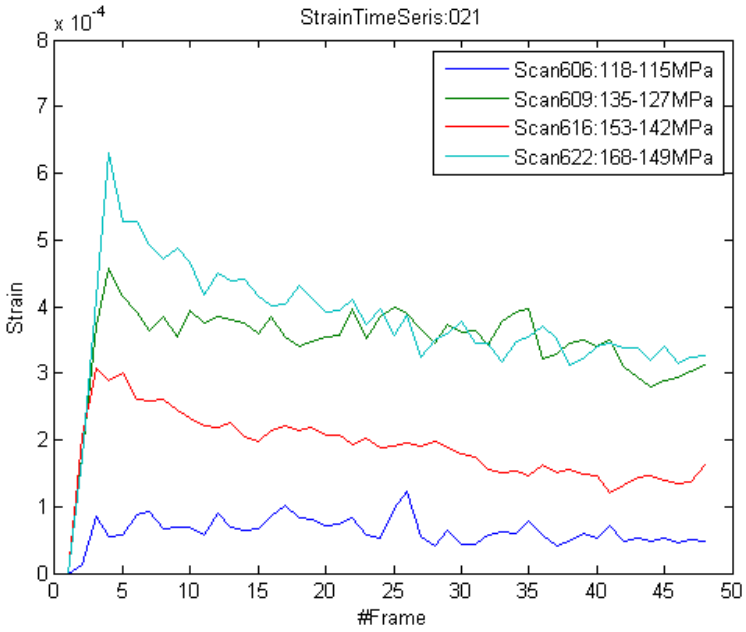

Figure 2.38: ⟨021⟩ Strain Change Under Different Loading

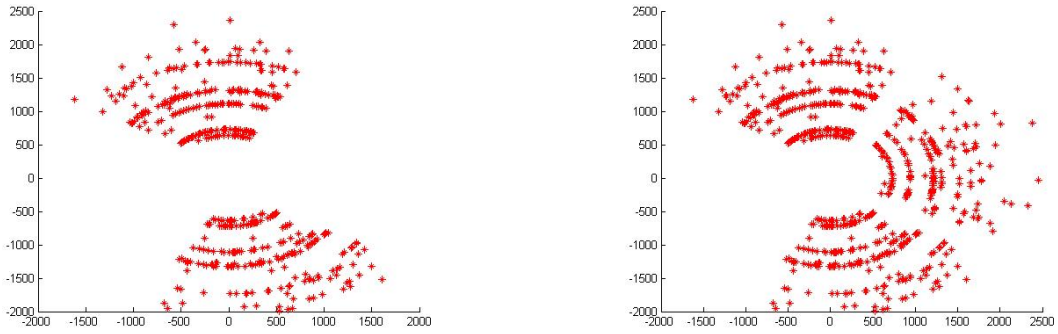

(a) Bi-Detector Peaks of Interest

(b) Tri-Detector Peaks of Interest

Figure 2.39: Peaks of Interest

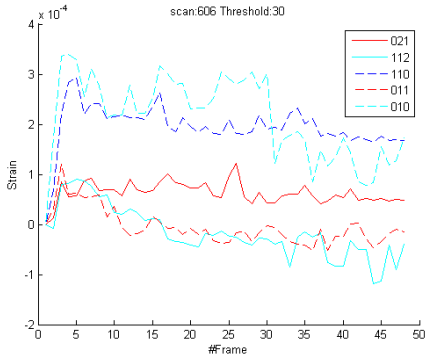

(a) Scan606 Tri-Detector $d\epsilon$ Time Series

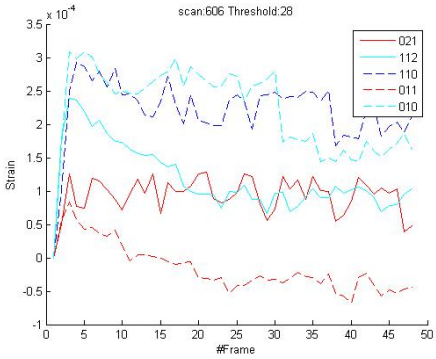

(b) Scan606 Bi-Detector $d\epsilon$ Time Series

Figure 2.40: Scan 606 $d\epsilon$ Time Series

dataset might not be big enough to fit the ellipse parameter and threshold was adjusted to get more peaks in previous algorithm.

Scan606 $(110MPa \rightarrow 118MPa \rightarrow 115MPa)$ In Figure 2.40, all reflections experienced loading-and-relaxation process in elastic region. Obviously, prismatic planes reacted to a larger extent than the pyramidal ones. In both sub-figures, the prismatic planes $d\epsilon$ reached to 3×10^{-4} and then relaxed by 0.7×10^{-4}. As for pyramidal reflections, tri-detector time series gave similar peak value about 1.0×10^{-4} and then diverged into two branches (see Figure 2.40a), one of which ($\langle 112 \rangle$ and $\langle 011 \rangle$) kept decaying and the other ($\langle 021 \rangle$) showed no relaxation. However, $\langle 112 \rangle$ bi-detector time series differed a lot from previous one, which relaxed from 2.4×10^{-4} and stabilized together with $\langle 021 \rangle$ (see Figure 2.40b). Part of fitting results was biased by the dataset selection.

Scan609 $(120MPa \rightarrow 135MPa \rightarrow 127MPa)$ Time series of load 135MPa branched into three different $d\epsilon$ levels in Figure 2.41a. Two prismatic reflections were close to each other. The peak values were 6.5×10^{-4} and relaxed to 5.0×10^{-4}. Pyramidal reflections $\langle 021 \rangle$ and $\langle 011 \rangle$ overlapped in tri-detector series and bifurcated in bi-detector one (red lines). Finally, $\langle 112 \rangle$ pyramidal time series still relaxed to zero $d\epsilon$ as in Figure 2.40. In this case, the behavior of $\langle 011 \rangle$ was affected by the choice of dataset. At Table 2.7 peak $d\epsilon$ meant peak value and relaxed $d\epsilon$ meant the difference between stable and peak values.

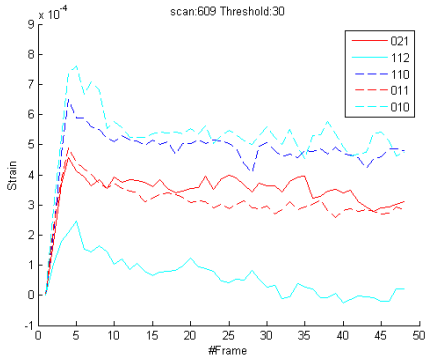

(a) Scan609 Tri-Detector $d\epsilon$ Time Series

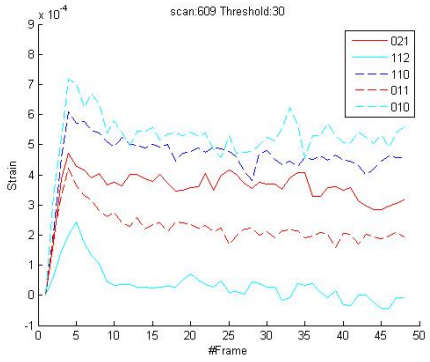

(b) Scan609 Bi-Detector $d\epsilon$ Time Series

Figure 2.41: Scan 609 $d\epsilon$ Time Series

Table 2.7: Figure 2.41a and b Statistics (Unit: 10^{-4})

Reflection	Peak $d\epsilon$	Relaxed $d\epsilon$	Reflection	Peak $d\epsilon$	Relaxed $d\epsilon$
$\langle 010 \rangle$	7.3	2.3	$\langle 010 \rangle$ $\langle 110 \rangle$	6.5	1.0
$\langle 110 \rangle$	6.5	1.5	$\langle 011 \rangle$	4.1	1.1
$\langle 011 \rangle$ $\langle 021 \rangle$	4.5	1.0	$\langle 021 \rangle$	4.5	2.1
$\langle 112 \rangle$	2.5	2.5	$\langle 112 \rangle$	2.5	2.5

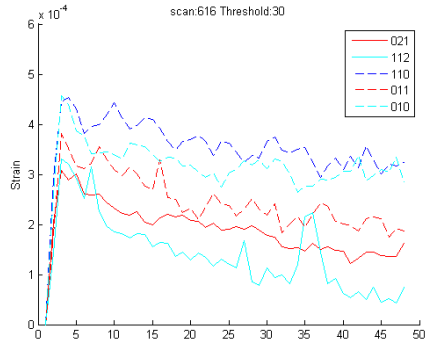

(a) Scan616 Tri-Detector $d\epsilon$ Time Series

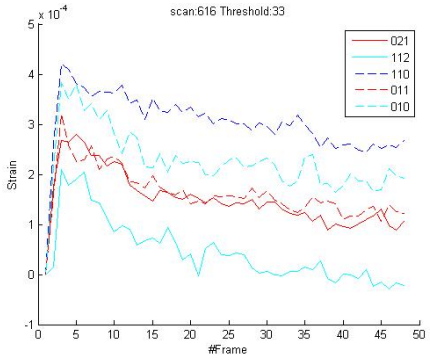

(b) Scan616 Bi-Detector $d\epsilon$ Time Series

Figure 2.42: Scan 616 $d\epsilon$ Time Series

Table 2.8: Figure 2.42a and b Statistics (Unit: 10^{-4})

Reflection	Peak $d\epsilon$	Relaxed $d\epsilon$	Reflection	Peak $d\epsilon$	Relaxed $d\epsilon$
$\langle 010 \rangle$ $\langle 110 \rangle$	4.5	0.7	$\langle 010 \rangle$	3.8	1.5
$\langle 011 \rangle$	3.7	2.0	$\langle 110 \rangle$	4.1	1.1
$\langle 021 \rangle$	3.1	1.3	$\langle 011 \rangle$ $\langle 021 \rangle$	3.0	1.7
$\langle 112 \rangle$	3.2	2.7	$\langle 112 \rangle$	2.1	2.1

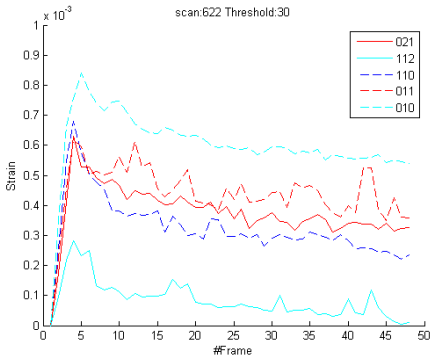

(a) Scan622 Tri-Detector $d\epsilon$ Time Series

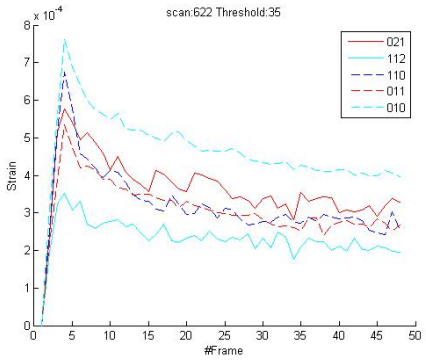

(b) Scan622 Bi-Detector $d\epsilon$ Time Series

Figure 2.43: Scan 622 $d\epsilon$ Time Series

Scan616 $(135MPa \rightarrow 153MPa \rightarrow 142MPa)$ Figure 2.42a and b were similar to each other but the details were different. According to tri-detector plot, all reflections reached close $d\epsilon$ peak values compared with other cases and prismatic series tangled together while the bi-detector series gave sparse peak values and $\langle 011 \rangle$ and $\langle 021 \rangle$ followed almost identical paths. As for $\langle 112 \rangle$, tri-detector series decayed above zero while bi-detector result relaxed until zero. Concluding from Figure 2.42a, pyramidal planes relaxed more than prismatic ones. The order and decaying (relaxation) pattern was not influenced by the dataset and only the $d\epsilon$ difference between lines changed.

Scan622 $(142MPa \rightarrow 168MPa \rightarrow 149MPa)$ The specimen was loaded plastically from 142MPa to 168MPa and reflection time series showed several interesting results. Compared with the results of the other three load steps (almost no difference in $d\epsilon$), the $d\epsilon$ difference between two prismatic time series is about 1.5×10^{-4}. Three lines $\langle 110 \rangle$, $\langle 021 \rangle$ and $\langle 011 \rangle$ decayed together in the whole process and $\langle 010 \rangle$ went above all the other lines. Last but not least, $\langle 112 \rangle$ was always good at relaxation as other cases. This divergence of prismatic

Table 2.9: Figure 2.43a and b Statistics (Unit: 10^{-4})

Reflection	Peak (a) $d\epsilon$	Relaxed (a) $d\epsilon$	Peak(b) $d\epsilon$	Relaxed(b) $d\epsilon$
$\langle 010 \rangle$	8.5	2.5	7.5	2.7
$\langle 021 \rangle$ $\langle 011 \rangle$ $\langle 110 \rangle$	6.7	2.5	5.7	2.2
$\langle 112 \rangle$	2.9	2.9	3.5	1.0

planes inferred several plastic events, such as distortion, started to emerge in prismatic planes. Muransky et al. [51] conducted comprehensive research for Schmid factor of distinct slip modes and the second pyramidal $\langle \mathbf{a+c} \rangle$ slip is the only mechanism which results in anisotropy of prismatic planes ($\langle 110 \rangle$ has 0.5 and $\langle 100 \rangle$ has about 0.3). From Table 2.9, the part (a) showed that the relaxation part for all peaks was almost identical for all time series and it might indicated intricate consistency of relaxation. This time, dataset selection had effect on the stable $d\epsilon$ value of $\langle 010 \rangle$, behavior of $\langle 112 \rangle$ and convergence of the middle three lines in Figure 2.43.

2.3.3.3 Error in the Least Square Fitting

Since the least square fitting is applied in the analysis, errors are inevitable in the time series computation. Algebraic distance is a good indicator of the error of fitting.

$$\begin{aligned} EOF = Q(x_j, y_j) &= Ax_j^2 + Bx_j y_j + Cy_j^2 + Dx_j + Ey_j + F \\ &= (\frac{x_j - x_0}{a})^2 + (\frac{y_j - y_0}{b})^2 - 1 \end{aligned} \tag{2.21}$$

The formula above shows the general form of the error and the form used in the thesis. However, in order to apply this EOF into the whole fitting analysis, math manipulations is required. Therefore, if the number of sampling points is n, then the averaged error ϵ is shown as follows:

$$\epsilon = \sum_{i=1}^{n} \frac{1}{n} \sqrt{(\frac{x_i - x_0}{a})^2 + (\frac{y_i - y_0}{b})^2 - 1} \tag{2.22}$$

b_{hkl} and ϵ_{hkl} are short semi-axis and error of the ellipse derived from reflection $\langle hkl \rangle$. There-

fore besides the time series, upper and lower boundaries of $d\epsilon$ can be computed from $b_{hkl}+\epsilon_{hkl}$ and $b_{hkl}-\epsilon_{hkl}$. Therefore, time series with error bars can be easily plotted. In Figure 2.44,

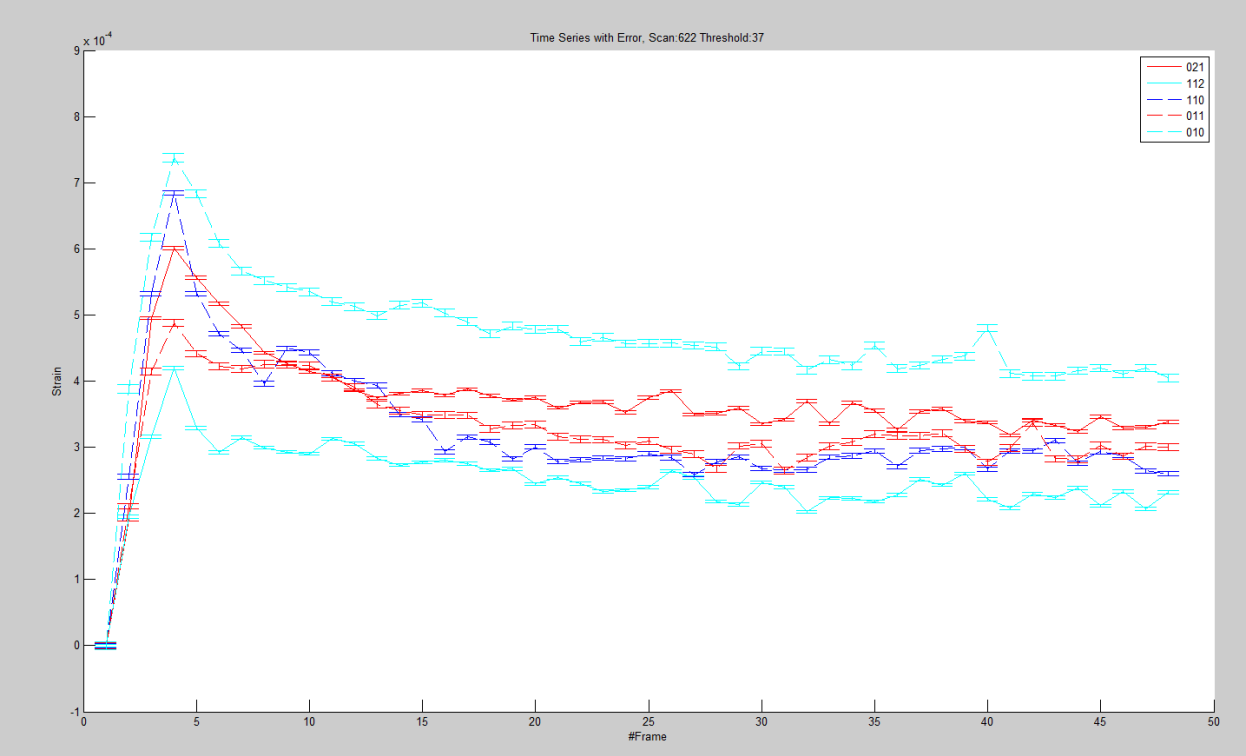

Figure 2.44: Example of Time Series with Error

five time series with error-bar are plotted and error is about 1.1×10^{-5} (see Figure 2.45).

2.3.3.4 Algorithm Sensitivity

The fitting method was sensitive to threshold choice, peaks of interest and algorithm selection. Sufficient peaks were necessary to fit the ellipse successfully and otherwise failure occurred, which might lied in no fitting result or misfit to hyperbola. The logic of a good fit will be discussed in this section.

Threshold There were two direct results of threshold choices.

1. If the threshold was too high, more number of peaks were filtered in the peak isolation program and a higher possibility of fitting failure would occur due to insufficient

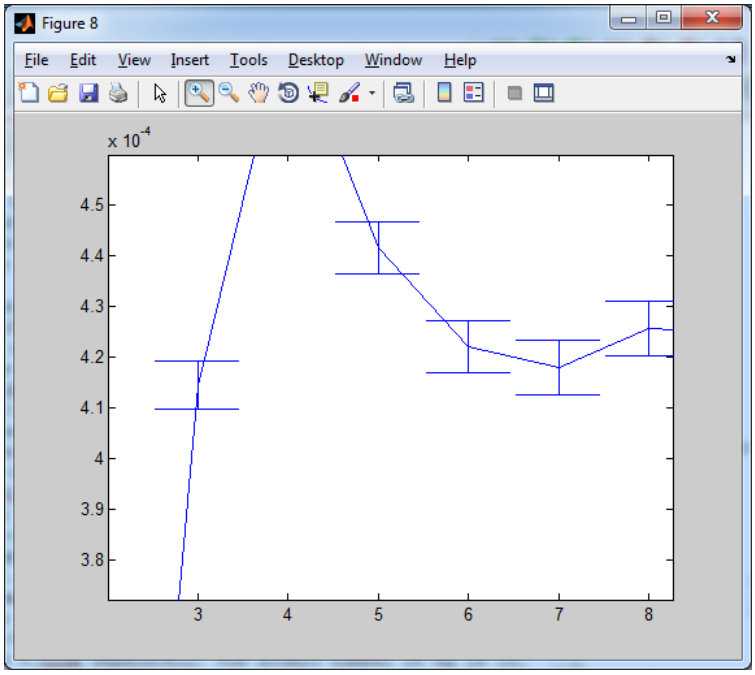

Figure 2.45: Detail of Time Series Error

sampling size. Especially for the higher order rings, no peak would be sorted out for threshold over 50.

2. If the threshold was too low, then many noisy pixels, especially in lower order rings, would be taken into consideration, which might bridge two separate peaks together and biased the peak isolation results.

25-35 was reasonable range of threshold in this algorithm and Figure 2.48 showed time series plotted under varying thresholds. Subplot a indicated that an underestimated threshold led to bias of some reflection series, such as $\langle 011 \rangle$ reflection. The $\langle 112 \rangle$ ascended with increasing thresholds and the line converged the closest in subfigure **d**. No plot was posted with threshold higher than 37 because of failure of fitting of higher order rings.

Alternative Fitting Algorithm Two fitting techniques were applied in this problem and both of them worked well and alternative fitting algorithm had advantage in some terms. For the direct fitting, the algorithm was less strict to the threshold and the upper limit was about 41, which was 4 higher than least square fitting. Figure 2.50 illustrated a trend that except $\langle 010 \rangle$, the other time series converged closer and closer with the rise of threshold.

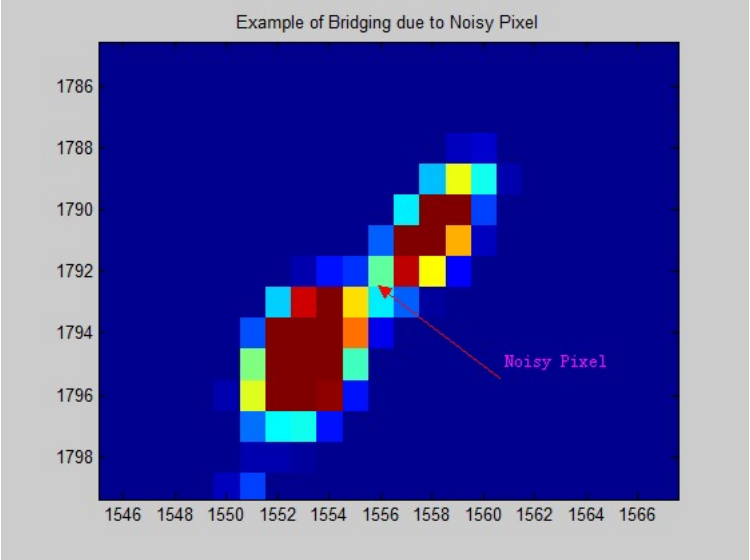

Figure 2.46: Example of Bridging of Peaks due to Noisy Pixel

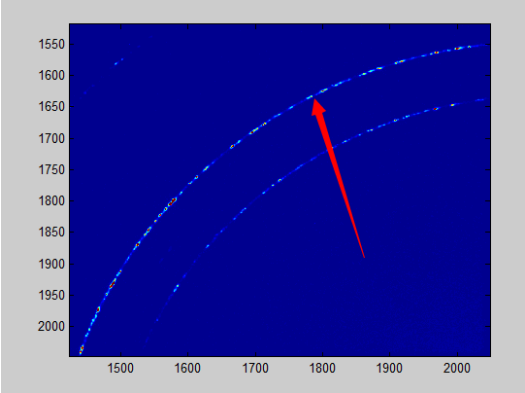

(a) Location of Subimage

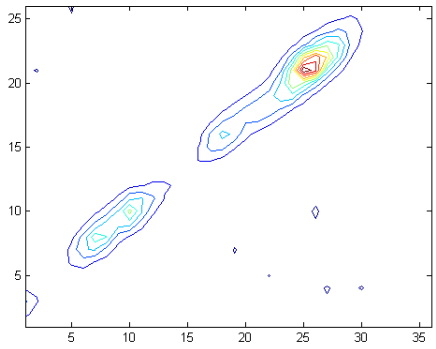

(b) Contour of Peak Profile

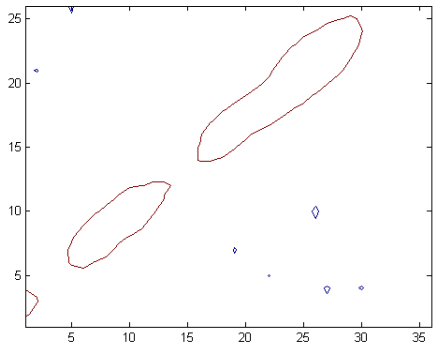

(c) Contour under Threshold 100

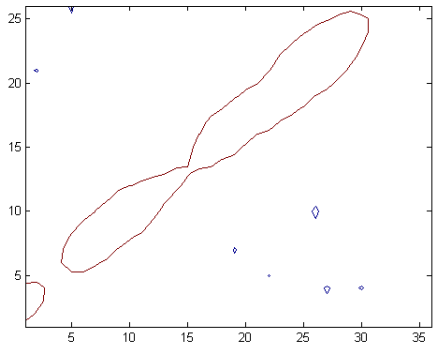

(d) Contour under Threshold 70

Figure 2.47: Effect of Threshold Change on Lower Order Diffraction Peak Contour

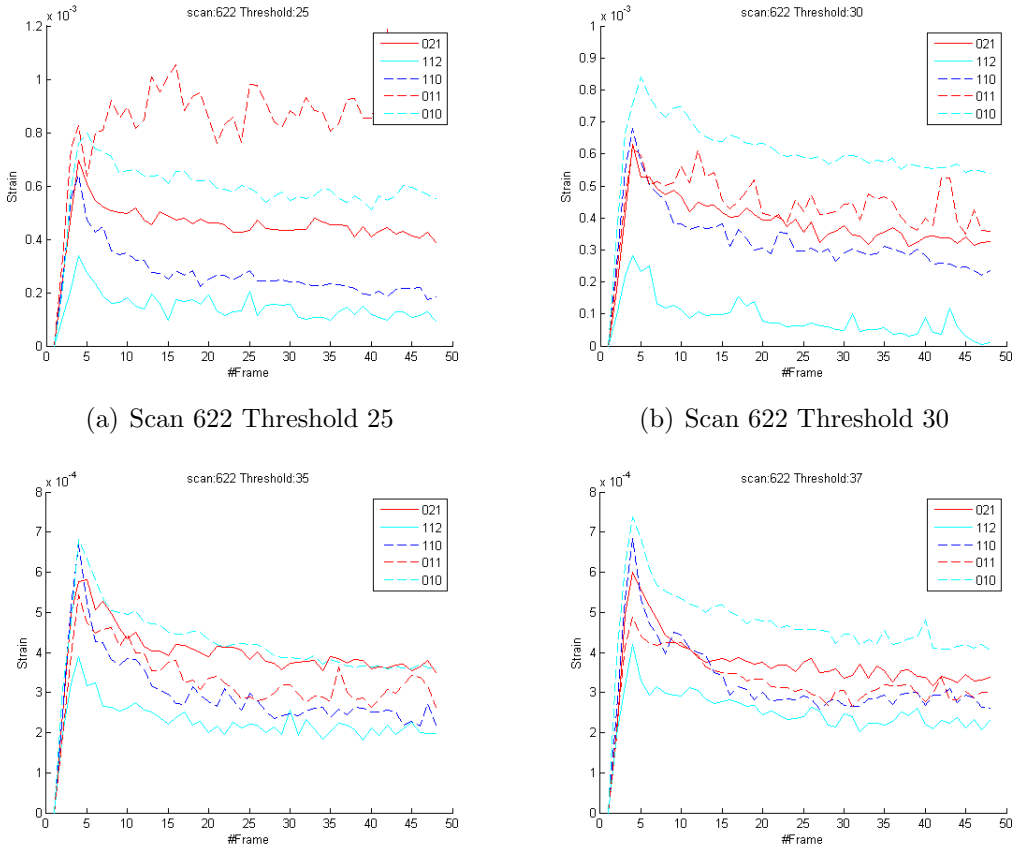

(a) Scan 622 Threshold 25

(b) Scan 622 Threshold 30

(c) Scan 622 Threshold 35

(d) Scan 622 Threshold 37

Figure 2.48: Time Series under Different Thresholds for Least Square Fitting

The consistent path in subplot **d** might help insight into some intrinsic characteristics of macroscopic relaxation process, such as activation energy.

2.3.3.5 Correlation of Plane Orientation and Maximum Strain Change

In this subsection, the relationship between plane orientation and maximum strain change $\mathbf{d}\epsilon$ is discussed above. The notation will be discussed here first. The diffraction plane orientation is parametrized by the dot product of loading direction vector $\vec{\mathbf{a}}$ and the basal orientation of the grain $\vec{\mathbf{b}}$ ($dot = \vec{a} \cdot \vec{b}$).

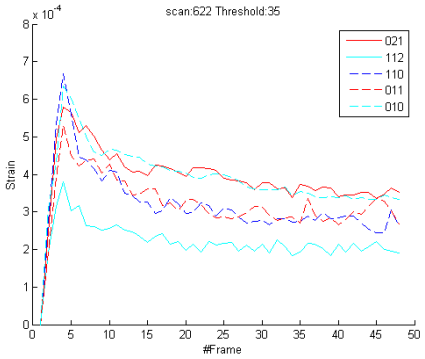

(a) Direct Fitting Result

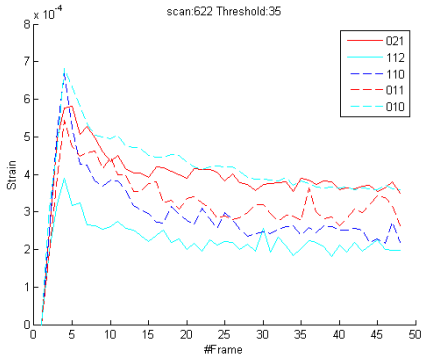

(b) Least Square Fitting Result

Figure 2.49: Comparison of Fitting Results

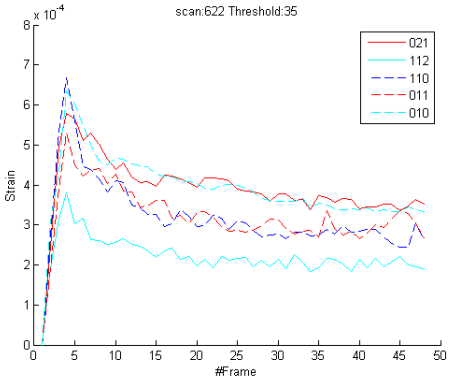

(a) Scan 622 Threshold 35

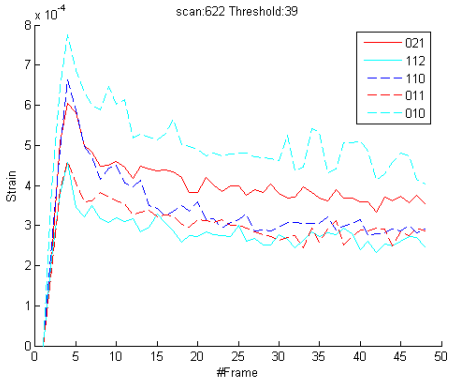

(b) Scan 622 Threshold 39

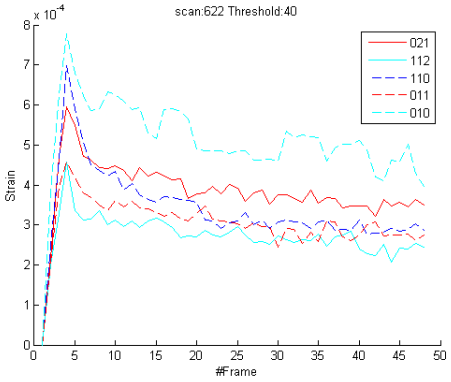

(c) Scan 622 Threshold 40

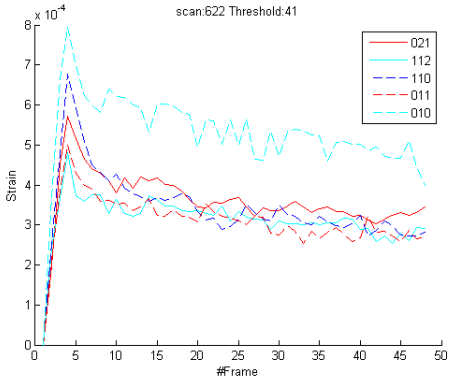

(d) Scan 622 Threshold 41

Figure 2.50: Time Series under Different Thresholds for Direct Fitting

Implementation Figure 2.51 shows geometry relationship of specimen, grain, plane and diffraction vector. The region of study are grain planes with diffraction vector almost parallel

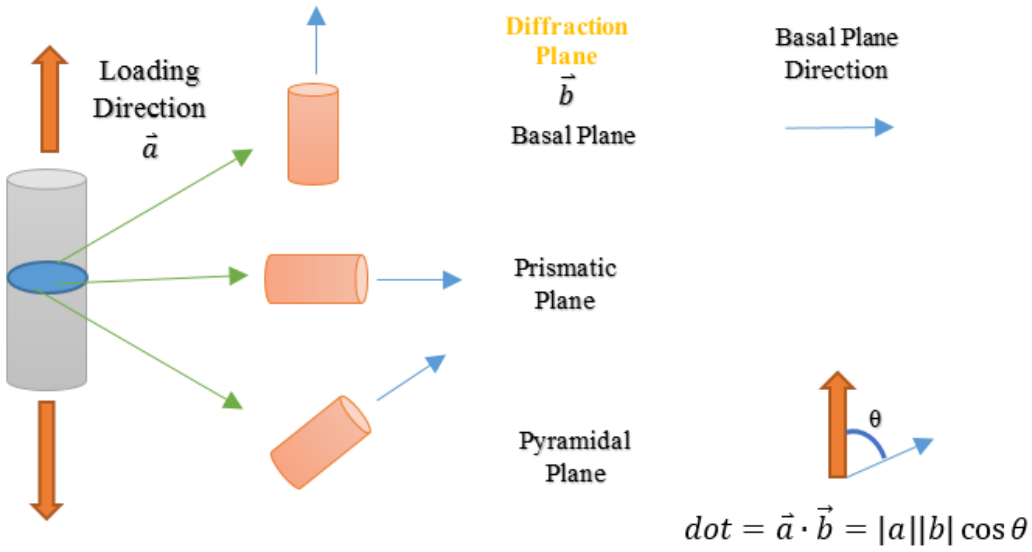

Figure 2.51: Scheme of geometry of correlation study: there are many blue grains in the blue cross section; the blue arrows are basal directions inside different grains; the loading direction can be parametrized by the reflection vector of peak

to loading direction. Red cylinders represent the spatial orientation of the grain and blue arrows ($\vec{\mathbf{b}}$) are basal directions of individual grains. Therefore, dot product of $\vec{\mathbf{a}}$ and $\vec{\mathbf{b}}$ is a reasonable indicator of degrees of activation of basal glide inside individual grains. Bernier at el. [32] gives the change-of-basis matrix $\mathbf{B}$ (the mathematical convention mentioned in equation 1.2–1.4),

$$\begin{aligned}\mathbf{B} &= \begin{bmatrix}\mathbf{a}^* & \mathbf{b}^* & \mathbf{c}^*\end{bmatrix} \\ &= \frac{1}{v}\begin{bmatrix} bc\sin\alpha^*\sin\beta\sin\gamma & 0 & 0 \\ -bc\sin\alpha^*\sin\beta\cos\gamma & ac\sin\alpha^*\sin\beta & 0 \\ -bc(\sin\alpha^*\sin\beta\cos\gamma + \cos\beta\sin\gamma) & ac\cos\alpha^*\sin\beta & ab\sin\gamma \end{bmatrix}\end{aligned} \tag{2.23}$$

The cell parameters of Mg are adopted, a and b are 320.94 pm, c is 521.08 pm, α and β are 90^o and γ is 120^o. The implementation of the change-of-basis matrix is shown by the code:

```
% This code is written to get the loading direction v.s. Basal Normal for
% different Orientations in AZ31 Magnesium Alloy
a=320.94*10^-12;
b=320.94*10^-12;
c=521.08*10^-12;
alpha=90;
beta=90;
gamma=120;
aa=alpha*pi/180;
bb=beta*pi/180;
cc=gamma*pi/180;
V=a*b*c*sqrt(1-(cos(aa))^2-(cos(bb))^2-(cos(cc))^2+2*cos(aa)*cos(bb)*cos(cc));
as=b*c*sin(aa)/V;
bs=a*c*sin(bb)/V;
cs=a*b*sin(cc)/V;
cosa=((cos(bb))*(cos(cc))-cos(aa))/((sin(bb))*(sin(cc)));
cosb=((cos(aa))*(cos(cc))-cos(bb))/((sin(aa))*(sin(cc)));
cosc=((cos(bb))*(cos(aa))-cos(cc))/((sin(bb))*(sin(aa)));
alphas=acos(cosa);
betas=acos(cosb);
gammas=acos(cosc);
A=[a b*cos(cc) c*cos(bb);
    0 b*sin(cc) -c*sin(bb)*cos(alphas);
    0 0 c*sin(bb)*sin(alphas)];
av=A(:,1);
bv=A(:,2);
cv=A(:,3);
asv=cross(bv,cv)/V;
bsv=cross(cv,av)/V;
csv=cross(av,bv)/V;
B=[asv bsv csv];
hkl=[0 2 1;1 1 2;1 1 0;0 1 1;0 1 0]';
NormalV=B*hkl;
NormalizedNormal=[];
for i=1:length(NormalV)
    NormalizedNormal(:,i)=NormalV(:,i)/norm(NormalV(:,i));
```

```
37 end
38 Basal=B*[0;0;1];
39 NormBasal=Basal/norm(Basal);
40 dotresult=NormBasal'*NormalizedNormal
```

In the code, aa, bb and cc are α, β and γ; asv, bsv and csv are $\vec{a}^*$, $\vec{b}^*$ and $\vec{c}^*$.

Result Time series generated in scan 622 are applied here because the loading path in this scenario is $168MPa \rightarrow 149MPa$, which is past the elasto-plastic transition.

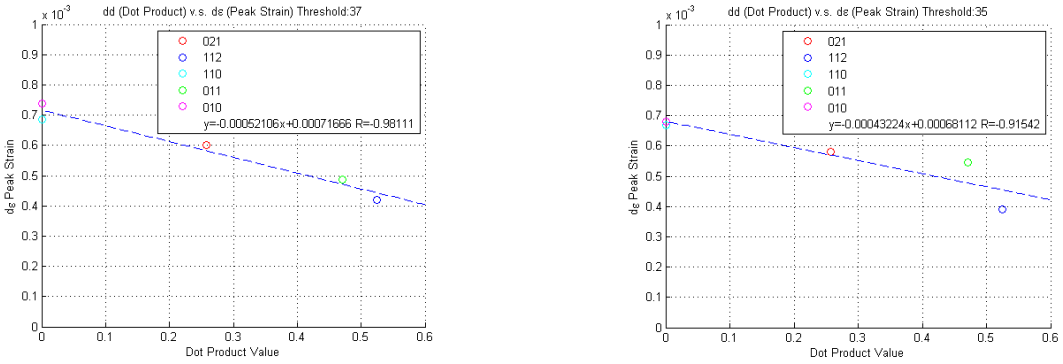

(a) Correlation with threshold 37

(b) Correlation with threshold 35

Figure 2.52: Correlation between Plane Orientation and Strain Value

Figure 2.52 shows negative linear relationship between dot value and strain and the correlation R is -0.915 for threshold 35 and -0.981 for 37.

Since the easiest slip mode of Mg is basal glide, both the slip direction and shear component on basal plane (slip plane normal) should be considered. For the basal grains (leftmost case in Figure 2.53), their slip direction is perpendicular to the loading direction and therefore the resultant shear stress in this case is zero. In another extreme case (rightmost case in Figure 2.53), prismatic grains, although the plane normal is the best for slip, no shear component can be decomposed to the slip system. Above all, neither basal nor prismatic grains are well set for slip.

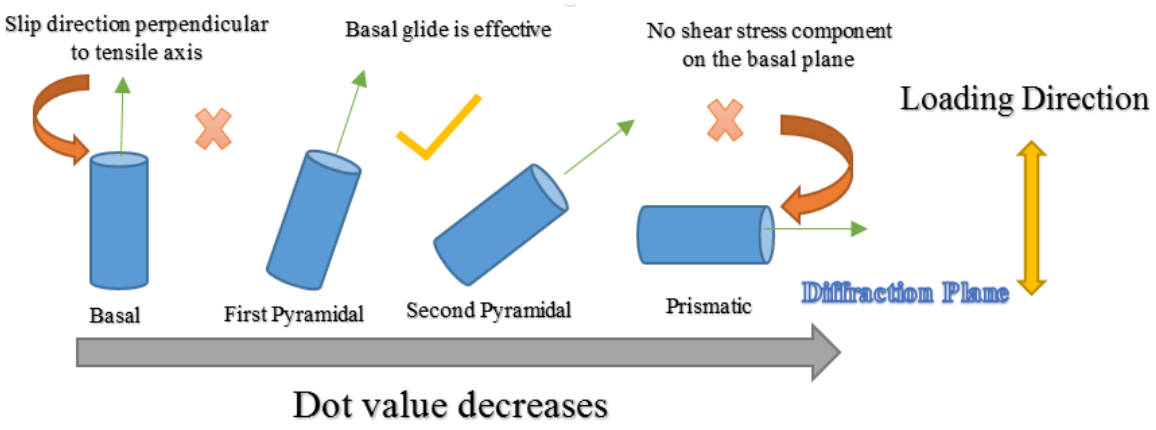

Figure 2.53: Scheme of Physical Meaning of Correlation

Now then, in the case of a grain where the basal normal is away from being perpendicular to the loading direction (two middle cases in Figure 2.53), some shear component is decomposed onto the basal plane. As there are three slip directions on the basal plane, glide on basal system will take place. As a result, more plasticity and a lower increase of lattice strain is measured because plasticity could reduce the lattice strain increase with respect to the stress increase.

CHAPTER 3

CONCLUSION

Far-field high-energy diffraction microscopy is a functional tool to study the kinetics of slip/twin events of AZ31 alloy. The technique successfully captures motion of individual peak on every diffraction rings . The background intensity is about 10, so some higher-order peaks from $\langle 200 \rangle$ and $\langle 202 \rangle$ reflections fail to be identified (intensity range from 16 to 35). A Least square ellipse fitting algorithm is used to successfully compute the reflection-wise average tensile strain. The key results will be mentioned in the following part.

Movement Direction Prismatic and pyramidal peaks show different moving directions in terms of peak dynamics. Prismatic peaks always go inwards and then relax a little or no outwards while pyramidal peaks present rich diversity: some peaks go outwards and then relax inwards, some peaks random wander about the origin point and the others follow the same trend as prismatic peaks do.

Movement Manner There are two main classes of movements observed in all the trajectories– smooth movement and jerky jump. The stop-and-jump trajectory can be interpreted by the dynamic interaction of solute atoms with mobile dislocations temporarily arrested at forest dislocation (strain-aging phenomenon), or alternatively by the non-diffusional theory mentioned in the baseline of peak dynamics.

Ellipse-fitted Time Series In the highest loading step (168MPa), two prismatic time series fitted from $\langle 010 \rangle$ and $\langle 110 \rangle$ reflections diverge and can not be converged by adjustment of threshold. This indicates anisotropic deformation occurs on grains with prismatic planes having normal parallel to the loading direction.

Peak Strain-Orientation Correlation The smaller dot product of basal vector and loading-direction-corresponding vector is, the larger the peak strain is and the easier it is to trigger the basal glide.

APPENDIX A

MULTIPLE POINTS CIRCLE FITTING ALGORITHM

```
function [x,y,r]=MultipulePointCenter(templist)
n=length(templist);
x=templist(:,1);
y=templist(:,2);
A=0;
B=0;
C=0;
D=0;
E=0;
tempx=0;
tempxx=0;
tempxxx=0;
tempy=0;
tempyy=0;
tempyyy=0;
for i=1:n
    A=A+x(i)^2;
    B=B+x(i)*y(i);
    C=C+y(i)^2;
    D=D+x(i)*y(i)^2;
    E=E+y(i)*x(i)^2;
    tempx=tempx+x(i);
    tempy=tempy+y(i);
    tempxx=tempxx+x(i)^2;
    tempxxx=tempxxx+x(i)^3;
    tempyy=tempyy+y(i)^2;
```

```
27      tempyyy=tempyyy+y(i)^3;
28  end
29  A=n*A-tempx^2;
30  B=n*B-tempx*tempy;
31  C=n*C-tempy^2;
32  D=0.5*(n*D-tempx*tempyy+n*tempxxx-tempx*tempxx);
33  E=0.5*(n*E-tempy*tempxx+n*tempyyy-tempy*tempyy);
34  a1=(D*C-B*E)/(A*C-B^2);
35  b1=(A*E-B*D)/(A*C-B^2);
36  r1=0;
37  for i=1:n
38      r1=r1+(sqrt((x(i)-a1)^2+(y(i)-b1)^2))/n;
39  end
40  x=a1;
41  y=b1;
42  r=r1;
43  end
```

APPENDIX B

MG RING GENERATION ALGORITHM

```
a=320.94; b=320.94; c=521.08;  %unit:A
Mg=Hexagonal(a,b,c);
RingD=[];
for i=1:length(Mg)
    RingD(i)=Mg{i,1}/100;
end
wavelength=0.15359;
dist=2305.50;
for i=1:length(RingD)
    % Bragg's Law: 2*d*sin(theta)=n*lambda;
    % However, the diffraction angle in this analysis is 2*theta;
    Sintheta(i)=0.5*wavelength/RingD(i);
    Ttheta(i)=asin(Sintheta(i));
    Tan2Theta(i)=tan(2*Ttheta(i));
end
MgRadius=1000*dist*Tan2Theta/200;
MR=[];
Orientation=[];
DetectorSize=2995;
for i=1:length(MgRadius)
    if MgRadius(i)*2≤DetectorSize
        MR=[MR MgRadius(i)];
        Orientation=[Orientation;Mg{i,2}];
    end
end
```

APPENDIX C

ELLIPSE FIT USING LEAST SQUARES CRITERION

```
function ellipse_t = EllipseFitAxisHandle( x,y,axis_handle )
% initialize
orientation_tolerance = 1e-3;
% prepare vectors, must be column vectors
x = x(:);
y = y(:);
% remove bias of the ellipse - to make matrix inversion more accurate. ...
    (will be added later on).
mean_x = mean(x);
mean_y = mean(y);
x = x-mean_x;
y = y-mean_y;

% the estimation for the conic equation of the ellipse
X = [x.^2, x.*y, y.^2, x, y ];
a = sum(X)/(X'*X);

% check for warnings
if ~isempty( lastwarn )
    disp( 'stopped because of a warning regarding matrix inversion' );
    ellipse_t = [];
    return
end
% extract parameters from the conic equation
[a,b,c,d,e] = deal( a(1),a(2),a(3),a(4),a(5) );

```

```
% remove the orientation from the ellipse
if ( min(abs(b/a),abs(b/c)) > orientation_tolerance )

    orientation_rad = 1/2 * atan( b/(c-a) );
    cos_phi = cos( orientation_rad );
    sin_phi = sin( orientation_rad );
    [a,b,c,d,e] = deal(...
        a*cos_phi^2 - b*cos_phi*sin_phi + c*sin_phi^2,...
        0,...
        a*sin_phi^2 + b*cos_phi*sin_phi + c*cos_phi^2,...
        d*cos_phi - e*sin_phi,...
        d*sin_phi + e*cos_phi );
    [mean_x,mean_y] = deal( ...
        cos_phi*mean_x - sin_phi*mean_y,...
        sin_phi*mean_x + cos_phi*mean_y );
else
    orientation_rad = 0;
    cos_phi = cos( orientation_rad );
    sin_phi = sin( orientation_rad );
end
% check if conic equation represents an ellipse
test = a*c;
switch (1)
case (test>0),  status = '';
case (test==0), status = 'Parabola found';  warning( 'fit_ellipse: Did ...
    not locate an ellipse' );
case (test<0),  status = 'Hyperbola found'; warning( 'fit_ellipse: Did ...
    not locate an ellipse' );
end

% if we found an ellipse return it's data
if (test>0)

    % make sure coefficients are positive as required
    if (a<0), [a,c,d,e] = deal( -a,-c,-d,-e ); end

```

```
60      % final ellipse parameters
61      X0          = mean_x - d/2/a;
62      Y0          = mean_y - e/2/c;
63      F           = 1 + (d^2)/(4*a) + (e^2)/(4*c);
64      [a,b]       = deal( sqrt( F/a ),sqrt( F/c ) );
65      long_axis   = 2*max(a,b);
66      short_axis  = 2*min(a,b);
67
68      % rotate the axes backwards to find the center point of the ...
           original TILTED ellipse
69      R           = [ cos_phi sin_phi; -sin_phi cos_phi ];
70      P_in        = R * [X0;Y0];
71      X0_in       = P_in(1);
72      Y0_in       = P_in(2);
73
74      % pack ellipse into a structure
75      ellipse_t = struct( ...
76          'a',a,...
77          'b',b,...
78          'phi',orientation_rad,...
79          'X0',X0,...
80          'Y0',Y0,...
81          'X0_in',X0_in,...
82          'Y0_in',Y0_in,...
83          'long_axis',long_axis,...
84          'short_axis',short_axis,...
85          'status','' );
86  else
87      % report an empty structure
88      ellipse_t = struct( ...
89          'a',[],...
90          'b',[],...
91          'phi',[],...
92          'X0',[],...
93          'Y0',[],...
94          'X0_in',[],...
```

```
95          'Y0_in',[],...
96          'long_axis',[],...
97          'short_axis',[],...
98          'status',status );
99  end
100
101 % check if we need to plot an ellipse with it's axes.
102 if (nargin>2) & ¬isempty( axis_handle ) & (test>0)
103
104     % rotation matrix to rotate the axes with respect to an angle phi
105     R = [ cos_phi sin_phi; -sin_phi cos_phi ];
106
107     % the axes
108     ver_line        = [ [X0 X0]; Y0+b*[-1 1] ];
109     horz_line       = [ X0+a*[-1 1]; [Y0 Y0] ];
110     new_ver_line    = R*ver_line;
111     new_horz_line   = R*horz_line;
112
113     % the ellipse
114     theta_r         = linspace(0,2*pi);
115     ellipse_x_r     = X0 + a*cos( theta_r );
116     ellipse_y_r     = Y0 + b*sin( theta_r );
117     rotated_ellipse = R * [ellipse_x_r;ellipse_y_r];
118
119     % draw
120     hold_state = get( axis_handle,'NextPlot' );
121     set( axis_handle,'NextPlot','add' );
122     plot( new_ver_line(1,:),new_ver_line(2,:),'r' );
123     plot( new_horz_line(1,:),new_horz_line(2,:),'r' );
124     plot( rotated_ellipse(1,:),rotated_ellipse(2,:),'r' );
125     set( axis_handle,'NextPlot',hold_state );
126 end
```

APPENDIX D

PEAK TRAJECTORIES I

Load I ($110MPa \longrightarrow 118MPa \longrightarrow 115MPa$)

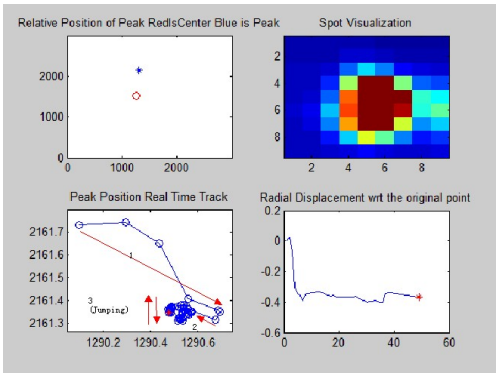

(a) $\langle 100 \rangle$

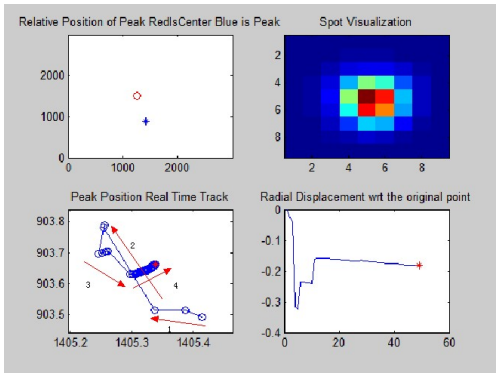

(b) $\langle 100 \rangle$

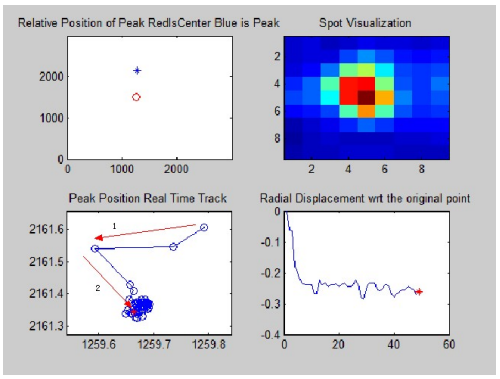

(c) $\langle 100 \rangle$

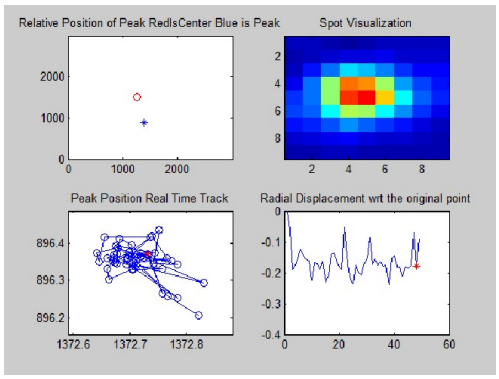

(d) $\langle 101 \rangle$

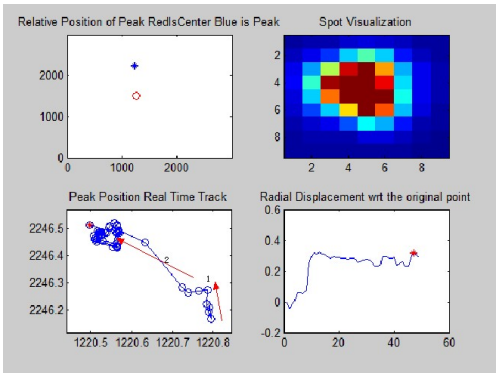

(e) ⟨101⟩

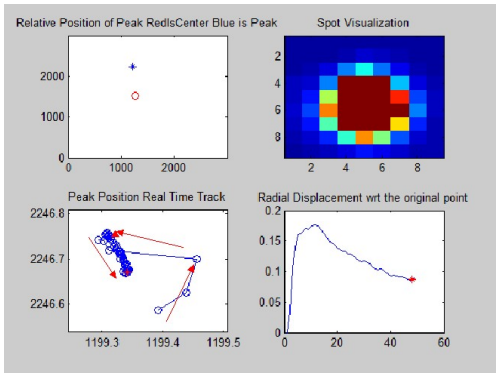

(f) ⟨101⟩

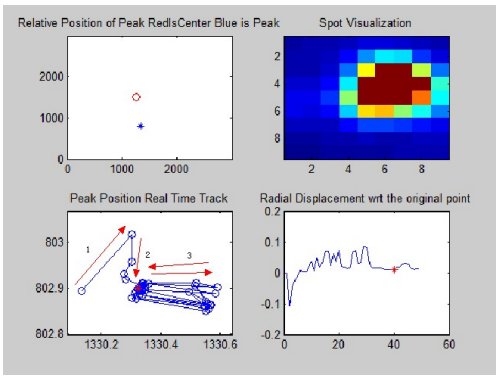

(g) ⟨101⟩

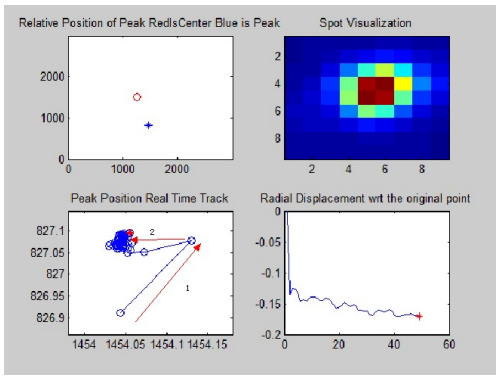

(h) ⟨101⟩

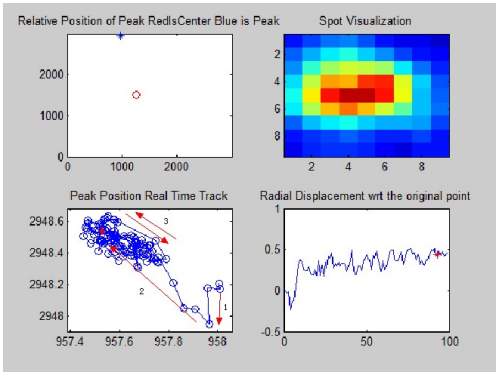

(i) ⟨202⟩

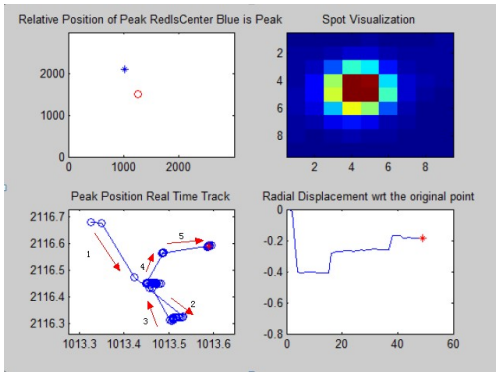

(j) ⟨100⟩

APPENDIX E

PEAK TRAJECTORIES II

Load II ($115MPa \longrightarrow 135MPa \longrightarrow 127MPa$)

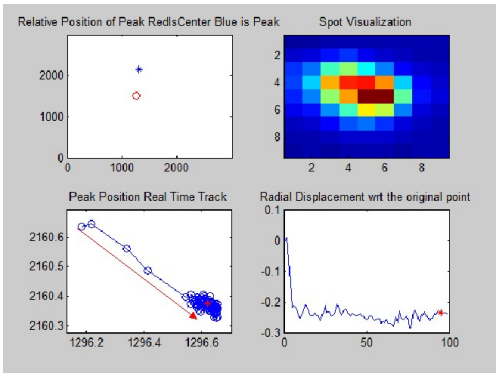

(a) $\langle 100 \rangle$

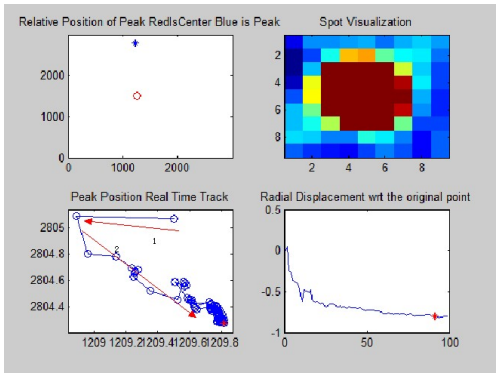

(b) $\langle 200 \rangle$

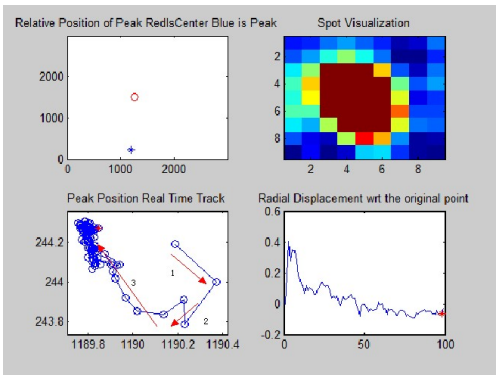

(c) $\langle 200 \rangle$

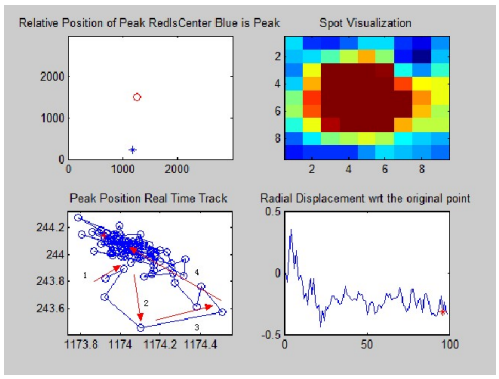

(d) $\langle 200 \rangle$

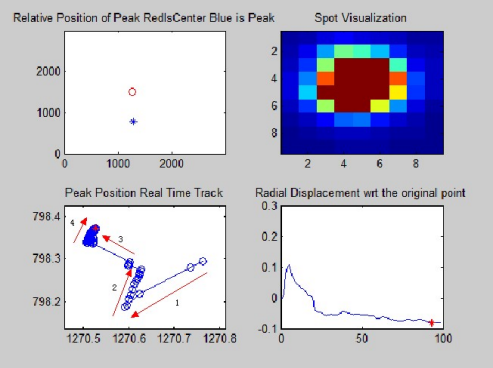

(e) ⟨101⟩

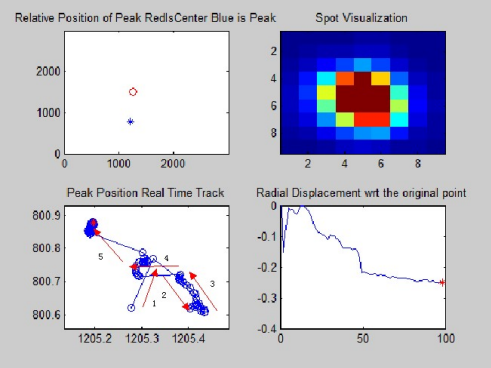

(f) ⟨101⟩

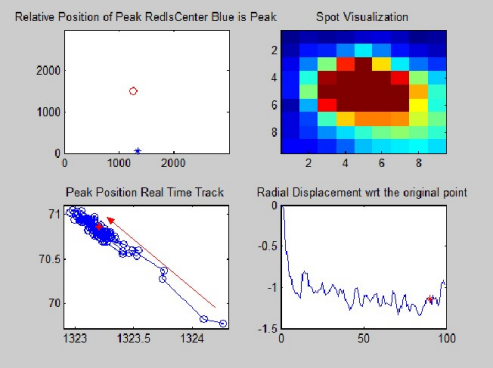

(g) ⟨202⟩

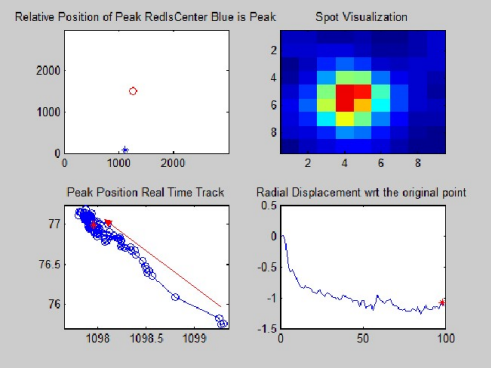

(h) ⟨202⟩

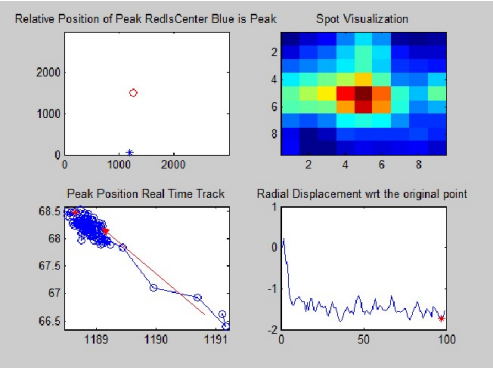

(i) ⟨202⟩

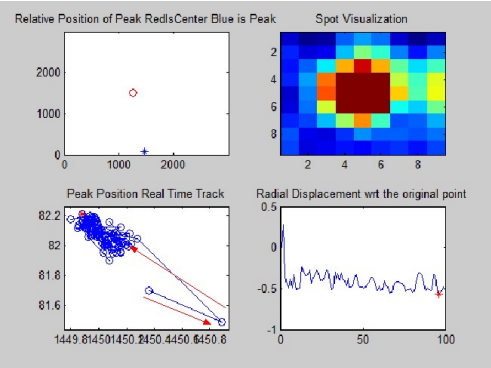

(j) ⟨202⟩

APPENDIX F

PEAK TRAJECTORIES III

Load III ($120MPa \longrightarrow 153MPa \longrightarrow 142MPa$)

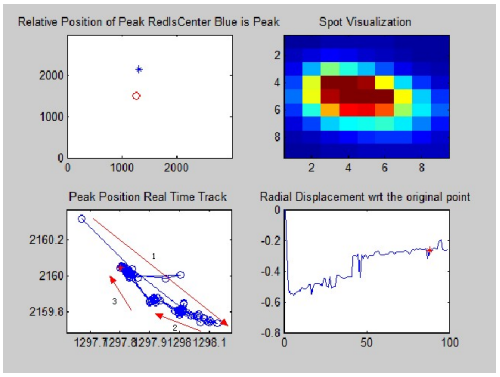

(a) $\langle 100 \rangle$

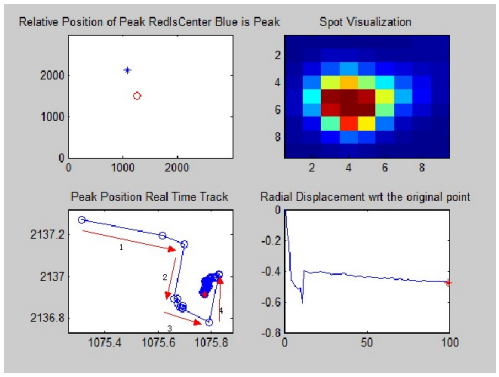

(b) $\langle 100 \rangle$

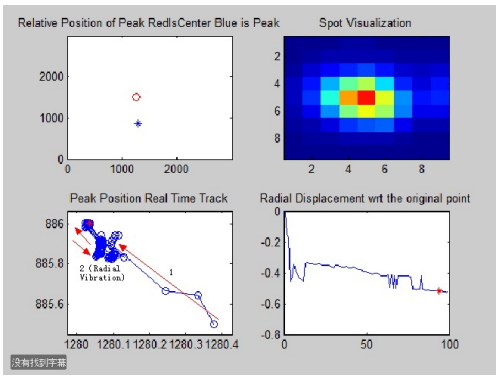

(c) $\langle 100 \rangle$

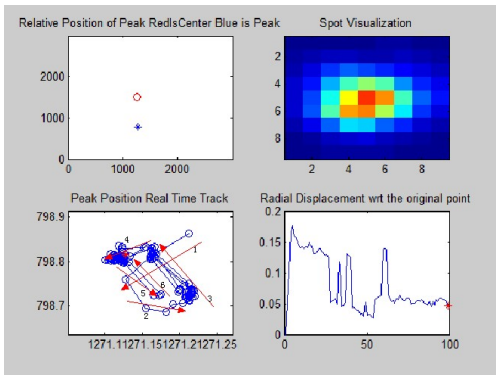

(d) $\langle 101 \rangle$

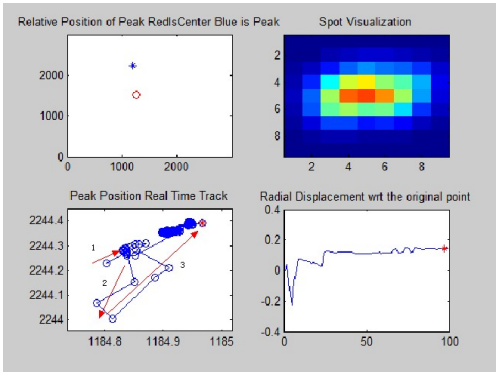

(e) ⟨101⟩

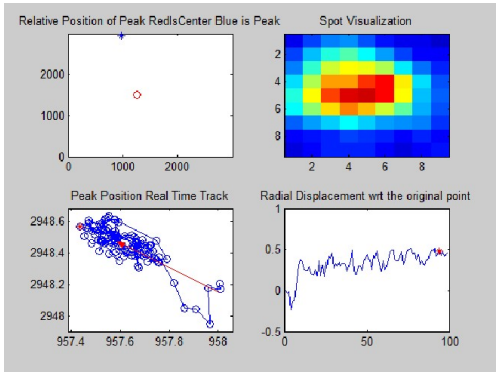

(f) ⟨202⟩

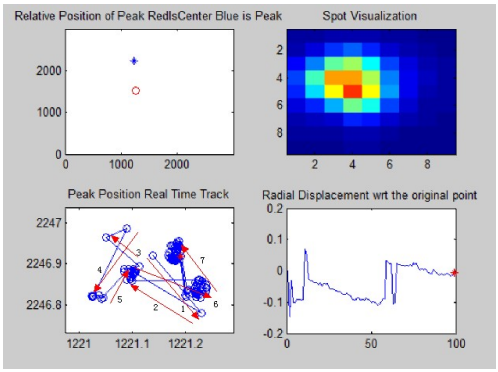

(g) ⟨101⟩

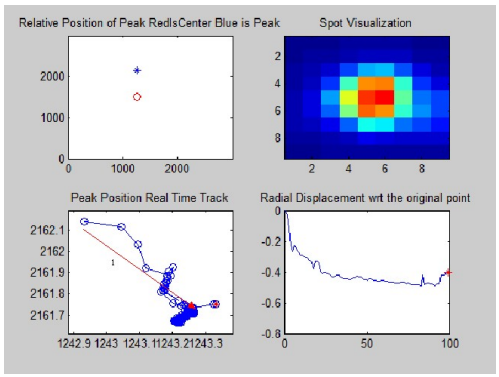

(h) ⟨100⟩

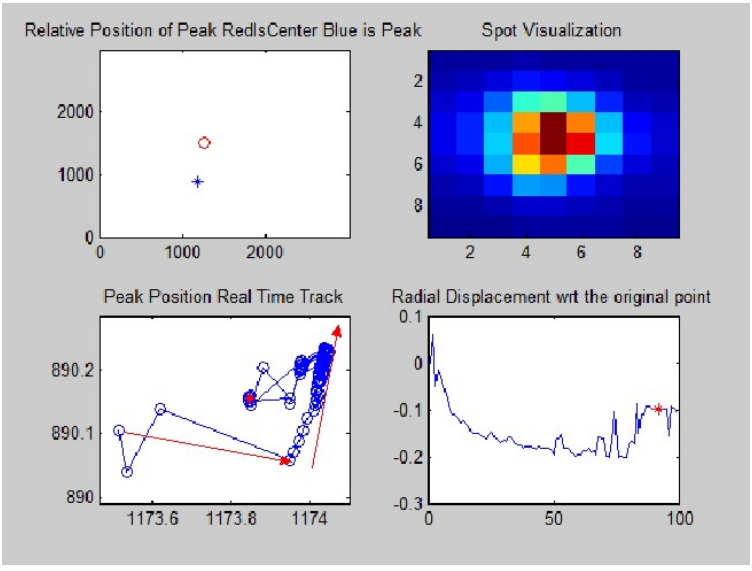

⟨100⟩

APPENDIX G

PEAK TRAJECTORIES IV

Load IV $(142MPa \longrightarrow 168MPa \longrightarrow 149MPa)$

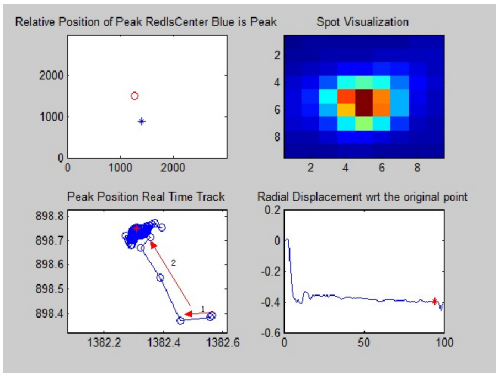

(a) $\langle 100 \rangle$

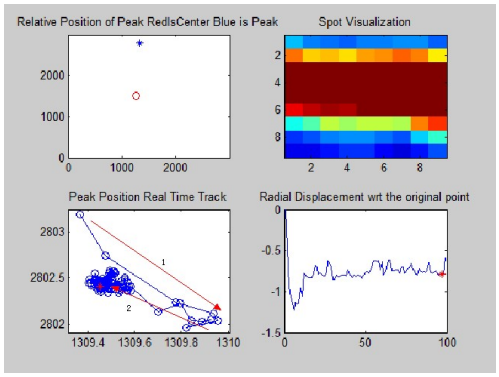

(b) $\langle 200 \rangle$

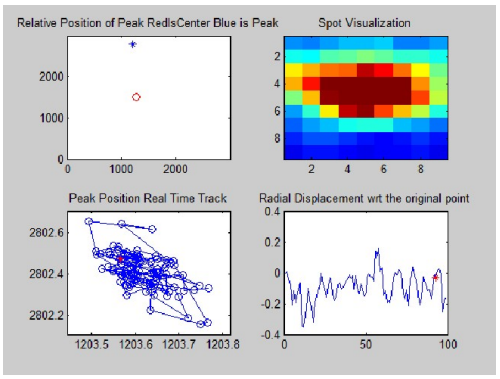

(c) $\langle 200 \rangle$

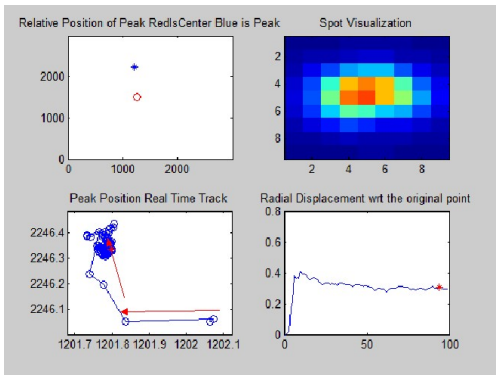

(d) $\langle 101 \rangle$

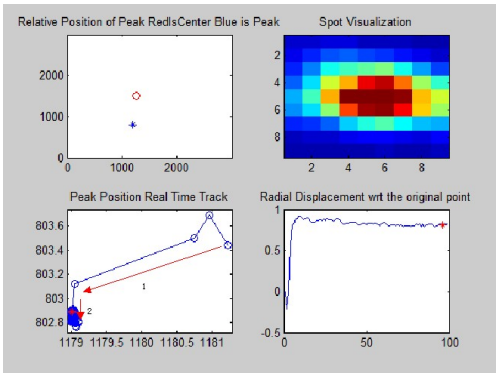

(e) ⟨101⟩

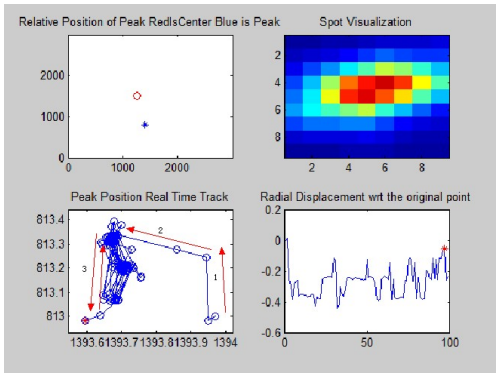

(f) ⟨101⟩

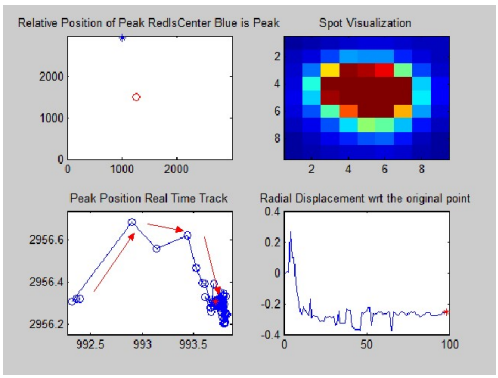

(g) ⟨202⟩

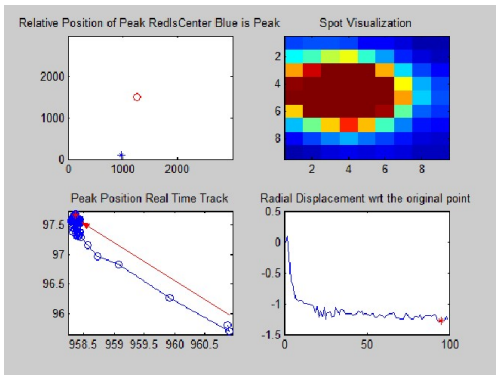

(h) ⟨202⟩

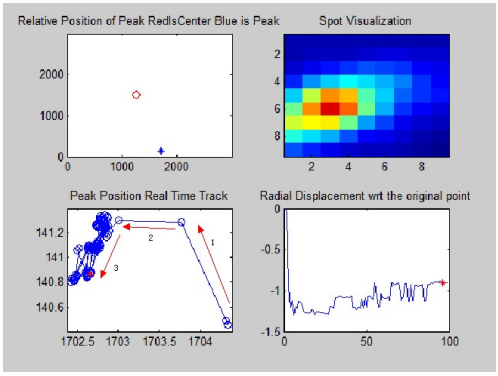

(i) ⟨202⟩

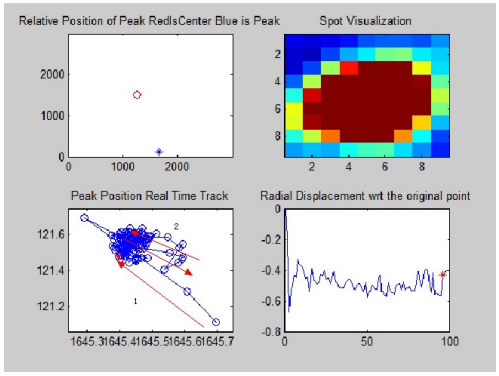

(j) ⟨202⟩

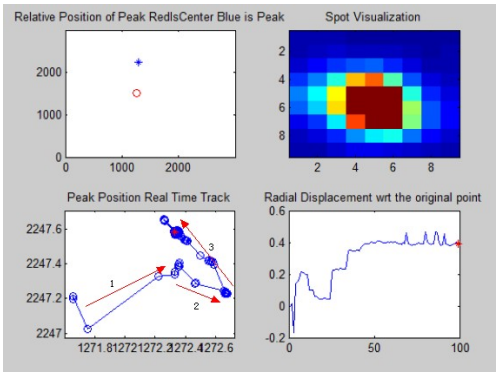
Relative Position of Peak RedIsCenter Blue is Peak
Spot Visualization
Peak Position Real Time Track
Radial Displacement wrt the original point

(k) ⟨101⟩

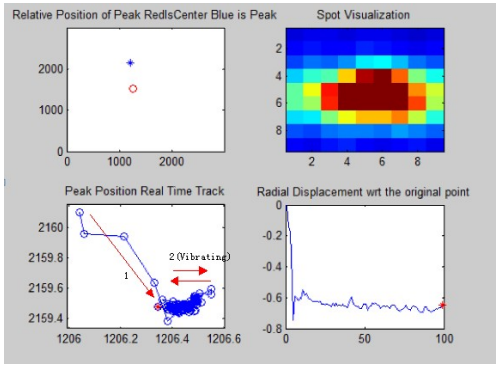
Relative Position of Peak RedIsCenter Blue is Peak
Spot Visualization
Peak Position Real Time Track
2 (Vibrating)
Radial Displacement wrt the original point

(l) ⟨100⟩

REFERENCES

[1] M. Janecek, R. Kral, P. Dobron, F. Chmelik, V. Supik, and F. Hollander, "Mechanisms of plastic deformation in {AZ31} magnesium alloy investigated by acoustic emission and transmission electron microscopy," *Materials Science and Engineering: A*, vol. 462, no. 12, pp. 311 – 315, 2007. International Symposium on Physics of Materials, 2005.

[2] H. Brar, M. Platt, M. Sarntinoranont, P. Martin, and M. Manuel, "Magnesium as a biodegradable and bioabsorbable material for medical implants," *JOM*, vol. 61, no. 9, pp. 31–34, 2009.

[3] A. Atre and W. S. Johnson, "Effect of interference on the mechanics of load transfer in aircraft fuselage lap joints," *Journal of engineering materials and technology*, vol. 129, no. 3, pp. 356–366, 2007.

[4] F. Chen and T. Huang, "Formability of stamping magnesium-alloy az31 sheets," *Journal of Materials Processing Technology*, 2003.

[5] A. Material, "Magnesium alloy az31b: Technical data sheet," 2013.

[6] A. Galiyev, R. Kaibyshev, and G. Gottstein, "Correlation of plastic deformation and dynamic recrystallization in magnesium alloy zk60," *Acta Materialia*, vol. 49, no. 7, pp. 1199–1207, 2001.

[7] S. Ion, F. Humphreys, and S. White, "Dynamic recrystallisation and the development of microstructure during the high temperature deformation of magnesium," *Acta Metallurgica*, vol. 30, no. 10, pp. 1909–1919, 1982.

[8] M. Yoo, "Slip, twinning, and fracture in hexagonal close-packed metals," *Metallurgical Transactions A*, vol. 12, no. 3, pp. 409–418, 1981.

[9] G. I. Taylor, "Plastic Strain in Metals," *Journal of the Institute of Metals*, vol. 62, pp. 307–324, 1938.

[10] M. Yoo, J. Morris, K. Ho, and S. Agnew, "Nonbasal deformation modes of hcp metals and alloys: Role of dislocation source and mobility," *Metallurgical and Materials Transactions A*, vol. 33, no. 3, pp. 813–822, 2002.

[11] A. Couret, D. Caillard, W. Pschl, and G. Schoeck, "Prismatic glide in divalent h.c.p. metals," *Philosophical Magazine A*, vol. 63, no. 5, pp. 1045–1057, 1991.

[12] S. Agnew, M. Yoo, and C. Tom, "Application of texture simulation to understanding mechanical behavior of mg and solid solution alloys containing li or y," *Acta Materialia*, vol. 49, no. 20, pp. 4277 – 4289, 2001.

[13] M. Yoo, S. Agnew, J. Morris, and K. Ho, "Non-basal slip systems in HCP metals and alloys: source mechanisms," *Materials Science and Engineering: A*, vol. 319-321, pp. 87–92, Dec. 2001.

[14] M. Morris, J.R.a, Ho, K.M.a, Chen, K.Y.a, Rengarajan, G.bd, Yoo, "Large-scale atomistic study of core structures and energetics of c+a {1122} dislocations in hexagonal close packed metals," *Modelling and Simulation in Materials Science and Engineering*, vol. 8, no. 1, pp. 25–35, 2000.

[15] J. Koike, T. Kobayashi, T. Mukai, H. Watanabe, M. Suzuki, K. Maruyama, and K. Higashi, "The activity of non-basal slip systems and dynamic recovery at room temperature in fine-grained {AZ31B} magnesium alloys," *Acta Materialia*, vol. 51, no. 7, pp. 2055 – 2065, 2003.

[16] M. Homayonifar, *Modeling of Deformation-induced Twinning and Dislocation Slip in Magnesium Using a Variationally Consistent Approach.* HZG report, Helmholtz-Zentrum, 2011.

[17] Y. Minonishi, S. Ishioka, M. Koiwa, and S. Morozumi, "Structure of right brace 1121 left brace twin boundaries in h. c. p. crystals.," *Physica Status Solidi (A) Applied Research*, vol. 71, no. 1, pp. 253–258, 1982.

[18] Y. Chino, K. Kimura, and M. Mabuchi, "Twinning behavior and deformation mechanisms of extruded AZ31 Mg alloy," *Materials Science and Engineering: A*, vol. 486, pp. 481–488, July 2008.

[19] S. Yi, C. Davies, H.-G. Brokmeier, R. Bolmaro, K. Kainer, and J. Homeyer, "Deformation and texture evolution in AZ31 magnesium alloy during uniaxial loading," *Acta Materialia*, vol. 54, pp. 549–562, Jan. 2006.

[20] E. Emley, "Principles of magnesium technology," *Pergamon*, 1966.

[21] R. V. Mises, "Mechanik der plastischen formnderung von kristallen," *J Appl Math Mech (ZAMM)*, vol. 8, 1928.

[22] Y. Liu and X. Wu, "An electron-backscattered diffraction study of the texture evolution in a coarse-grained az31 magnesium alloy deformed in tension at elevated temperatures," *Metallurgical and Materials Transactions A*, vol. 37, no. 1, pp. 7–17, 2006.

[23] B. B. He, *Geometry Conventions*, pp. 28–50. John Wiley Sons Inc., 2009.

[24] B. B. He, *Introduction*, pp. 1–27. John Wiley Sons Inc., 2009.

[25] R. M. S. E. M. Lauridsen, S. Schmidt and H. F. Poulsen, "Tracking: a method for structural characterization of grains in powders or polycrystals," vol. 34, pp. 744–750, 2001.

[26] U. Lienert, R. M. Suter, C. M. H. S. F. Li, and J. Lind, "High energy x-ray diffraction microscopy (hedm):microstructure responses in polycrystals," 2012. `http://neon.materials.cmu.edu/rollett/for-downloading/SummerSchool2012/HEDM_summerschool2012.pdf`.

[27] H. J. Bunge, *Texture Analysis in Materials Science*. Butterworth Heinemann, 1982.

[28] L. Margulies, T. Lorentzen, H. F. Poulsen, and T. Leffers, "Strain tensor development in a single grain in the bulk of a polycrystal under loading," *Acta Materialia*, vol. 50, no. 7, pp. 1771–1779, 2002.

[29] R. V. Martins, L. Margulies, S. Schmidt, H. F. Poulsen, and T. Leffers, "Simultaneous measurement of the strain tensor of 10 individual grains embedded in an al tensile sample," *Materials Science and Engineering A*, vol. 387-389, no. 1-2 SPEC. ISS., pp. 84–88, 2004.

[30] M. Moscicki, P. Kenesei, J. Wright, H. Pinto, T. Lippmann, A. Borbly, and A. R. Pyzalla, "Friedel-pair based indexing method for characterization of single grains with hard x-rays," *Materials Science and Engineering A*, vol. 524, no. 1-2, pp. 64–68, 2009.

[31] J. Oddershede, S. Schmidt, H. F. Poulsen, H. O. Srensen, J. Wright, and W. Reimers, "Determining grain resolved stresses in polycrystalline materials using three-dimensional x-ray diffraction," *Journal of Applied Crystallography*, vol. 43, no. 3, pp. 539–549, 2010.

[32] J. Bernier, N. Barton, U. Lienert, and M. Miller, "Far-field high-energy diffraction microscopy: A tool for intergranular orientation and strain analysis," *Journal of Strain Analysis for Engineering Design*, vol. 46, no. 7, pp. 527–547, 2011.

[33] R. M. Suter, D. Hennessy, C. Xiao, and U. Lienert, "Forward modeling method for microstructure reconstruction using x-ray diffraction microscopy: Single-crystal verification," *Review of Scientific Instruments*, vol. 77, no. 12, 2006.

[34] R. M. Suter, C. M. Hefferan, S. F. Li, D. Hennessy, C. Xiao, U. Lienert, and B. Tieman, "Probing microstructure dynamics with x-ray diffraction microscopy," *Journal of Engineering Materials and Technology, Transactions of the ASME*, vol. 130, no. 2, pp. 0210071–0210075, 2008.

[35] W. Ludwig, P. Reischig, A. King, M. Herbig, E. M. Lauridsen, G. Johnson, T. J. Marrow, and J. Y. Buffre, "Three-dimensional grain mapping by x-ray diffraction contrast tomography and the use of friedel pairs in diffraction data analysis," *Review of Scientific Instruments*, vol. 80, no. 3, 2009.

[36] U. Lienert, "High energy diffraction microscopy at the advanced photon source 1-id beamline," 2009. http://ftp.esrf.eu/pub/scisoft/fable/talks/workshop_April_2009/HighEnergyDiffractionAPS_Lienert.pdf.

[37] V. G. Tkachenko, "Physical theory of useful strength of metallic crystals," *Strength of Materials*, vol. 45, no. 5, pp. 555 – 564, 2013.

[38] V. G. Tkachenko, "Model of dislocation microyield of metallic crystals," *Defects and Fracture of Materials and Nanomaterials*, pp. 90 – 92, 2011.

[39] N. Kamyshanchenko, I. Nikulin, E. Kungurtsev, and M. Kungurtsev, "Experimental determination of preferential mechanisms of stress relaxation during deformation of hcp metals," *Technical Physics Letters*, vol. 39, no. 5, pp. 469–471, 2013.

[40] P. Lukáč and Z. Trojanová, "Stress relaxation in an az31 magnesium alloy," 2011.

[41] R. M. Suter, L. Young, and J. Schuren, "High energy diffraction microscopy at sector 1: An inside view of materials' responses," 2013. http://www.aps.anl.gov/News/Meetings/Monthly_Meetings/2013/20130424_suter.pdf.

[42] B. group, "Users guide for the ge amorphous silicon angio flat panel detector," 2009. https://http://www.aps.anl.gov/Xray_Science_Division/Detectors/Detector_Pool/Detector_Information/GE_Amorphous_Silicon_Detector/GEaSi_UsersGuide-V3_public.pdf.

[43] P. Delmas, "University of auckland lectures gaussian filtering," 2010. https://www.cs.auckland.ac.nz/courses/compsci373s1c/PatricesLectures/Gaussian%20Filtering_1up.pdf.

[44] M. Inc., "Enhancement methods in image processing," 2014. https://http://www.mathworks.com/discovery/image-enhancement.html.

[45] B. Warren, *X-Ray Diffraction*. Courier Dover Publications, 1969.

[46] D. Umbach and K. Jones, "A few methods for fitting circles to data," *Instrumentation and Measurement, IEEE Transactions on*, vol. 52, pp. 1881–1885, Dec 2003.

[47] F. Bookstein, "Fitting conic sections to scattered data," *Computer Graphics and Image Processing*, vol. 9, no. 1, pp. 56 – 71, 1979.

[48] A. Fitzgibbon, M. Pilu, and R. Fisher, "Direct least square fitting of ellipses," *IEEE Transactions on Pattern Analysis and Machine Intelligence*, vol. 21, pp. 476–480, May 1999.

[49] C. Corby, C. Cceres, and P. Luk, "Serrated flow in magnesium alloy az91," *Materials Science and Engineering: A*, vol. 387389, no. 0, pp. 22 – 24, 2004.

[50] Z. S. Basinski and P. J. Jackson, "The effect of extraneous deformation on strain hardening in cu single crystals," *Applied Physics Letters*, vol. 6, no. 8, pp. 148–150, 1965.

[51] O. Murnsky, D. Carr, M. Barnett, E. Oliver, and P. ittner, "Investigation of deformation mechanisms involved in the plasticity of {AZ31} mg alloy: In situ neutron diffraction and {EPSC} modelling," *Materials Science and Engineering: A*, vol. 496, no. 12, pp. 14 – 24, 2008.